SEED LOCALIZATION IN IMAGE-GUIDED PROSTATE BRACHYTHERAPY INTRAOPERATIVE DOSIMETRY SYSTEMS

by
Nathanael Kuo

A dissertation submitted to Johns Hopkins University in conformity with the requirements for the degree of Doctor of Philosophy.

Baltimore, Maryland
September, 2013

Abstract

Prostate cancer is the most common cancer among men in the United States. Many treatments are available, but prostate brachytherapy is acknowledged as a standard treatment for patients with localized cancer. Prostate brachytherapy is a minimally invasive surgery involving the permanent implantation of approximately 100 grain-sized radioactive seeds into the prostate. While effective, contemporary practice of brachytherapy is suboptimal because it spreads the stages of planning, implant, and dosimetry over several weeks. Although brachytherapy is now moving towards intraoperative treatment planning (ITP) which integrates all three stages into a single day in the operating room, the American Brachytherapy Society states, "the major current limitation of ITP is the inability to localize the seeds in relation to the prostate." While the procedure is traditionally guided by transrectal ultrasound (TRUS), poor image quality prevents TRUS from accurately localizing seeds to compute dosimetry intraoperatively. Alternative methods exist, but are generally impractical to implement in clinics worldwide.

The subject of this dissertation is the development of two intraoperative dosimetry systems to practically solve the problem of seed localization in ITP. The first system fuses TRUS with X-ray fluoroscopy using the ubiquitous non-isocentric mobile C-arm. The primary contributions of this dissertation include an automatic fiducial and seed segmentation algorithm for fluoroscopic images, as well as a next generation intraoperative dosimetry system based on a fiducial with seed-like markers. Results from over 30 patients prove that both contributions are significant for localizing seeds with high accuracy and demonstrate the capability of detecting cold spots. The second intraoperative dosimetry system is based on photoacoustic imaging, and uses the already implemented TRUS probe to detect ultrasonic waves converted from electromagnetic waves generated by a laser. The primary contributions of this dissertation therefore also include a prototype benchtop photoacoustic system and an improved clinical version usable in the operating room. Results from gelatin phantoms, an *ex vivo* dog prostate, and an *in vivo* dog study reveal that multiple seeds are clearly visible with high contrast using photoacoustic imaging at clinically safe laser energies. Together, both systems significantly progress the latest technologies to provide optimal care to patients through ITP.

Thesis Committee:

Dr. Jerry L. Prince (advisor)

Dr. Emad M. Boctor (advisor)

Dr. Jeffrey H. Siewerdsen

Dr. Junghoon Lee

Preface

The dissertation contained in these pages is the culmination of my graduate research that began so long ago in August 2007. It also summarizes the arduous journey that I have taken from a research novice to seasoned expert. I first thank the reader for taking the time to read this dissertation detailing the contributions I have made to the research community through these past several years.

Of course, none of this work would be possible without the many people who helped me along the way. Dr. Jerry L. Prince, my primary advisor, has been an invaluable mentor to me, not only in his support, but in being such a great example of research professionalism. Words cannot express my admiration for his research intuition, his commitment to the interests of his students, and for his balanced lifestyle. Dr. Emad M. Boctor, my secondary advisor, has also been a source of inspiration to me. His limitless ideas and his diligent work ethic demonstrate such a passion for research that is hard to come by. I would also like to specifically thank Dr. Junghoon Lee, who although is not officially among my advisors, is someone I acknowledge as a mentor and friend. Without him, I would not nearly be so adept and accomplished in my studies today. Special thanks also to Dr. Jeffrey H. Siewerdsen, who has been my essential thesis committee member from the Department of Biomedical Engineering, and has taken the time to see my progress from the graduate board oral to the thesis proposal to the research defense.

There are many other people who have helped me along the way, much too numerous to mention by name. These include my labmates from the Image Analysis and Communications Laboratory and the Medical UltraSound Imaging and Intervention Collaboration. Their support has pushed me forward when it seemed like there was no light at the end of the tunnel. Thanks also to the Department of Biomedical Engineering and the Johns Hopkins University for giving me such a wonderful opportunity and a nurturing environment to grow professionally.

My dearest thanks to my family, especially Mom and Dad, the two most special people to me on earth. There is no way I would have ever made it this far without their encouragement to improve not only academically, but in all aspects of life, and I dedicate this dissertation to them. Finally, I give my thanks to God. To Him do I not only owe my success, but also my life, and all glory belongs to His name.

Table of Contents

List of Tables

List of Figures

Chapter 1. Introduction

Across the globe, prostate cancer is the second most frequently diagnosed cancer and the sixth leading cause of cancer deaths in males [23]. In the United States alone, the statistics are even less favorable with prostate cancer being the most common cancer among men at nearly 240,000 cases and 30,000 deaths per year [55]. It is predicted that more than 80% of men will develop prostate cancer by the age of 80 [3].

1.1 Prostate Brachytherapy

There are many treatments that currently exist to combat these sobering statistics, such as radical prostatectomy, external beam radiation therapy, and hormonal therapy. However, permanent low-dose-rate brachytherapy is acknowledged as a standard option of care for patients of localized prostate cancer, with estimates of up to 250,000 treated by it in the United States during the past decade [7]. Permanent prostate brachytherapy (PPB) is a minimally invasive surgery that permanently implants approximately 100 grain-sized radioactive seeds into the prostate. The goal of the operation is to optimally position the seeds in order to maximize dose to cancerous tissue and minimize dose to healthy tissue. PPB is an effective means to treating prostate cancer, and has become a common choice among patients and surgeons because of its excellent long-term treatment outcomes of maximizing cancer control while minimizing morbidity [30, 65].

The treatment typically begins with a transrectal ultrasound (TRUS) planning study a few weeks before the implant to outline the prostate contour and to prepare the optimal placement of seeds. The implant then takes place in the operating room (OR), where the seeds are delivered via surgical needles through the perineum into the prostate, also under TRUS guidance. Finally, the patient is imaged most commonly by X-ray computed tomography (CT) within 60 days after the operation to verify the success of the operation in a final post-implant dosimetry.

1.2 Current Limitations

This contemporary procedure has several limitations that may be improved by a process called intraoperative treatment planning (ITP), as recommended by the American Brachytherapy Society [45].

ITP condenses all the steps of the treatment – planning, implant, and dosimetry – into one procedure in the OR. By moving the planning stage into the OR (known as intraoperative preplanning), ITP avoids any needless changes in anatomy or setup that may occur between planning and implant. By moving the dosimetry stage into the OR (known as dynamic dose calculation), ITP also allows additional seeds to be implanted immediately, rather than weeks, thereafter if the dosimetry is deemed insufficient. Furthermore, the three stages may be iterated, with the latest intraoperative dosimetry generating an updated plan for the additional implant of seeds.

Iteration of planning, implant, and dosimetry is an especially salient feature of ITP since such dynamic planning is necessary to provide truly optimal seed placement (see Figure 1). Even though the surgeon may have an optimal initial plan, actual seed locations may deviate from the planned seed locations for a variety of reasons. First, the seeds may naturally migrate in the soft tissue of the prostate. Secondly, the prostate itself may deform due to patient movement, needle insertion, or edema caused by the procedure. Finally, the surgeon himself may place seeds imprecisely during implantation. The ability to compensate for such deviations is essential to produce the best surgical outcome for the patient.

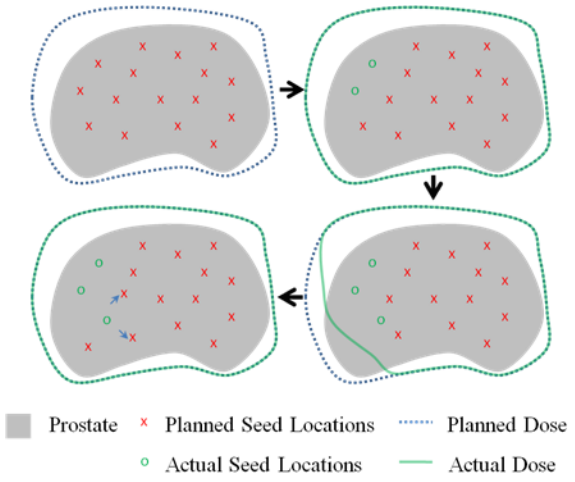

Figure 1 Illustration of dynamic planning. In the top left, surgeon plans seed locations to give planned dose. In the top right, surgeon implants seeds so that actual seed locations match planned seed locations. In the bottom right, an implanted seed deviates from planned location causing a "cold spot". In the bottom left, future planned seed locations are modified to compensate for deviations already present.

ITP would be a bold step forward to optimizing patient-specific care through PPB, but as stated by the American Brachytherapy Society, "the major current limitation of ITP is the inability to localize the seeds in relation to the prostate," primarily due to the failings of TRUS. While TRUS is a valuable intraoperative tool for contouring the prostate during planning and for visualizing surgical needles during implant, it is difficult to use TRUS alone for localizing seeds during dosimetry (see Figure 2). False positives occur due to calcifications and air bubbles, while false negatives occur due to shadowing effects and poor image quality. Some have tried to segment the seeds in TRUS images but it has become widely accepted that TRUS alone is insufficient to locate seeds in relation to the prostate [16].

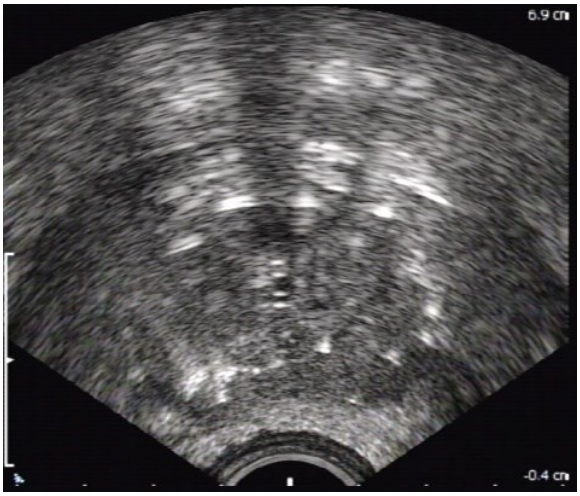

Figure 2 Sample TRUS image. It is difficult to localize seeds with TRUS alone because there are many false positives and false negatives.

1.3 Other Approaches to Intraoperative Dosimetry

Alternative approaches have been suggested to localize seeds for intraoperative dosimetry. There are several groups who have remained in the realm of ultrasound despite its disadvantages, utilizing technologies such as Doppler ultrasound high-resolution TRUS or three-dimensional probes [42, 79, 73, 74]. While some results are promising, most have not yet been proven to succeed in patients and still suffer from the same ultrasound weaknesses. Other approaches attempt to supplement or entirely replace ultrasound to localize seeds, a review of which may be found in the paper by Polo et al. [49]. To summarize, one approach is based on conventional CT scanners or cone-beam CT using flat-panel C-arms

[13, 75]. Although effective in locating seeds, such scanners and motorized encoded C-arms are uncommon in the OR and require a large orbit around the patient which is impractical to accomplish in the typically confined brachytherapy setup. Another approach is based on magnetic resonance imaging (MRI) [5, 6]. MRI is excellent for imaging prostatic tissue and is capable of identifying implanted seeds; however, intraoperative MRI is cumbersome, expensive, and slow while also requiring robotics to operate within the confined bore of the scanner during implant. There are other approaches, such as those based on vibro-acoustography [44, 43], but such technologies are still in early developmental stages.

1.4 Proposed Intraoperative Dosimetry Systems

To solve these challenges, two intraoperative dosimetry systems are proposed in this dissertation. Both systems are effective, empowering surgeons to intraoperatively localize seeds in relation to the prostate as could never be done before. Both systems are economical, adding little additional expense in our currently cost-conscious health care system. Both systems are finally practical, adding minimal changes to current brachytherapy protocol and, consequently, incurring few if any further burdens to the surgeon. These systems are capable of widespread use due to their effectiveness, low cost, and practicality in solving the seed localization problem.

The first proposed intraoperative dosimetry system fuses TRUS with X-ray fluoroscopy based on the ubiquitous mobile non-isocentric C-arm to localize the seeds with respect to the prostate. Fluoroscopy can visualize the metallic seeds well, but alone it cannot visualize the prostate. It therefore makes a perfect complement to ultrasound, which is sufficient in visualizing the prostate, but insufficient in visualizing the seeds. Several groups have successfully combined the two imaging modalities for PPB, although most use radiation therapy simulators or encoded isocentric C-arms [14, 46, 66, 61, 12, 51, 28]. However, the most common fluoroscopic imaging device currently found in ORs across the world is the mobile non-isocentric C-arm, which in fact, is already used by many brachytherapists in addition to TRUS to occasionally verify needle or seed placement. Although more challenging, fusion of TRUS with such ubiquitous C-arms for seed localization would have a much wider impact than the specialized equipment used by a majority of groups. Therefore, in our system, three or more fluoroscopic shots are taken at arbitrary poses with a

mobile non-isocentric C-arm to image the seeds while the patient is still positioned on the surgical table with his legs in a high lithotomy position (see Figure 3). The three-dimensional (3D) seed locations are reconstructed from these two-dimensional (2D) X-ray images, which are subsequently registered to the TRUS prostate volume, making dynamic dose calculation possible. In order to track the C-arm, we also use a fiducial with radio-opaque features.

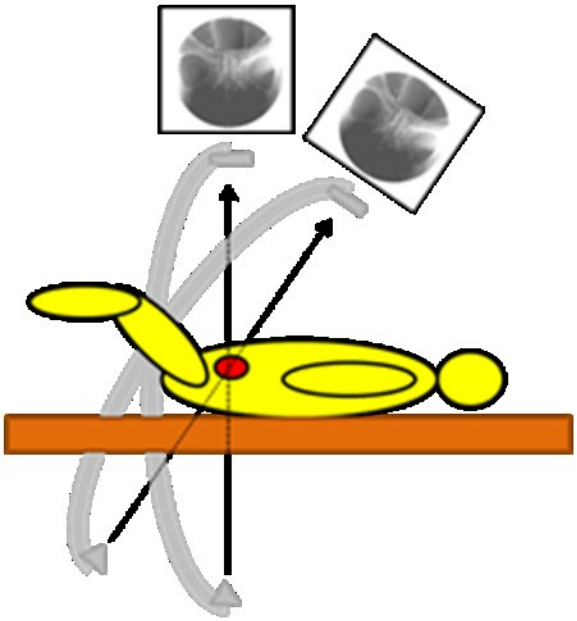

Figure 3 Several fluoroscopic images are needed to produce a 3D reconstruction of the seeds.

The second proposed intraoperative dosimetry system involves photoacoustic imaging. Recently, photoacoustic imaging has emerged as a promising new medical imaging modality suitable for various structural, functional, and molecular imaging applications [76]. It is based on the phenomenon known as the photoacoustic effect, simply defined as the conversion of electromagnetic waves to acoustic waves. The acoustic waves generated by the photoacoustic effect via a light source may be detected using a transrectal probe as is used in TRUS. Photoacoustic imaging would theoretically solve the brachytherapy seed localization problem since it would be capable of imaging the seeds more clearly than ultrasound. The number of false positives would be reduced because the metallic seeds would exclusively generate signal at specific wavelengths of light. The number of false negatives would also be reduced because the light source would be easily manipulated by fiber optic to illuminate all areas of the prostate. Moreover, photoacoustic

imaging would require little alteration to contemporary clinical practice since only the addition of a laser source is required (see Figure 4).

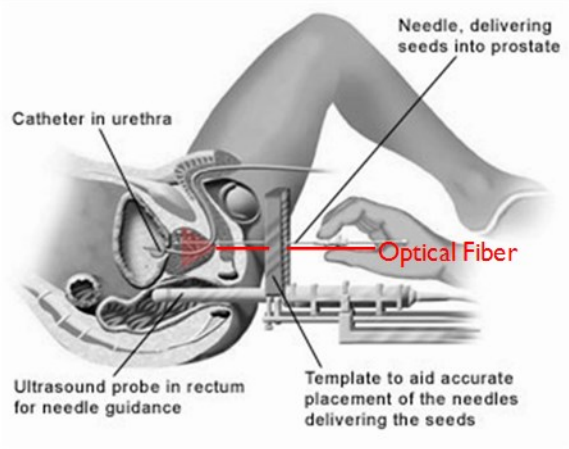

Figure 4 Photoacoustic imaging of seeds involves the simple addition of an optical fiber to contemporary PPB practice.

1.5 Primary Contributions

The following is a summary of my primary contributions to set the stage for more detailed descriptions in the upcoming chapters.

1. I developed an algorithm that simultaneously segments the tracking fiducial and brachytherapy seeds in fluoroscopic images without a region of interest (ROI), thereby minimizing the need for manual intervention. Image-based radiographic fiducials are often used to track non-encoded X-ray devices like the mobile non-isocentric C-arm, but manual intervention is typically needed to select proper ROIs for segmenting both the tracking fiducial and the seeds, to evaluate the segmentation results, and to correct the segmentations in the case of failure, thus requiring a significant amount of extra time in the OR. Through the innovative use of image processing techniques such as mathematical morphology, Hough transforms, and random sample consensus (RANSAC), my method also detects and separates overlapping seeds that are common in brachytherapy implant images. The details of this method are discussed in Chapter 2.
2. I developed our next generation TRUS-fluoroscopy intraoperative dosimetry system based around a simple marker-based fiducial. Most TRUS-fluoroscopy intraoperative dosimetry systems use encoded C-arms or other specialized X-ray equipment that are impractical to

incorporate into most clinics. Even systems based on the ubiquitous mobile non-isocentric C-arm have flaws throughout their imaging pipeline, resulting in dosimetry that is neither very accurate nor robust. Shifting the paradigm to a simpler marker-based fiducial, I integrated an intraoperative dosimetry system based on my previously developed seed segmentation algorithm, a newly created fiducial detection algorithm, and existing reconstruction and registration algorithms developed by my colleagues and myself. This system proves to accurately localize seeds in patients while detecting cold spots, effectively resolving the problem of seed localization in ITP. The details of this TRUS-fluoroscopy intraoperative dosimetry system along with the marker-based fiducial are described in Chapter 3.

3. I developed a prototype photoacoustic imaging system for visualizing brachytherapy seeds in a laboratory setting. While there are several approaches to seed localization, photoacoustic imaging has emerged as an ideal modality to address this challenge and is easily incorporated into the ultrasound system used in the OR. A photoacoustic imaging system was therefore built around a clinical ultrasound system to achieve the task of visualizing and localizing seeds. I performed several experiments to analyze the effects of various parameters on the appearance of brachytherapy seeds in photoacoustic images. I also imaged multiple seeds in an *ex vivo* dog prostate phantom to demonstrate the feasibility of using this system in a clinical setting. The initial results of this benchtop photoacoustic imaging system demonstrated how the appearance of the seeds varied with each tested parameter, and showed that multiple seeds are clearly visible in an *ex vivo* dog prostate. The details of this prototype system and its corresponding results are found in Chapter 4.
4. I developed the next generation photoacoustic imaging system for the localization of brachytherapy seeds in a clinical setting. The prototype photoacoustic imaging system described in the previous contribution demonstrated promising results, but it also had many limitations that prevented it from being implementable in the OR. System components needed to be upgraded and several practical issues regarding imaging configurations and signal optimization had to be addressed. The first known *in vivo* study of photoacoustic imaging for PPB was then conducted

with this upgraded photoacoustic system. Results show that multiple seeds are clearly seen in an *in vivo* dog prostate, but the experiments also raise some research questions that may be addressed in the future. The details of this next generation system and its corresponding results are found in Chapter 5.

Chapter 2. Automatic Segmentation of Fiducial and Seeds in Fluoroscopic Images

One of the key steps in any system that fuses TRUS and X-ray fluoroscopy for prostate brachytherapy is image segmentation. Even with the many advanced image processing technologies available today, segmentation is not a trivial task, especially on fluoroscopic images of the prostate, where many radio-opaque objects may appear in the field of view (FOV). The primary contribution of this work, previously presented at SPIE Medical Imaging [36] and published in Medical Engineering and Physics [31], is a fully automated seed and fiducial segmentation algorithm that detects and separates overlapping seeds without the need of a user-selected ROI. The strong results of this algorithm therefore permit the direct pipelining from image acquisition to seed reconstruction.

2.1 Introduction

The first of our proposed intraoperative dosimetry systems fuses TRUS and fluoroscopy to localize the seeds with respect to the prostate. There are several different approaches to seed localization even among TRUS-fluoroscopy based intraoperative dosimetry systems, but fluoroscopy using the ubiquitous mobile non-isocentric C-arm is a promising approach because it is already a standard means of imaging within the OR.

While we present our own latest intraoperative dosimetry system based on the mobile non-isocentric C-arm in Chapter 3, this current chapter covers research that was applied on a previous generation system and initially proposed by Jain et al. [20, 21]. In their system, TRUS is used to image the prostate while 3 or 4 C-arm X-ray shots are taken at arbitrary poses to image the seeds. The 2D X-ray images are used to reconstruct the 3D seed locations, which are subsequently registered to the TRUS prostate volume. In order to achieve accurate tracking of the C-arm and registration with the TRUS frame, they mount a radiographic tracking fiducial called FTRAC [22] (see Figure 5) to the needle-guiding

template in a mechanically calibrated position, thereby providing a transformation between X-ray and TRUS.

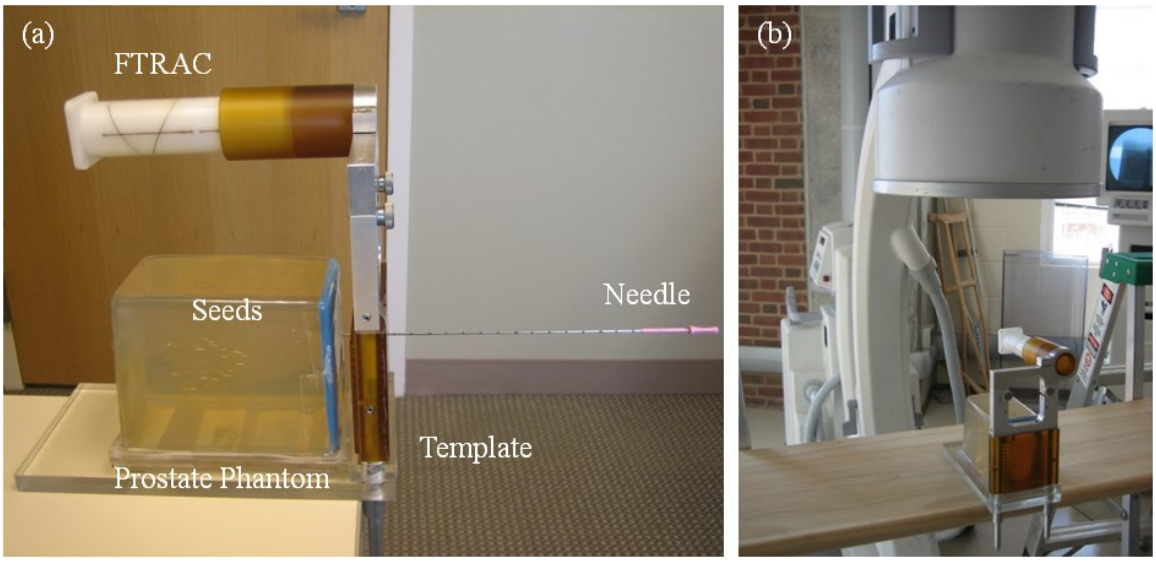

Figure 5 Phantom setup of the FTRAC. (a) View of the FTRAC setup. (b) Setup with non-isocentric mobile C-arm.

The system proposed by Jain et al. is very attractive as a practical solution for dynamic dose calculation, since it is cost-effective and may be easily adopted by minimally altering the contemporary TRUS-guided brachytherapy procedure. However, significant improvements may be made in the workflow of their system, especially in regards to segmentation. A key element to the described approach by Jain et al. is the fluoroscope tracking fiducial (FTRAC), a compact image-based tracking fiducial composed of radio-opaque beads (BBs), lines and ellipses (see Figure 6). The FTRAC is designed to solve two important issues for localizing seeds: 1) the estimation of the C-arm pose for seed reconstruction and 2) registration to the prostate volume computed from TRUS images. However, while most other portions of the system are fully automatic, current segmentation algorithms of the FTRAC [71] and the seeds [72] require operator intervention, bringing the entire pipeline to a halt. The reason for this is that both the FTRAC and the seeds are located in the same X-ray field of view, and current algorithms require the operator to outline an ROI each for the FTRAC and for the seeds so that these features may be processed separately. Even with properly selected ROIs, such algorithms often need further intervention because of automatic segmentation failure, in which case the operator has to manually correct or entirely resegment the features. There are several alternative seed segmentation algorithms available [69, 61], but none would eliminate the need of

user intervention since they also require the selection of an ROI in this framework. Overall, these drawbacks inhibit the workflow of ITP, which is problematic in the OR where time is of critical importance.

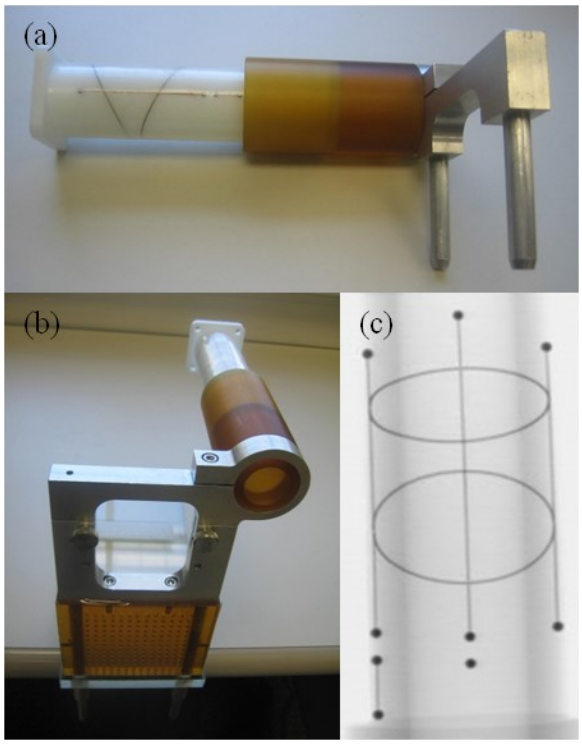

Figure 6 Figures of the FTRAC. (a) FTRAC attached to the mounting bridge. (b) FTRAC mounted on needle template. (c) X-ray image of the FTRAC.

In this chapter, we propose an ROI-free segmentation of both the radiographic tracking fiducial and the seeds. The purpose of this work is two-fold: 1) to accomplish fully automatic pipelining from image acquisition to seed reconstruction by removing the requirement of selecting ROIs and 2) to minimize manual intervention caused from automatic segmentation failures. Although we focus on the segmentation of the FTRAC, our methods may be easily applied to various radiographic tracking fiducials that use points, lines, or conics [25, 54].

2.2 Methods

Our proposed algorithm (see Figure 7) takes as input a single X-ray grayscale image and outputs the equations of the lines, the 2D image coordinates of the points, and the equations of the conics (note that

the FTRAC has 3 parallel lines, 9 BBs, and 2 ellipses) as well as the 2D image coordinates of the brachytherapy seeds. In cases when there are overlapping seeds in a projection view, the algorithm automatically classifies them as overlapping and outputs separated image coordinates. If desired, the resulting segmentation may be overlaid on the input image for visualization (see Figure 8). There are several assumptions made regarding the X-ray image, all of which are practical in the clinical setting: 1) the X-ray image has been corrected for geometric image distortion caused by the X-ray image intensifier, 2) the FTRAC and seeds are fully visible within the X-ray FOV, 3) the FTRAC appears to the right of the seeds without overlapping them, 4) the FTRAC is oriented upright, and 5) the TRUS probe is retracted and therefore not located in the FOV. Our algorithm was tested on Palladium-103 seeds which tend to appear small and oval in X-ray.

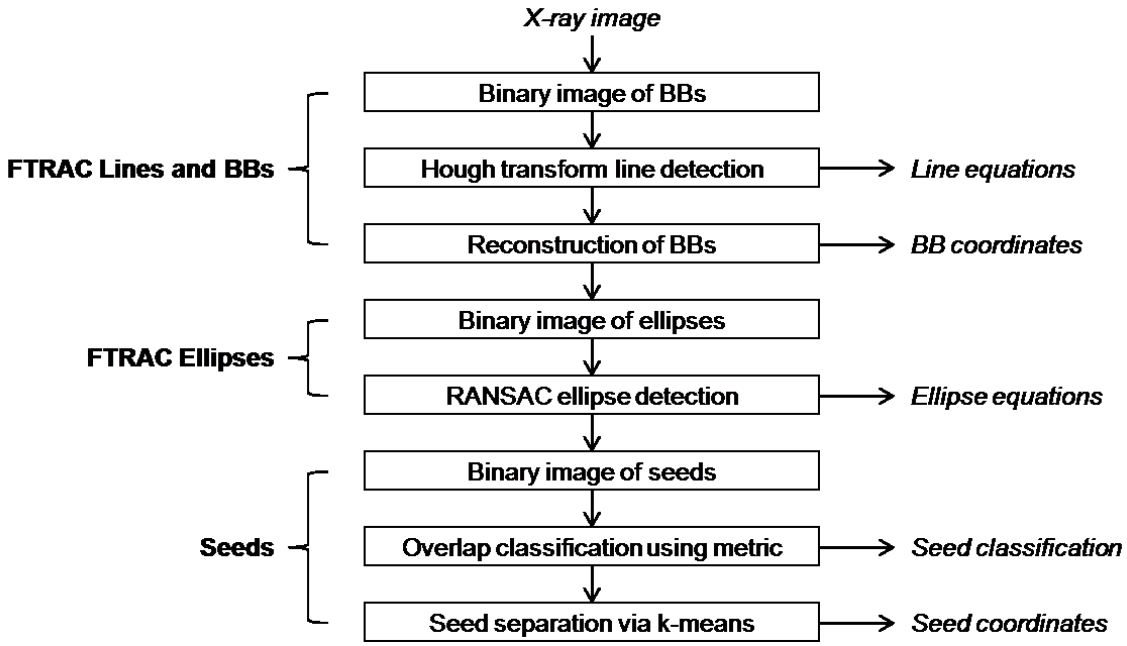

Figure 7 Flowchart of segmentation algorithm.

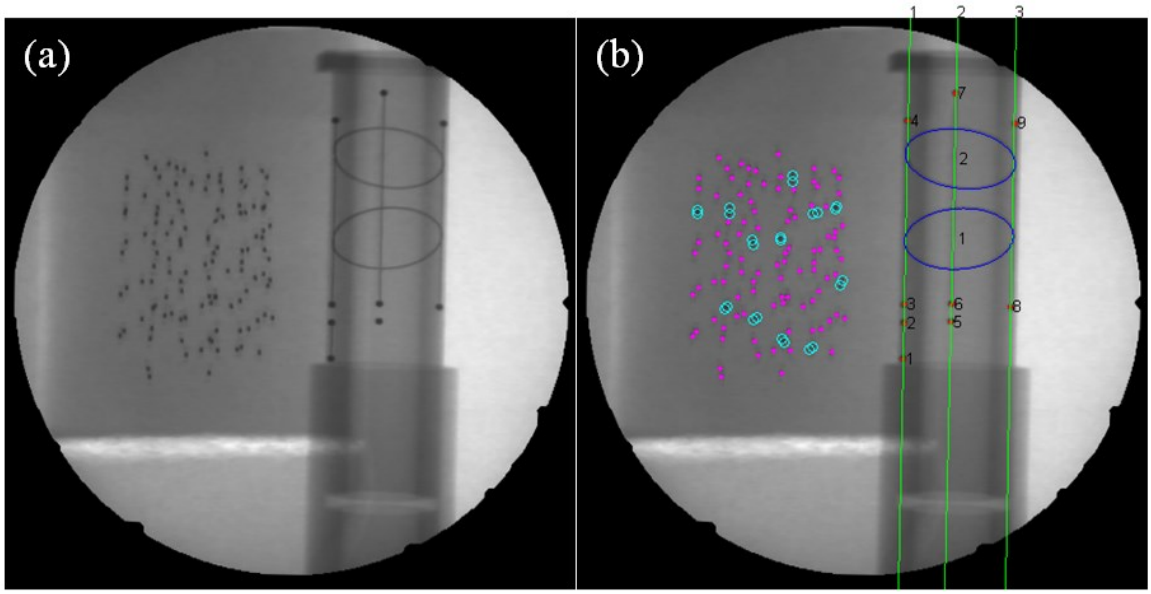

Figure 8 Sample phantom experiment segmentation. (a) Inputted original X-ray image. (b) Outputted segmentation of FTRAC lines (green), BBs (red dots), and ellipses (blue) as well as single (magenta dots) and overlapping (cyan circles) seeds overlaid on X-ray image.

2.2.1 Morphological image processing

As mathematical morphology [18] has proven fast and effective for segmenting various features such as points and edges, we first review morphological operations that are frequently applied to both binary and grayscale images in our segmentation process. The following four translation invariant morphological operations are especially important, forming a basis for other morphological operations. In these definitions, f is the input image and B is the structuring element.

Erosion: $\psi_\epsilon(f)(x,y) = \min_{\xi,\eta}[f(x+\xi, y+\eta) - B(\xi,\eta)]$

Dilation: $\psi_\delta(f)(x,y) = \max_{\xi,\eta}[f(x-\xi, y-\eta) + B(\xi,\eta)]$

Opening: $\psi_\delta(\psi_\epsilon(f))(x,y)$

Closing: $\psi_\epsilon(\psi_\delta(f))(x,y)$

Erosion and dilation may be described as nonlinear shape filters that replace a pixel with the minimum and maximum, respectively, of its neighborhood as indicated by a shaped structuring element. Opening and closing are standard combinations of erosion and dilation that are often used for filtering by shape.

There are also more advanced morphological operations used in our algorithm.

Conditional dilation: $\delta_B^k(f^m|f) = \delta_B^1\delta_B^1 \ldots \delta_B^1(f^m|f)$ k times, where $\delta_B^1(f^m|f) = \min[\psi_\delta(f^m), f]$

Reconstruction: $r_B(f^m|f) = \max_{k>1}[\delta_B^k(f^m|f)]$

Top-hat: $f - \psi_\delta(\psi_\epsilon(f))$

Top-hat by reconstruction: $f - r_B(\psi_\delta(\psi_\epsilon(f))|f)$

Conditional dilation is a stepwise region growing process, using repeated incremental dilations to grow the marker image f^m into the mask image f (note that every pixel in f^m must have a value less than or equal to that in f). It also provides a convenient means to describe morphological reconstruction, which is the end result of continuous conditional dilations. Top-hat is an operation involving the subtraction of an image by its opening, and is used to enhance contrast in an image. It may also be used along with reconstruction, hence top-hat by reconstruction, to provide more specific contrast depending on the structuring element. Figure 9 shows an example illustrating conditional dilation and reconstruction. Note that a reconstructed image by definition is equivalent to an image after numerous conditional dilations. However, the outputted reconstructed image is not necessarily equivalent to the inputted mask image. This is related to the nature of the min function in conditional dilation. In areas where the mask image f is less than the dilation $\psi_\delta(f^m)$, the mask image is chosen and thus reproduced; in other areas, the dilation is chosen rather than the mask and thus appears differently from the mask. Figure 10 shows an example of top-hat and top-hat by reconstruction. Note that these two operations often produce very different results.

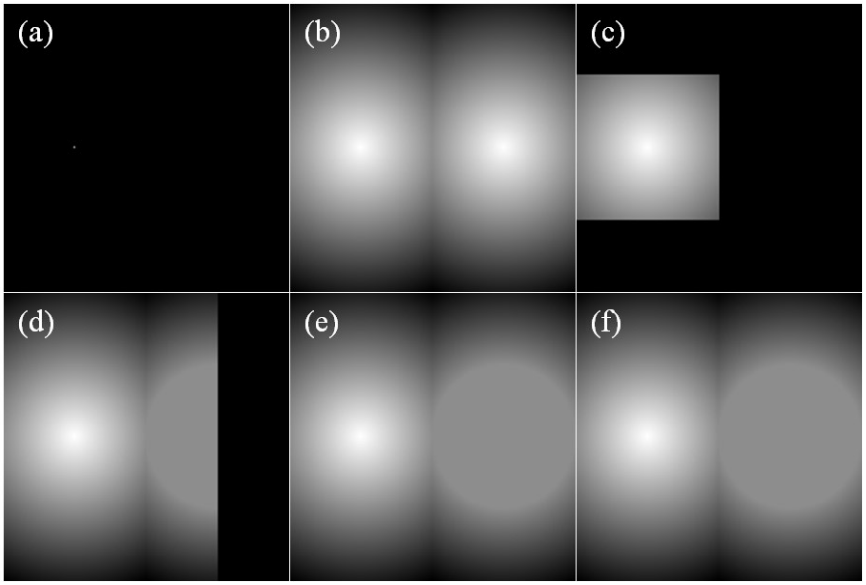

Figure 9 Grayscale examples of conditional dilation (using a 3×3 square structuring element) and reconstruction. (a) Marker image, $\boldsymbol{f^m}$. (b) Mask image, $\boldsymbol{f}$. (c) Image after 50 conditional dilations, $\boldsymbol{\delta_B^{50}(f^m|f)}$. (d) Image after 100 conditional dilations, $\boldsymbol{\delta_B^{100}(f^m|f)}$. (e) Image after 150 conditional dilations, $\boldsymbol{\delta_B^{150}(f^m|f)}$. (f) Reconstructed image, $\boldsymbol{r_B(f^m|f)}$.

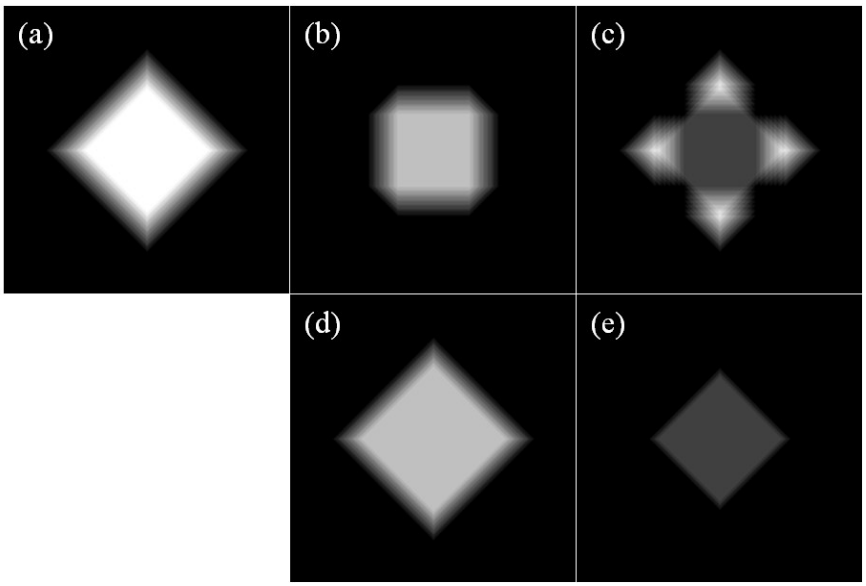

Figure 10 Grayscale examples of top-hat and top-hat by reconstruction (using a 50×50 square structuring element). (a) Original image, $\boldsymbol{f}$. (b) Image after opening, $\boldsymbol{\psi_\delta(\psi_\epsilon(f))}$. (c) Image after top-hat, $\boldsymbol{f - \psi_\delta(\psi_\epsilon(f))}$. (d) Reconstructed image of opening, $\boldsymbol{r_B(\psi_\delta(\psi_\epsilon(f))|f)}$. (e) Image after top-hat by reconstruction, $\boldsymbol{f - r_B(\psi_\delta(\psi_\epsilon(f))|f)}$.

The choice of structuring element (i.e., its size and shape) in these morphological operations depends on the object at hand. Since object size may vary depending on resolution and scale, the size of the structuring element must also adjust accordingly. However, once resolution and scale are fixed, the size of the structuring element may likewise remain fixed. Since object shape is not dependent on resolution or scale, the shape of the structuring element may remain constant regardless of these factors.

2.2.2 FTRAC Lines and BBs

The FTRAC has a fixed structure that may be exploited; in particular, the 9 FTRAC BBs are positioned by design coincidently on top of the 3 parallel FTRAC lines. This becomes the basis for our approach of segmenting the lines and BBs simultaneously.

The first objective is to obtain a clean binary image of the FTRAC BBs. To do so, we perform a top-hat by reconstruction operation using a disk-shaped structuring element on the complemented X-ray image and then binarize the image using Otsu's threshold [47] (see Figure 11a). The connected components [17] in the resulting binary image are then analyzed by properties such as area (i.e. the number of pixels in a connected region), eccentricity, solidity, and location to filter out objects that are not BBs (such as the implanted brachytherapy seeds). The 9 FTRAC BBs are distinguished from the majority of seeds and other remaining structures in the image due to their larger size, rounder shape, and location to the right side of the image. The result is a binary image containing the FTRAC BBs and very few if any remaining false detections (see Figure 11b).

Next, the FTRAC BBs are differentiated from false detections by the fact that they lie on lines that are oriented roughly in the vertical direction. To do this, the Hough transform [1] is applied to create a list of lines that pass through the pixels of the detected regions, sorted by their line strength. The FTRAC lines are always among the strongest lines output by the Hough transform since the BBs are large in size and since there are few false detections. The FTRAC lines are further distinguished because they comprise three lines that are parallel, roughly vertical, and are on the right side of the image (see Figure 11c). Since the Hough transform parameter space is fairly coarse (to reduce computation time), the three line positions are further refined. In particular, the three lines are fit using least squares to line edges produced from a thresholded top-hat operator using a vertical structuring element applied to the complemented source image

(see Figure 11d). This process yields three precise equations for the three FTRAC lines appearing in the source image.

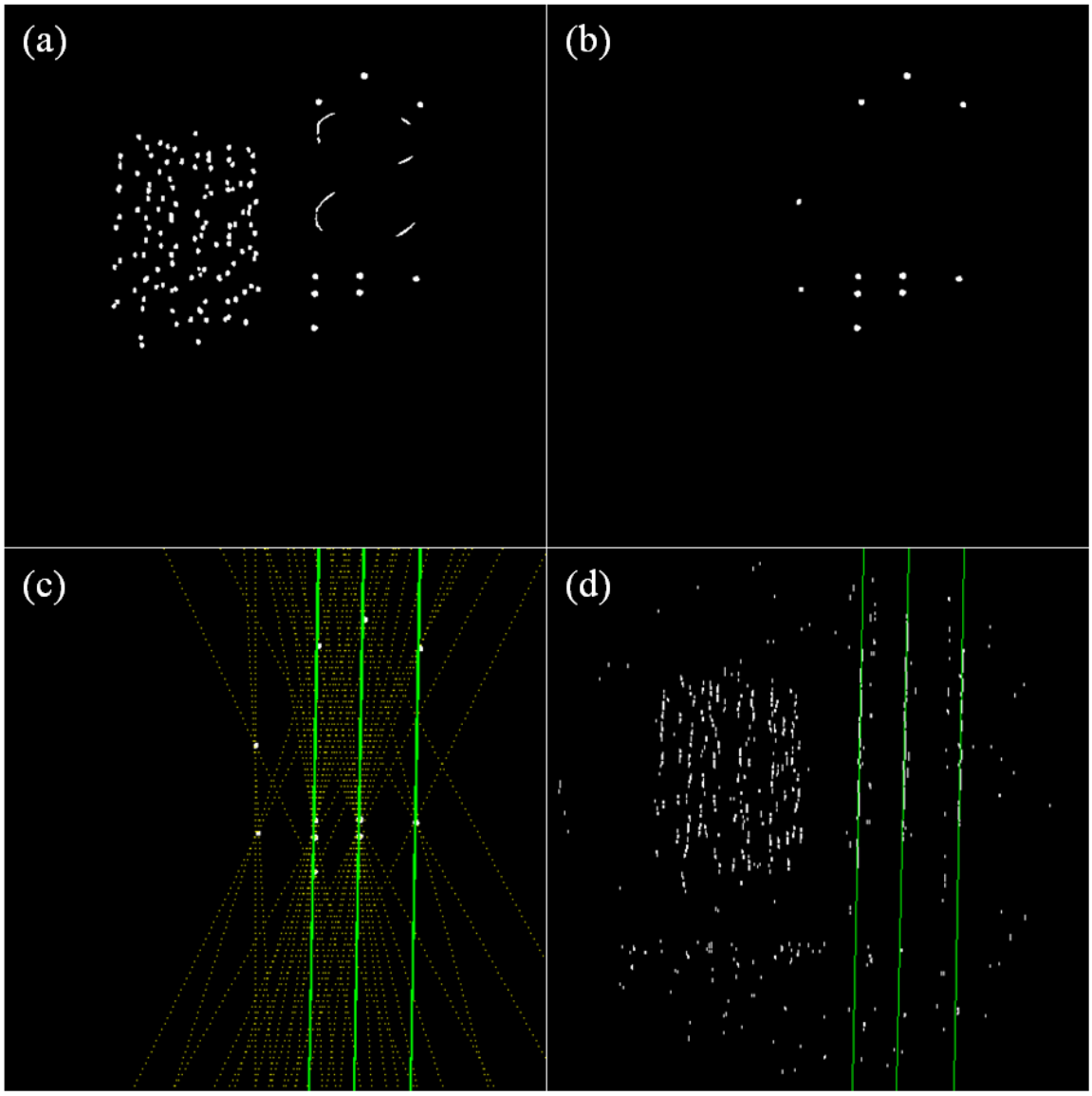

Figure 11 Sample phantom experiment FTRAC lines and BBs segmentation. (a) Binary BB image after applying Otsu's threshold. (b) Binary BB image after binary image processing. (c) FTRAC lines (green) selected from among roughly vertical Hough transform lines (yellow). (d) FTRAC lines better resolved by least squares fitting of detected vertical line edges.

Given the FTRAC lines, false BB detections are removed by applying morphological reconstruction to the binary image (see Figure 11b) using the intersections with the detected FTRAC lines

as the marker image. The centroids of the resulting connected components give the estimated positions of the 9 FTRAC BBs.

2.2.3 FTRAC Ellipses

Segmentation of the FTRAC ellipses is much easier given knowledge of the positions of the FTRAC lines and BBs for two reasons: 1) a rough estimate of the regions of the FTRAC ellipses may be gained from the FTRAC lines and BBs, and 2) the FTRAC ellipse edges may be distinguished from the FTRAC line edges. Still, determining the equations of the FTRAC ellipses is still a challenging task as ellipse detection in itself is still an ongoing research field.

Our first objective in ellipse detection is to obtain a binary image containing the ellipse edges. Naïve application of the Canny edge detector [4] yields double edges rather than a desired single edge since the ellipse boundaries are spike edges rather than step edges. Instead, we apply Otsu's threshold to the result of a top-hat operation using a square structuring element on the complemented input image (see Figure 12a). Further image processing follows, including 1) removing the edge pixels within a small range of the middle FTRAC line since it passes through the center of the two ellipses and thus interferes with ellipse detection, 2) filtering by area and shape using an opening with a square structuring element to remove spurious non-ellipse edges, and 3) thinning the edges of the binary image, which reduces complexity of ellipse detection by refining edges to have the width of a single pixel (see Figure 12b). These operations and their corresponding parameters are applied uniformly to all images.

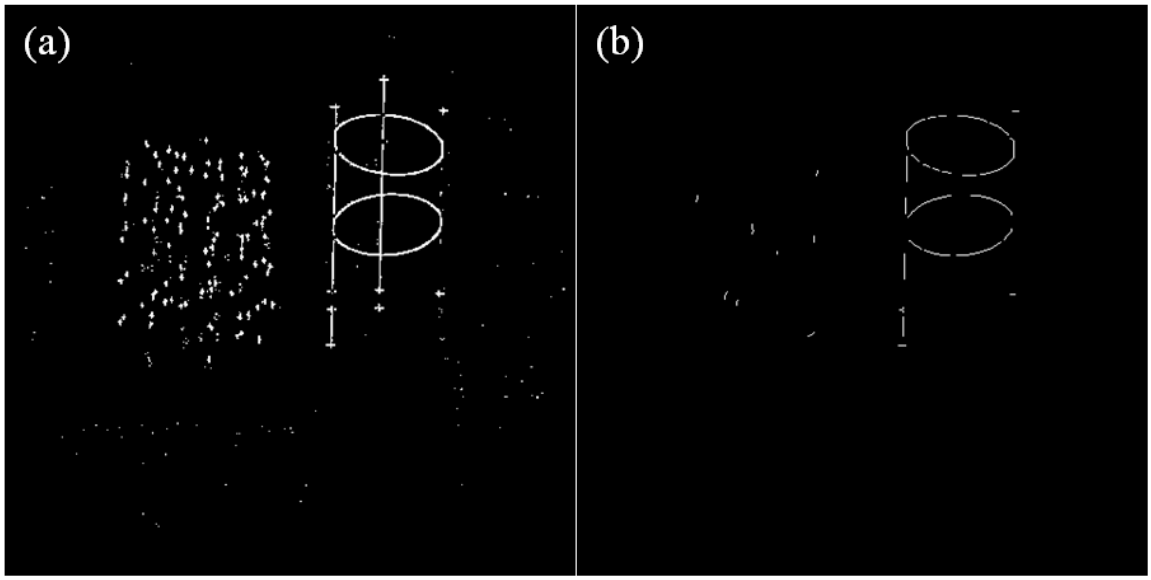

Figure 12 Sample phantom experiment FTRAC ellipses segmentation. (a) Binary ellipse edges image after applying Otsu's threshold. (b) Binary ellipse edges image after binary image processing.

At this stage, we have a binary image containing thinned FTRAC ellipse edges as well as a few remaining false edges. From here, we estimate an approximate region for each of the two FTRAC ellipses so an ellipse detection algorithm may subsequently determine the equations of the two ellipses separately. To do so, we exploit the now known positions of the FTRAC BBs to define an outer boundary around the ellipses. A dividing line between the two ellipse regions is then found by a two step process: first, by randomly positioning lines parallel and in between the now known outermost FTRAC lines to search for lines with four intersections, presumably two intersections per ellipse; and second, by finding the average point between the two innermost intersections out of the four total intersections. Such an average point then defines a horizontal line to separate the two ellipse regions.

Just as with lines, there exists a Hough transform for detecting ellipses. However, the generalized Hough transform is impractical for this application since it requires a large amount of memory. As an alternative, we used an ellipse detection algorithm based on RANSAC [11], which is a technique to fit instances of a model (in our case, ellipses) to data even in the presence of numerous outliers. The RANSAC framework requires code for a model fitting method and an error distance measurement, both of which already exist in the case of ellipses. We therefore implemented our RANSAC-based ellipse detection

algorithm with the aid of pre-existing code, including the numerically stable ellipse fitting algorithm developed by Halir and Flusser [15] and the point-to-ellipse distance calculation described by Xie and Ohya [78]. Using edge pixels selected within each of the previously estimated FTRAC ellipse regions, our ellipse detection algorithm then determines the equations of the two FTRAC ellipses.

2.2.4 Seeds

Segmentation of the FTRAC projection elements simplifies seed segmentation because the seeds may be distinguished from potentially similar appearing features of the FTRAC, such as the BBs. However, seed segmentation at this point is not trivial because: 1) other objects in the entire field of view may appear as seeds, and 2) seeds may overlap one another in the image making it difficult to identify their locations.

To segment the seeds we first obtain a binary image of the seeds by thresholding the top-hat by reconstruction of the complemented image using a disk-shaped structuring element (see Figure 13a). We chose a disk-shaped structuring element over a rectangular-shaped one since seeds may appear in any orientation. After removing the FTRAC region using a bounding quadrilateral determined by the FTRAC BBs and lines, we are left with a binary image of the seeds and some spurious seed-like artifacts (see Figure 13b). To remove these false positives, we take advantage of the fact that seeds are typically positioned close to one another. Therefore objects that are greater than an empirically determined threshold distance from the densest seed region are assumed to be false positives and removed from the binary image. Such spurious detections are rare (and we do not see such an artifact in Figure 13b) because the densest objects in the image are usually associated with either the seeds or the FTRAC BBs; but occasionally the urethral catheter used during surgery bends in such a way as to produce an artifact (see Figure 17b), and this step is typically effective in removing it.

At this point we have a binary image comprising only seeds, but some of these seeds are overlapping. We identify overlapping seeds based on the following physical principle. Assume a single seed with uniform attenuation coefficient μ is placed in a radio-transparent medium. According to Beer's Law,

$$I(x,y) = I_0 e^{-\mu \int dz}$$

where $I(x,y)$ is the image intensity at position (x,y), $I_0$is the original X-ray intensity, and z is orthogonal to the image plane along the line of projection. We may rearrange this equation to obtain:

$$-\ln\frac{I(x,y)}{I_0} = \mu\int dz$$

$$\iint -\ln\frac{I(x,y)}{I_0}dxdy = \mu\iiint dxdydz = \mu V$$

Here, V is the volume of a single seed and is clearly constant irrespective of the projection direction. Moreover, if there are n seeds in the projection, then the total volume is nV, and the resulting value to the double integral is $n\mu V$. Therefore the calculation of $\iint -\ln\frac{I(x,y)}{I_0}dxdy$ over each connected seed region of the image may serve as a metric for identify overlapping seeds, with the resulting value being constant for a single seed, double the constant for two overlapping seeds, triple for three seeds, and so forth.

There are several issues to consider when implementing this principle. First, seeds are not actually placed in a radio-transparent medium as described above since the patient anatomy surrounding the seeds has some degree of radio-opaqueness. Moreover, we generally do not know the value of the source intensity I_0. Nonetheless, the complemented top-hat by reconstruction that was previously calculated may effectively solve these two issues and represent $\frac{I(x,y)}{I_0}$ in this strategy. This is made possible since top-hat by reconstruction not only enhances contrast but removes nearly all background effects in the process. As a result, this emulates a normalized projection of seeds through a radio-transparent medium, evaluating to 1 at positions (x,y) where there is no seed and a value between 0 and 1 where there is a seed (see Figure 13c). Another issue to consider is that the image is digital, so rather than calculate a double integral, we calculate a double summation. Finally, we also do not know the actual value of μV. However, this value may be estimated by taking the median value of this metric among all the connected regions, since in general the vast majority of regions are single seeds. Therefore, all seeds visible from regions with a metric value greater than a defined threshold are considered overlapped seeds, and these indications are included as an output of the algorithm.

The final step is to determine the positions of the individual seeds identified above to be in overlapping regions. We use the facts that palladium seeds in X-ray are small and appear Gaussian shaped

in intensity (see Figure 13d and e), and that the k-means [53] clustering algorithm works particularly well with Gaussian distributed data. Briefly, the k-means algorithm takes an array of data values (which might be vectors) as input and, given a user-specified number of clusters, outputs the cluster means and the cluster classification for each data point. In our case, each pixel of a particular overlapping region is set up as a data point multiple times according to the intensity of that pixel. For example, if pixel (50,100) has intensity value of 128 in 256-grayscale, there would be 128 instances of the data point (50,100) in the input to k-means. The previously described metric also provides a good estimate for the number of seeds n found in an overlapping region and is therefore used as the number of clusters input to the k-means algorithm. The cluster means determined by k-means are the estimated positions of seeds found in overlapping regions. The positions of the remaining seeds found in non-overlapping regions are calculated by each region's centroid (see Figure 13f).

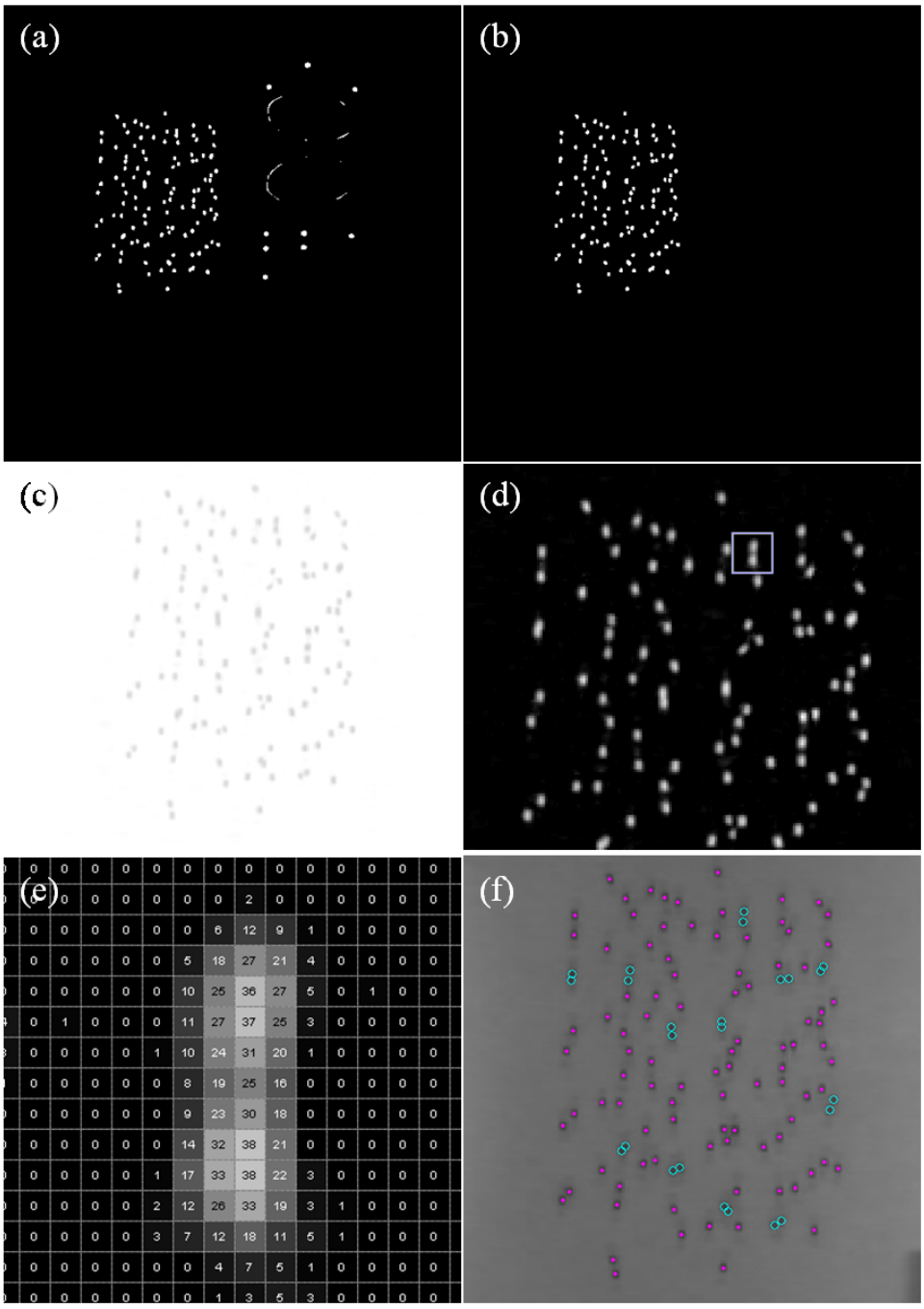

Figure 13 Sample phantom experiment seeds segmentation. (a) Binary seeds image after applying Otsu's threshold. (b) Binary seeds image after removing FTRAC. (c) Magnified complemented top-hat by reconstruction used to calculate metric for seed classification. (d) Magnified image of seeds with an example of overlapping seeds in rectangle. (e) Gaussian-like intensity distribution of overlapped seeds in rectangle of (d). (f) Magnified image of final seed segmentation.

Figure 14 through Figure 17 demonstrate a second example of the steps in our algorithm, this time for a clinical case that is also presented in our results.

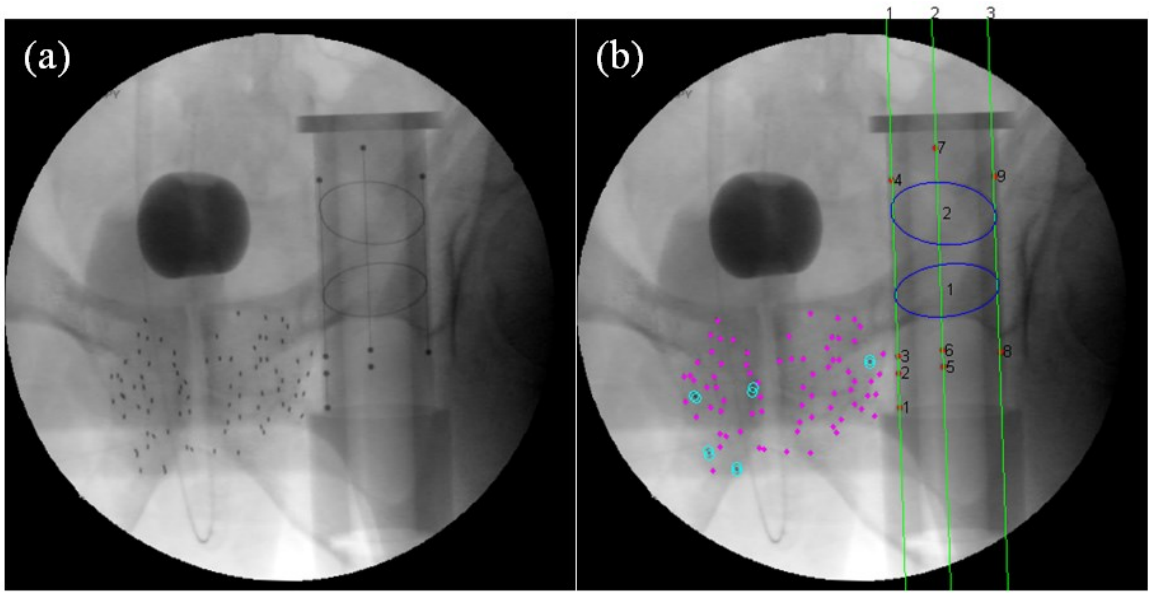

Figure 14 Sample clinical study segmentation. (a) Inputted original X-ray image. (b) Outputted segmentation of FTRAC lines (green), BBs (red dots), and ellipses (blue) as well as single (magenta dots) and overlapping (cyan circles) seeds overlaid on X-ray image.

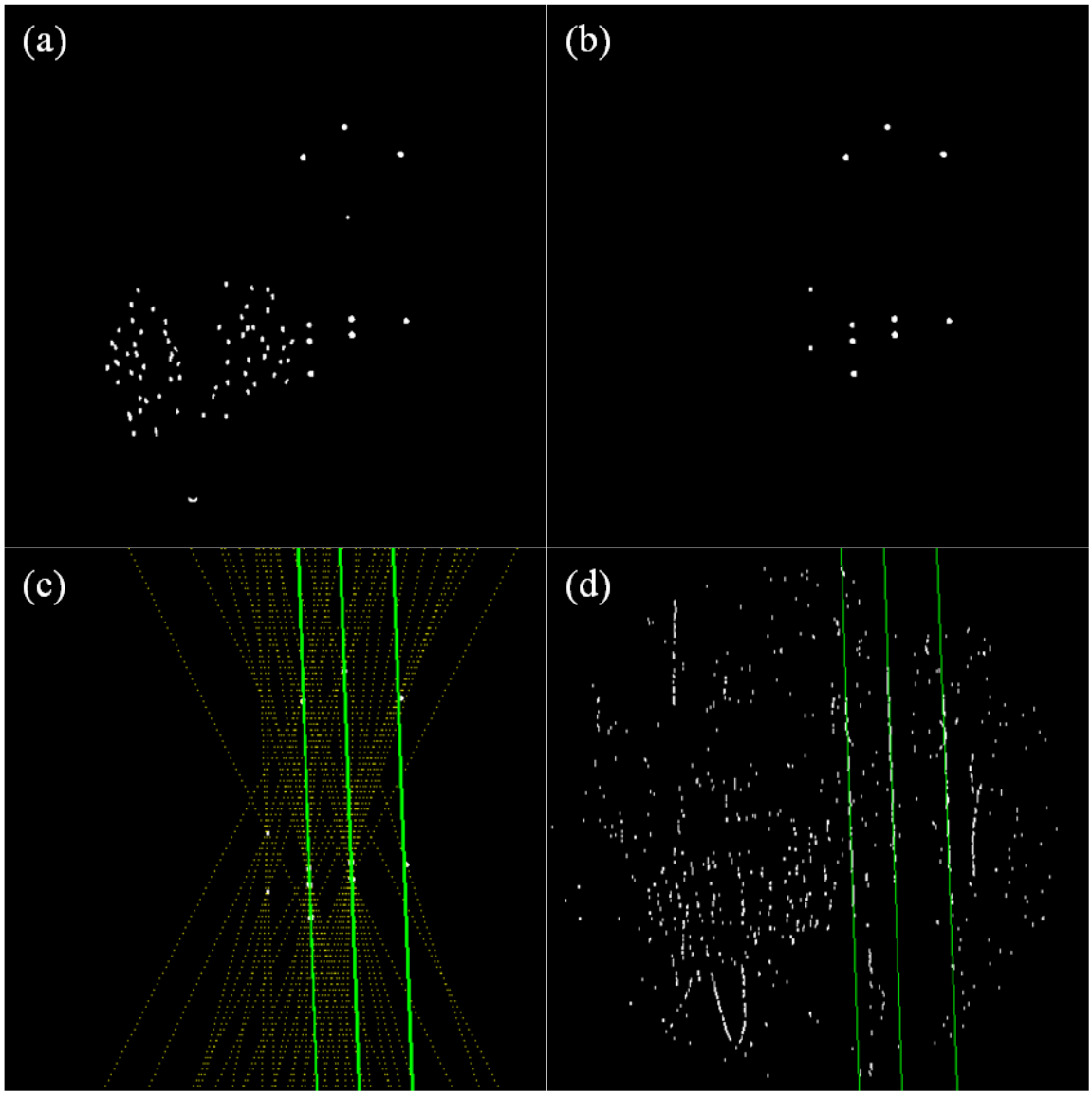

Figure 15 Sample clinical study FTRAC lines and BBs segmentation. (a) Binary BB image after applying Otsu's threshold. (b) Binary BB image after binary image processing. (c) FTRAC lines (green) selected from among roughly vertical Hough transform lines (yellow). (d) FTRAC lines better resolved by least squares fitting of detected vertical line edges.

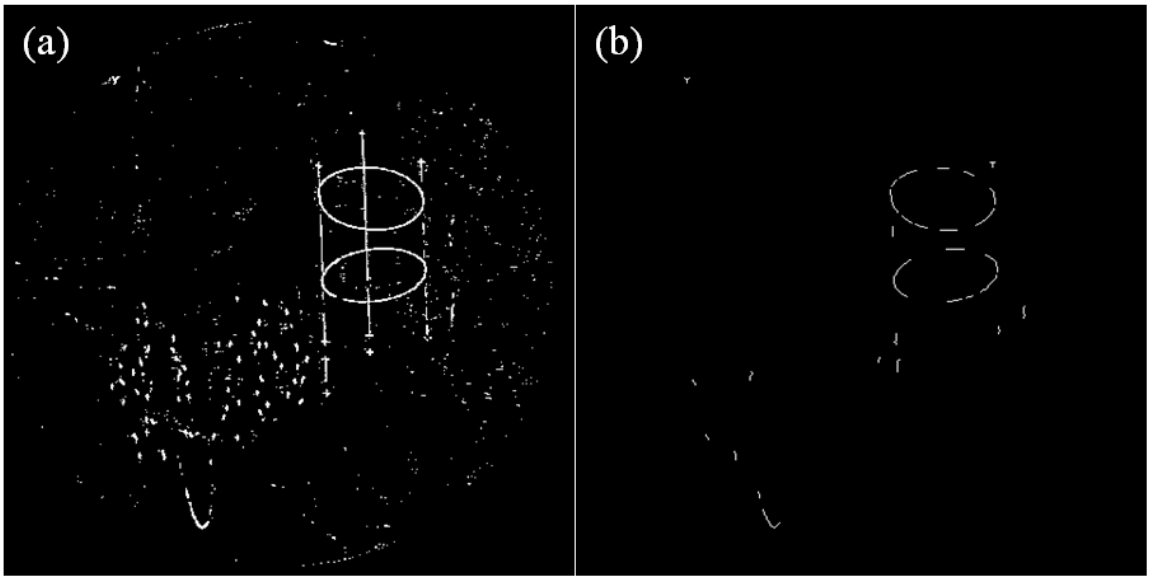

Figure 16 Sample clinical study FTRAC ellipses segmentation. (a) Binary ellipse edges image after applying Otsu's threshold. (b) Binary ellipse edges image after binary image processing.

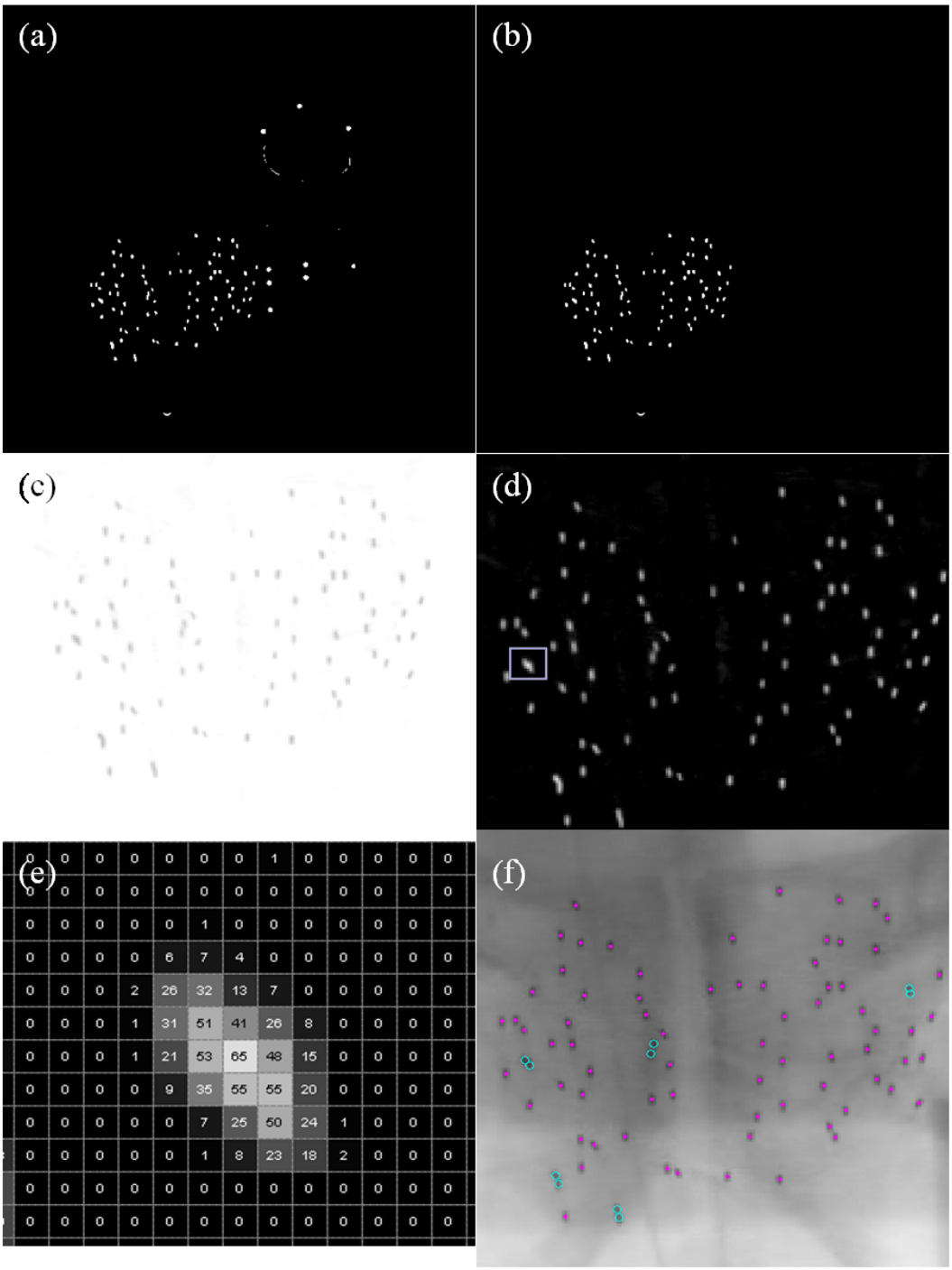

Figure 17 Sample clinical study seeds segmentation. (a) Binary seeds image after applying Otsu's threshold. (b) Binary seeds image after removing FTRAC. (c) Magnified complemented top-hat by reconstruction used to calculate metric for seed classification. (d) Magnified image of seeds with an example of overlapping seeds in rectangle. (e) Gaussian-like intensity distribution of overlapped seeds in rectangle of (d). (f) Magnified image of final seed segmentation.

2.3 Results

The algorithm was tested on 55 phantom and 206 clinical images. X-ray images were taken with an OEC 9600 (GE Healthcare, Milwaukee, WI, USA) for phantom images and an OEC 9800 (GE Healthcare, Milwaukee, WI, USA) for clinical images using an analog NTSC video output with an image size of 720x480 pixels and a pixel resolution of 0.44 mm x 0.44 mm. Although it is possible to use digital DICOM images, they generally cannot be retrieved quickly in the OR.

The outputs of the algorithm were compared to manually corrected automatic segmentations of the FTRAC and the seeds. The manually corrected segmentation of the FTRAC was first computed using an automatic algorithm requiring an ROI [71]. Manual corrections followed, with the BBs segmented by choosing the nearest darkest points to the user's selected points, the lines by performing least squares fitting of the 5 points per line that the user selects, and the ellipses by least squares fitting of the 7 points per ellipse that the user selects. As with the FTRAC, the manually corrected segmentation of the seeds was first computed by an automatic algorithm requiring an ROI [72], and then followed by any manual corrections. All manual segmentations were done by a well trained operator who had hundreds of cases of experience segmenting the FTRAC and seeds. In the most difficult cases where it is unclear whether a seed is overlapped, multiple poses were examined to verify the correct manual segmentation. Automatic segmentations of both the FTRAC and the seeds in the proposed algorithm required 5 seconds per image on average when running on a PC with a 2.33 GHz Intel Core 2 Duo processor.

Differences between manually corrected and automatic segmentations of the FTRAC are included in Table 1 through Table 4 and were calculated as follows. Let the subscripts m and a represent the manually corrected and automatic segmentations, respectively. BB segmentation differences are calculated using the Euclidean distance between the two BB coordinates, (x_m, y_m) and (x_a, y_a). For line segmentation differences, let ρ and θ represent the parameters for the equation of a line, such that

$$x\cos\theta + y\sin\theta = \rho.$$

The difference in perpendicular distance to origin is $|\rho_m - \rho_a|$ and the difference in angle is $|\theta_m - \theta_a|$. For ellipse segmentation differences, let h, k, a, b, θ be the parameters for the equation of an ellipse, such that

$$\frac{\left((x\cos\theta+y\sin\theta)-h\right)^2}{a^2}+\frac{\left((-x\sin\theta+y\cos\theta)-k\right)^2}{b^2}=1.$$

The difference in center position is calculated as $\sqrt{(h_m-h_a)^2+(k_m-k_a)^2}$, the difference in major axis is $|a_m-a_a|$, the difference in minor axis is $|b_m-b_a|$, and the difference in orientation is $|\theta_m-\theta_a|$. Finally, for pose estimation differences, pose is calculated from the FTRAC segmentations using the pose recovery mathematics provided by Jain et al. [22] and is given in the homogeneous form

$$\begin{bmatrix} r_{11} & r_{12} & r_{13} & t_x \\ r_{21} & r_{22} & r_{23} & t_y \\ r_{31} & r_{32} & r_{33} & t_z \\ 0 & 0 & 0 & 1 \end{bmatrix},$$

where r_{ij}represents entries in the rotation matrix R, and t_i represents entries in the translation vector T. Difference in rotation angle is thus computed as $\cos^{-1}(\mathrm{trace}(R_aR_m^{-1})/2)$, and translation difference is computed as $|t_m-t_a|$ for each of the three axes.

Table 1 BB segmentation differences [root mean square (mm)].

BB #	Phantom	Clinical
1	0.2699	0.2431
2	0.3000	0.2464
3	0.2658	0.2405
4	0.2650	0.2635
5	0.2356	0.2332
6	0.2496	0.2616
7	0.1965	0.2759
8	0.1905	0.3038
9	0.1625	0.2481

Table 2 Line segmentation differences (mean ± std).

Data	Line #	Distance (mm)	Angle (degrees)
Phantom	**1**	0.3252 ± 0.2194	0.1314 ± 0.1114
	2	0.4521 ± 0.5130	0.2464 ± 0.2431
	3	0.6321 ± 0.4625	0.2304 ± 0.2077
Clinical	**1**	0.4260 ± 0.3798	0.2436 ± 0.2002
	2	0.4037 ± 0.3428	0.2566 ± 0.1928
	3	0.5269 ± 0.4018	0.2916 ± 0.2221

Table 3 Ellipse segmentation differences (mean ± std).

Data	Ellipse #	Center (mm)	Major axis (mm)	Minor axis (mm)	Orientation (degrees)
Phantom	**1**	0.2181 ± 0.0911	0.0970 ± 0.0773	0.0825 ± 0.0583	0.7119 ± 0.6463
	2	0.4136 ± 0.3598	0.4059 ± 0.5602	0.0919 ± 0.0819	0.5068 ± 0.6510
Clinical	**1**	0.2325 ± 0.1531	0.1952 ± 0.2821	0.1165 ± 0.1554	0.5861 ± 0.5163

	2	0.3462 ± 0.7220	0.2961 ± 0.7829	0.1558 ± 0.2112	0.8534 ± 1.0834

Table 4 Pose estimation differences (mean ± std).

Data	Rotation angle (degrees)	x (mm)	y (mm)	z (mm)
Phantom	0.3362 ± 0.2277	0.0698 ± 0.0481	0.0623 ± 0.0551	1.6546 ± 0.9500
Clinical	0.3965 ± 0.3228	0.0904 ± 0.0674	0.0925 ± 0.1316	2.1118 ± 2.7820

Table 5 Seed segmentation results.

Data	Patient	Number of Seeds	Detection Rate	False Positive Rate
Phantom	**Phantom**	20	98.1%	0.6%
		40	97.8%	0.3%
		60	97.3%	0.2%
		80	95.5%	0.0%
		100	94.9%	0.0%
		120	95.4%	0.3%
	Phantom Overall	-	95.9%	0.2%
Clinical	**1**	22	95.4%	3.7%
		44	99.3%	2.3%
		65	98.6%	2.7%
		66	98.9%	2.0%
	2	39	99.4%	2.0%
		82	98.9%	3.0%
		84	97.6%	2.9%
	3	33	99.6%	5.0%
		67	98.8%	3.0%
		70	99.0%	4.7%
	4	35	99.2%	4.1%
		68	99.7%	3.3%
		77	98.7%	1.6%
	5	24	100.0%	0.8%
		48	98.3%	1.7%
		53	99.0%	1.3%
	6	33	98.5%	0.8%
		61	99.8%	0.7%
		66	99.1%	0.9%
	7	81	99.5%	3.6%
	Clinical Overall	-	98.9%	2.6%

2.3.1 Phantom Experiments

A phantom was created with gelatin and implanted with 5 different seed configurations comprising 20, 40, 60, 80, 100, and 120 seeds, respectively. A total of 55 images (10 images for 20 seeds

and 9 images for the other cases) were taken at various C-arm poses as would be done in a clinical setting (see Figure 8).

For FTRAC segmentation, our algorithm was able to segment 53 of the 55 distortion corrected phantom images successfully, resulting in a 96.4% success rate. We define successful segmentation here as having less than 2 degrees difference in rotation angle compared to manually corrected segmentation, using pose as the standard since it is a simple unifying metric for all the feature segmentations of the FTRAC. Moreover, current reconstruction algorithms may handle pose errors of less than 2 degrees with greater than 97.5% success rate [39]. Segmentation failure may therefore result either by failing to produce segmentation outputs for all features, or by inaccurately segmenting features so large differences in rotation angle occur. A sample result is shown in Figure 8, and differences in the successful automatic FTRAC segmentations of the phantom images and their manually corrected counterparts are shown in Table 1 through Table 4.

For seed segmentation, our algorithm detected 3485 seeds while there were 3629 seeds. 3479 detected seeds from our algorithm matched to the manually corrected seeds, resulting in a 95.9% seed detection rate and a 0.2% false positive rate. More specific results are recorded in Table 5.

2.3.2 Clinical Study

A total of 206 patient images were collected from 7 patients under the Institutional Review Board's approved protocols at the Johns Hopkins Hospital. For all patients, Palladium-103 seeds (Theragenics®, GA, United States) were implanted. The X-ray images were taken at various C-arm poses, and the number of implanted seeds varied from 22 to 84 seeds (see Figure 14).

44 of the 206 clinical images were not properly taken with the complete FTRAC in the field of view, therefore failing to satisfy one of the assumptions of our algorithm. Of the remaining 162 images, 143 FTRAC segmentations were successful resulting in an 88.3% success rate. A sample result is shown in Figure 14, and quantitative differences between successful automatic and manually corrected segmentations are also shown in Table 1 through Table 4 within the row or column labeled "Clinical".

For seed segmentation, 13 among the 143 images with successful FTRAC segmentations were improperly taken with the TRUS probe in the field of view, being useful for FTRAC segmentation

development but inappropriate for seed segmentation evaluation**.** Consequently, in the remaining 130 images, our algorithm detected 7118 seeds while there were 7014 seeds. 6936 detected seeds in our algorithm matched to the manually corrected segmented seeds, resulting in a 98.9% seed detection rate but a 2.6% false positive rate. More specific results are also recorded in Table 5.

2.4 Discussion and Conclusion

We have developed an algorithm to simultaneously segment the FTRAC and the seeds while effectively identifying and separating overlapped seeds. The end result is a pipelined seed reconstruction system for prostate brachytherapy and minimized manual intervention caused by segmentation failures.

With the addition of this algorithm, processing begins immediately after image acquisition, so the steps of distortion correction, FTRAC segmentation, seed segmentation, and pose estimation are automatically pipelined. Once three images are acquired, seed reconstruction (using a technique described elsewhere [39]) completes the pipeline so that dose distribution calculations may be obtained. All computations are easily completed within the tens of seconds it takes for the technician to rotate the C-arm to the proper pose for acquiring the next X-ray image.

Although the algorithm fulfills its purpose, there are a few items that require caution. First, this algorithm uses the FTRAC fiducial, which is sensitive to segmentation differences along the depth (z) direction (see Table 4) and is not yet commonly used in brachytherapy procedures. However, since most fiducials are likewise composed of lines, BBs, and/or ellipses, there is high confidence that the fiducial segmentation techniques used in this algorithm may be generalized to other fiducials. Secondly, our algorithm was only tested for implants of Palladium-103 seeds, not for implants of Iodine-125 seeds that are also commonly used in many clinics. Since iodine seeds appear larger and more rectangular than palladium seeds under X-ray, it is unknown whether our algorithm will show similar segmentation performance on iodine seeds. However, it is important to note that the theory for segmenting palladium seeds and iodine seeds is similar, and the general steps of morphological processing, calculating the double summation, and applying k-means would likely be applicable to iodine seeds also. Finally, while this algorithm is able to resolve most overlapping seeds in projection images, it is unable to completely identify

every seed in the image, especially in cases where one seed completely hides another. However, there are many existing matching-based [39, 29] and tomosynthesis-based [70, 40] reconstruction algorithms that may handle this "hidden seed" problem as well as the potential issue of reconstructing images with differing number of detected seeds.

A few algorithms have already been proposed for seed segmentation. Tubic et al. [69] have proposed a seed segmentation algorithm similarly based on morphological processing while also resolving overlapped seeds. However, there are several key differences between our work and theirs, including the choice in automatic threshold selection, overlapped seed analysis, and approach for resolving overlapped seeds. While we apply Otsu's threshold, a double summation metric, and k-means, Tubic et al. uses the bidimensional entropy method, analysis by connected region properties, and simulated annealing. Our work has a higher seed detection rate than their algorithm, boasting higher than a 96% detection rate compared to their 92% detection rate. Su et al. [61] have also proposed a seed segmentation algorithm. In their work, they have resolved overlapped seeds through a simulation study using Gaussian classifiers and geometric analysis of clusters. Although they have done extensive work on simulation and phantom studies, they have not presented any clinical results. Moreover, they present segmentation and cluster analysis time of 1 minute per projection.

While our algorithm is not perfect, it certainly improves the current workflow. At their worst, previous algorithms would require the operator to travel back and forth from C-arm to console, impeding with the multiple responsibilities of operating the C-arm, specifying ROIs, inspecting the results, and manually correcting segmentations, which may take as much as several additional minutes in the OR. Even at their best, they would still require the operator to divert attention away from orienting the C-arm and towards managing ROIs on the computer. On the other hand, at its best, our algorithm would allow the operator to focus almost exclusively on the C-arm, only requiring him to take a glance from his position at the C-arm to verify the results, and being limited only by his speed in C-arm operation. Even at its worst, the operator always has the option to take another X-ray image at a slightly adjusted C-arm position to allow the pipeline another chance to run successfully, or he may manually correct segmentation errors as would be needed in the case of failure regardless of segmentation algorithm.

We have presented our work for simultaneously segmenting the FTRAC and brachytherapy seeds. Through innovative use of image processing techniques, our method is able to give satisfactory results for both FTRAC and seed segmentation. Moreover, image acquisition and preprocessing is pipelined without need for manual intervention, saving crucial time in the OR and improving dynamic dosimetry system performance.

Chapter 3. Ultrasound-Fluoroscopy Intraoperative Dosimetry Based on a Marker-Based Fiducial

Even with an automatic fiducial and seed segmentation algorithm, complex fiducials with lines and conics are cumbersome in several ways. Moreover, existing TRUS-fluoroscopy based intraoperative dosimetry systems also present many other drawbacks in localizing seeds. Nonetheless, it is challenging to find better tracking solutions or to significantly improve existing systems unless an alternative fundamental approach is taken. The primary contribution of this work, previously presented at SPIE Medical Imaging [32], is therefore a next generation TRUS-fluoroscopy based intraoperative dosimetry system and the paradigm shift offered by a simple marker-based fiducial. Extensive clinical analysis of this system shows that it produces outstanding results while reducing opportunities for error.

3.1 Introduction

As mentioned in the previous chapter, Jain et al. [20, 21] has proposed a prototype intraoperative dosimetry system based on TRUS and mobile non-isocentric C-arm fluoroscopy that is capable of localizing seeds, but even so, their system leaves some things to be desired. Their premise for intraoperative dosimetry is to register a 3D fluoroscopic reconstruction of seeds to a corresponding 3D TRUS prostate volume. A central component to their system is the fluoroscope tracking fiducial (FTRAC) [22], a compact tube-like fiducial composed of several radio-opaque features such as points, lines, and ellipses. The FTRAC is an innovative method to recover the poses from the non-encoded C-arm that are needed for reconstruction, since image processing algorithms may estimate the C-arm source position from the unique appearance of the fiducial in a 2D projection image. Moreover, the FTRAC is fixed firmly above the patient's abdomen to the stepper guiding the TRUS probe, therefore also providing the necessary link between the fluoroscopy and ultrasound coordinate systems that is needed for registration. Although

the FTRAC has such features, it also has significant drawbacks. First, the FTRAC restricts fluoroscopic acquisition because the technician must position the C-arm in at least three distinct poses where the FTRAC and seeds are in the same field of view yet do not overlap. This is a challenging task since the C-arm already has little room to maneuver as the C-arm detector is typically confined to a small space between the raised legs of the patient in the lithotomic position. Second, the FTRAC complicates segmentation because of the different types and the number of features that need to be segmented. Although automatic segmentation algorithms exist [71, 31], no algorithm is fail-proof, and manual segmentation of points, lines and ellipses is both tedious and time-consuming. Finally, the mechanical registration that comes with the FTRAC is unsatisfactory. There are significant errors due to prostate deformation, as the TRUS probe must be inserted to capture TRUS images but is removed to capture fluoroscopic images. It is also reported that seed localization in an FTRAC-based intraoperative dosimetry system has an undesirable mean absolute system error of 4 mm [21], due to mechanical pre-calibration errors and biases that may be present during seed reconstruction. Besides the FTRAC, other components of their system also prove to be insufficiently robust. Their seed segmentation algorithm [72] requires user intervention via a manually selected ROI, and their reconstruction algorithm known as MARSHAL [23] is not only sensitive to common pose errors, but is also incapable of handling "hidden" overlapping seeds.

In this chapter, we present an alternative system for PPB intraoperative dosimetry. Based on ultrasound and fluoroscopy, our system overcomes limitations of other image-guidance systems because it is inexpensive, easily implementable, and thoroughly tested. Since we use the ubiquitous mobile non-isocentric C-arm, it is also an improvement to existing ultrasound-fluoroscopy intraoperative dosimetry systems because it uses standard OR imaging equipment. Finally, by shifting the paradigm to a simple marker-based fiducial and implementing a robust pipeline of image processing algorithms, our system overcomes the problems that come with the latest proposed intraoperative dosimetry systems.

3.2 Methods

3.2.1 System Workflow and Apparatus

Our proposed intraoperative dosimetry system follows a simple premise (see Figure 18). Three or more distinct 2D fluoroscopic images are taken of the seeds and fiducial. TRUS images are taken to acquire the prostate volume. Both image sets are processed and registered to compute dose.

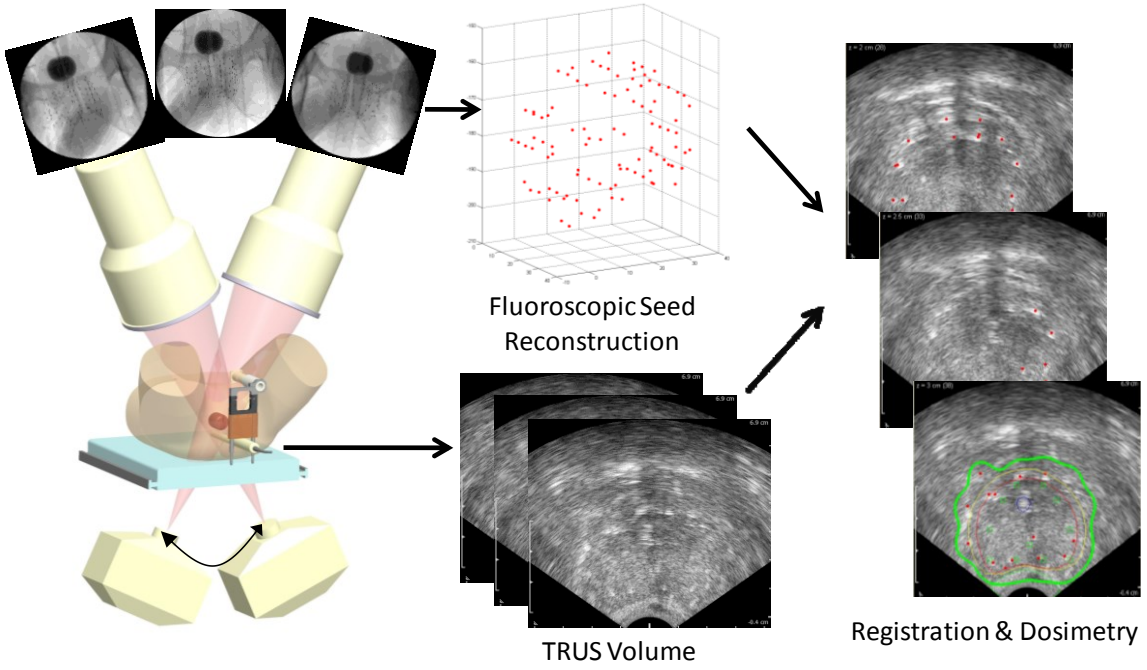

Figure 18 Ultrasound-Fluoroscopy Intraoperative Dosimetry System Workflow

Three pieces of hardware are required for our system. The first two are the imaging devices, i.e. the mobile non-isocentric C-arm and the TRUS scanner, both of which are assumed to be calibrated. The third is the fiducial, but instead of the FTRAC, our fiducial is a cylindrical radiolucent tube with nine seed-like point markers (see Figure 19). While fiducials based on large point markers, lines or conics may not be overlapped with the implanted seeds because it would degrade automatic seed segmentation, a fiducial with seed-like point markers may be overlapped because it would not interfere. This gives the technician the much needed freedom to maneuver the C-arm into the distinguishable poses required for reconstruction. Moreover, while other fiducials would entail a separate image processing pipeline, our fiducial allows the seed-like markers to be segmented and reconstructed just like implanted seeds. This streamlines the workflow and reduces the chances for error. The configuration of the nine markers is arbitrary; the only requirement in our experience is that at least four markers should be placed in a 3D configuration for more precise pose tracking. Such a liberty in configuration therefore also makes the fiducial trivial to

manufacture, especially when compared to other common tracking systems. This fiducial does not provide poses as precise as the FTRAC, but it is sufficiently precise for the purposes of our later-described seed reconstruction algorithm. And while the FTRAC is fixed in a predefined position, our fiducial may be moved to an arbitrary position using a flexible arm, since registration for our system is not done mechanically but computationally.

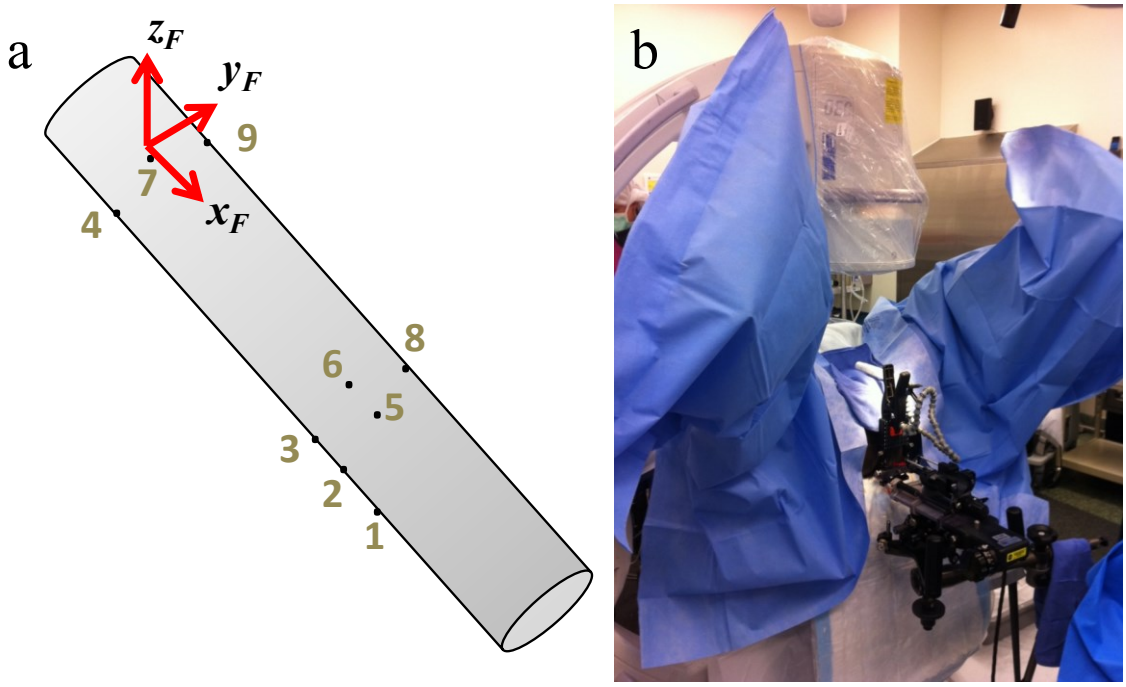

Figure 19 Simple marker-based fiducial. (a) Illustration of fiducial with markers and coordinate system identified. (b) Photograph of fiducial clipped to needle-guiding template with a flexible arm in the OR.

The protocol for our system begins with the patient placed on the surgical table and anesthetized in the lithotomic position. Prostate contouring and seed planning under TRUS guidance is completed during the intraoperative preplanning stage using the planning software known as VariSeed (Varian, Palo Alto, CA, USA). Palladium-103 seeds (Theragenics, Buford, GA, USA) are then delivered into the prostate via needles and a Mick applicator (Mick Radio-Nuclear Instruments, Mount Vernon, NY, USA). After all seeds are implanted, the TRUS volume for intraoperative dosimetry is acquired by recording transverse ultrasound slices at 1 mm intervals while the TRUS probe is continuously retracted from a few millimeters superior to the base to a few millimeters inferior to the apex. The fluoroscopy images for intraoperative

dosimetry are then acquired using a framegrabber by capturing at least 3 distinct images within a 20° cone around the patient's anterior-posterior axis with the TRUS probe fully retracted and the fiducial attached to the needle-guiding template. All images are then imported into our image-guidance software.

In software, there are four main image processing steps: 1) seed segmentation, 2) fiducial detection with pose estimation, 3) seed matching with reconstruction, and 4) fluoroscopy-to-TRUS registration. For each algorithm, graphical user interfaces (GUIs) have been set up for validation and for any required manual adjustments (see Appendix A).

3.2.2 Seed Segmentation

The first step in the image processing pipeline is seed segmentation, which has the purpose of localizing seeds in the multiple fluoroscopic images in preparation for seed matching with reconstruction. It therefore inputs a distortion-corrected image and outputs the 2D coordinates of every seed in the image (see Figure 20). Since our fiducial is composed of seed-like point markers, the marker coordinates are also outputted without differentiating markers from seeds; this distinction is left for the next step of fiducial detection with pose estimation. It is also designed to segment the seeds without a user-defined ROI, but if desired, an ROI may be selected via the provided GUI. Moreover, the algorithm attempts to recover overlapping seeds, but even if a few are not recovered by the end of this step, the remaining "hidden" seeds are generally recovered in our later step of seed matching.

Our algorithm is similar to the one presented in the previous chapter [31]. Briefly stated, the algorithm performs a morphological top-hat by reconstruction to improve contrast between the seeds and the background of the inputted image. The result is binarized by Otsu's threshold and each connected component region is then analyzed to distinguish any seeds that are closely overlapping. However, to improve upon the aforementioned published algorithm, next we assume that all regions may contain up to five overlapping seeds, although regions generally contain no more than three. We then perform k-means clustering on the coordinates in each region, setting the number of clusters to this maximum number of overlapping seeds. If the resulting cluster coordinates are unreasonable by being too close or too different in pixel intensity, we assume the wrong number of clusters was inputted into the k-means algorithm and reduce it by one. This is iterated until the result from the k-means clustering algorithm satisfies our

conditions of pixel distance and intensity. Note that at least one seed will be identified per region through this process.

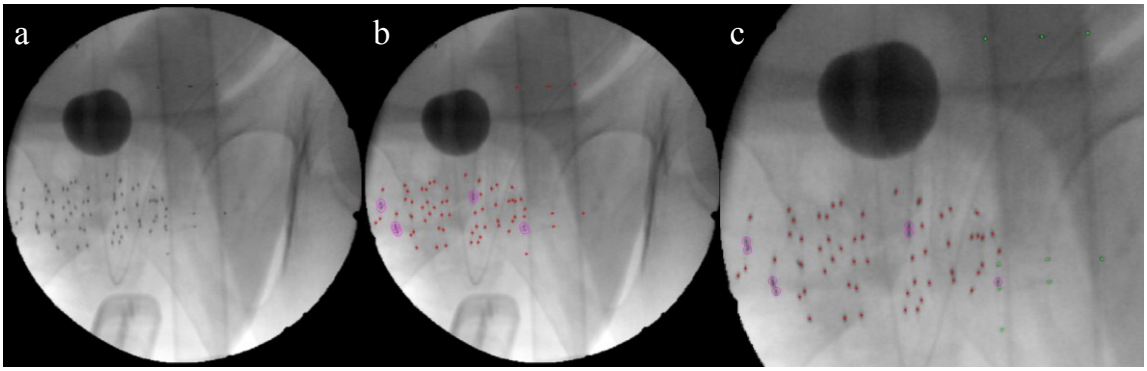

Figure 20 Seed segmentation and fiducial detection. (a) Before seed segmentation. (b) After seed segmentation and before fiducial detection, with single seeds (red dots) and overlapping seeds (magenta circles) identified. (c) After fiducial detection with markers identified (green dots).

3.2.3 Fiducial Detection with Pose Estimation

The second step is fiducial detection with pose estimation, which aims to distinguish the fiducial marker coordinates from among the segmented coordinates and calculate the respective pose from the marker coordinates for the later step of seed matching with reconstruction. This step therefore takes as input the segmented coordinates from the previous step and outputs the ones belonging to the fiducial as well as the corresponding pose (see Figure 20). We also assume the 3D model of the fiducial is known and there is some general knowledge of the pose (in our case, the length of the fiducial is oriented approximately foot-to-head and pose is roughly along the anterior-posterior axis), both of which are reasonable to know in a clinical setting. The fact that the fiducial model is one of the inputs also allows this algorithm to work for fiducials of arbitrary configuration.

Overall, this step is performed by iterating between two sub-functions we call template matching and pose estimation. Given a 3D pose, the template matching sub-function finds the best fit of the corresponding 2D fiducial projection among the segmented coordinates. Given 2D fiducial coordinates, the pose estimation sub-function calculates the optimal 3D pose. The algorithm is initialized with our assumed general knowledge of the pose. However, since this initial pose is not perfect, iteration between the two

sub-functions improves the results, with the outputs of each sub-function serving as the inputs to the other. This continues until convergence, which is generally within three iterations.

The details of the template matching sub-function are as follows (see Figure 21). First, the two furthest points are identified in the projected template (see Figure 21a). Next, these furthest points are registered in 2D with scale to a pair of segmented coordinates (see Figure 21b). Then, the registered template is overlaid on all the segmented coordinates to find the closest corresponding matches (see Figure 21c). Afterwards, an error metric is computed between the registered template and its closest matches; we chose mean Euclidean distance weighted by scale (see Figure 21d). In principle, this would be repeated over all pairs of segmented coordinates, and the registration with least error would be outputted as the best template match. However, to speed up computation time, we also added two heuristics that come from the assumption that the actual pose is within certain limits of the initial pose, thus reducing search time. The first heuristic is to consider only the pairs of segmented points that have a distance within a certain fraction of that of the furthest two points in the template, in our case 25%, since we assume that magnification will not differ significantly. The second heuristic is that the pairs of segmented coordinates must result in registrations within 15 degrees of in-plane rotation, since we do not expect to capture images with the fiducial oriented at a greater angle. With this approach, note that we would theoretically produce zero error if the fiducial is moved in 3D via four of the six degrees of freedom with respect to the initial pose. This is accomplished through the 2D registration with scale, which accounts for parallel movement (two translational degrees of freedom and one rotational degree of freedom, specifically yaw) and perpendicular movement (the third translational degree of freedom resulting in magnification) with respect to the imaging plane. We consequently notice that most errors in template matching are caused by the unaccounted differences about the other two rotational degrees of freedom (pitch and roll).

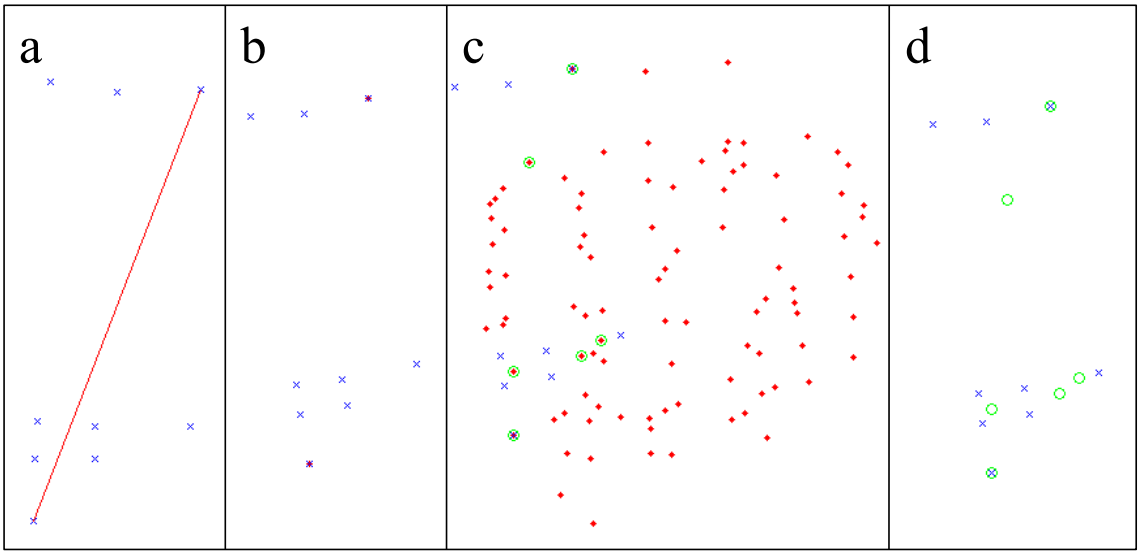

Figure 21 Steps in template matching. (a) Find the two furthest points in template (connected by red line) (b) register template (blue crosses) to a pair of segmented coordinates (red dots); (c) find the closest segmented coordinates (green circles) to the registered template, (d) calculate error, which in this case is high.

The other sub-function, pose estimation, is essentially an optimization problem with "projection error" as the cost function. To compute projection error, we consider that the image homogeneous coordinates, $p_i^I = [p_{ix}^I, p_{iy}^I, 1]$, of the i^{th} fiducial marker with world homogeneous coordinates, $p_i^W = [p_{ix}^W, p_{iy}^W, p_{iz}^W, 1]$, is calculated as:

$$p_i^I = \begin{bmatrix} f & 0 & u_0 & 0 \\ 0 & f & v_o & 0 \\ 0 & 0 & 0 & 1 \end{bmatrix} \begin{bmatrix} \boldsymbol{R}(\boldsymbol{\Phi}) & \boldsymbol{t} \\ \underline{0} & 1 \end{bmatrix} p_i^W$$

where f and (u_0, v_0) are the focal length and the image center, respectively, of the C-arm in units of pixels, assumed to be known through calibration, and $\boldsymbol{R}(\boldsymbol{\Phi})$ and $\boldsymbol{t}$ are the pose rotation in rotation matrix form and the pose translation vector, respectively. If the homogeneous segmented coordinates of the fiducial marker is notated as $\hat{p}_i^I = [\hat{p}_{ix}^I, \hat{p}_{iy}^I, 1]$, projection error is therefore computed as $PE_i = \|p_i^I - \hat{p}_i^I\|$. Therefore the optimization problem becomes:

$$\min_{\boldsymbol{\Phi}, \boldsymbol{t}} \sum_{i=1}^{N_M} PE_i$$

where N_M is the number of fiducial markers. This problem may be solved by various unconstrained optimization techniques, such as Newton's method.

3.2.4 Seed Matching with Reconstruction

The pipeline continues with the third step of seed matching with reconstruction, which computes a 3D seed cloud from the three or more distinct fluoroscopic images. This algorithm therefore takes as input the total number of implanted seeds and the previously computed results from all the images; it then outputs the 3D seed coordinates with respect to the fiducial coordinate system (see Figure 22). The algorithm we use is known as Automatic Pose Correction Reduced Dimensionality Matching Algorithm for Prostate Brachytherapy Seed Reconstruction (APC-REDMAPS) published by Lee et al. [38]. It is an extremely robust reconstruction algorithm that resolves hidden seeds while being insensitive to pose imprecision.

To describe it briefly, the crux of the reconstruction problem is to determine the unique correspondences of all the seeds among the images. However, since seeds may be hidden, this assignment problem should be modified so that each segmented coordinate may be assigned multiple times across images. In the case of the minimum of three images, it may be formulated as the following large combinatorial optimization problem:

$$\min_{x_{ijk}} \sum_{i=1}^{N_1}\sum_{j=1}^{N_2}\sum_{k=1}^{N_3} c_{ijk}(\boldsymbol{\Phi}, \boldsymbol{t})x_{ijk},$$

$$\text{s.t. } \sum_{j=1}^{N_2}\sum_{k=1}^{N_3} x_{ijk} \geq 1, \forall i$$

$$\sum_{i=1}^{N_1}\sum_{k=1}^{N_3} x_{ijk} \geq 1, \forall j$$

$$\sum_{i=1}^{N_1}\sum_{j=1}^{N_2} x_{ijk} \geq 1, \forall k$$

$$\sum_{i=1}^{N_1}\sum_{j=1}^{N_2}\sum_{k=1}^{N_3} x_{ijk} = N$$

$$x_{ijk} \in \{0,1\}, \forall i, j, k$$

where N is the total number of implanted seeds; N_1, N_2, N_3 are the numbers of segmented seed coordinates in images 1, 2, and 3, respectively; c_{ijk} is the cost of matching seed coordinates i, j, and k from images 1, 2, and 3, respectively and is a function of pose rotation $\boldsymbol{\Phi} = (\phi_1, \phi_2, \phi_3)$ and translation $\boldsymbol{t} = (t_1, t_2, t_3)$;

and x_{ijk} is a binary variable equal to 1 if seed coordinates i, j, and k from images 1, 2, and 3, respectively, are matched or 0 otherwise. In other words, the algorithm finds the matching that minimizes an overall cost such that the following constraints are satisfied: 1) every segmented coordinate in each image is matched at least once (hence ≥ 1), and 2) the total number of matches is equal to the total number of implanted seeds. The particular cost metric that is used is known as "reconstruction accuracy", which is defined as the root mean squared distance between the backprojected lines and their symbolic intersection. While it would normally be expensive to solve this huge optimization problem, the algorithm significantly reduces computation time by exploiting the nature of this cost metric to prune numerous impossible solutions, and by converting this NP-hard binary integer program into a polynomial-time linear program. Once this matching optimization problem is solved, reconstruction naturally follows by computing the intersection of the now matched backprojected lines.

At this stage, although the reconstruction is optimal for the poses provided, it might not be perfect since the poses themselves are not perfect; we therefore resolve these errors through automatic pose correction. The inspiration for this method comes from the fact that the 3D reconstructed seed cloud itself may serve as a model for recomputing the poses, as opposed to the inputted poses which were computed using only the fiducial markers. Automatic pose correction is therefore similar to the previous pose estimation sub-function, but the projection error is now minimized over the now reconstructed points, as we have correspondences of each 3D coordinate p_i^W to their respective 2D segmented coordinates $\hat{p}_{ij}^I$ in each jth image. The ensuing poses may then be reused for reconstruction, resulting in iterations between seed matching and automatic pose correction. This makes APC-REDMAPS less sensitive to imprecision in pose, which is critical for our less precise marker-based fiducial. We refer readers to Lee et al. [38] for more details.

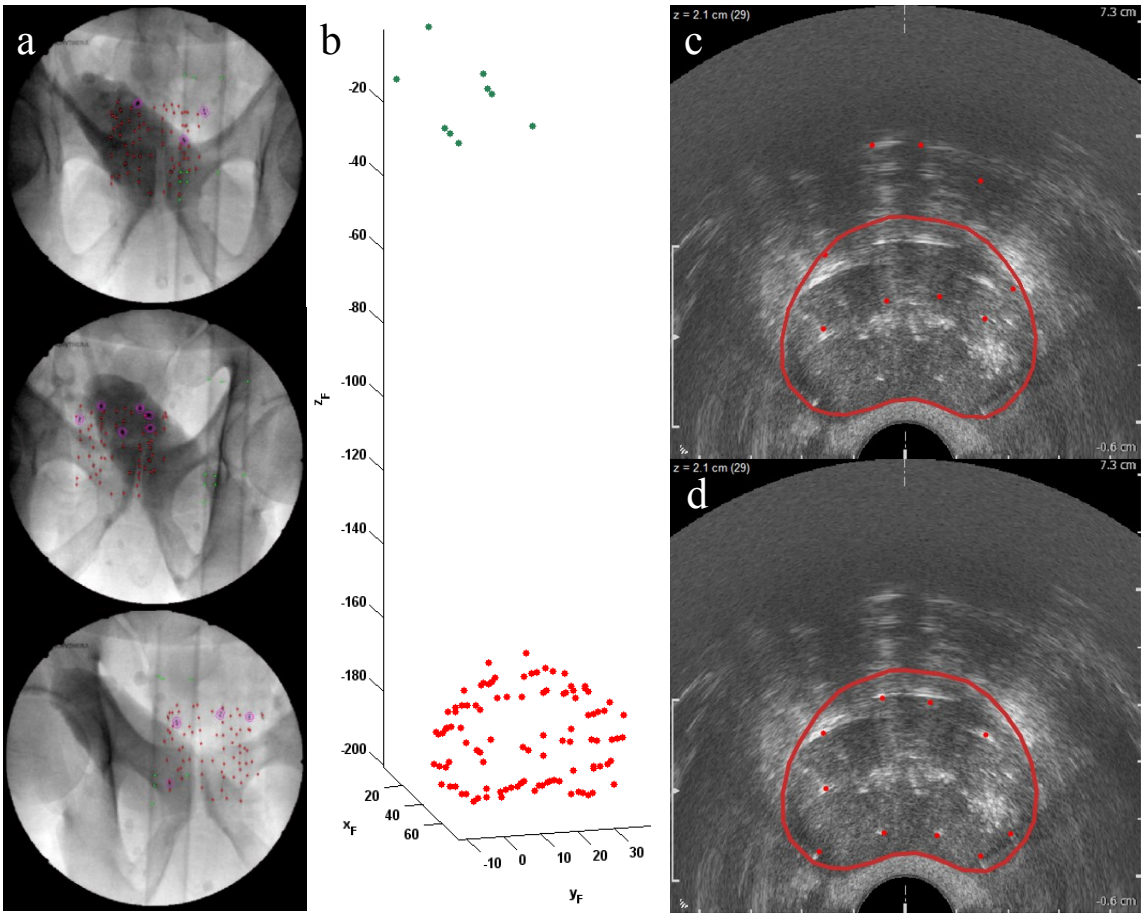

Figure 22 Reconstruction and registration. (a) Before reconstruction, user selects at least three fluoroscopic images that have seeds segmented and poses estimated. (b) After reconstruction, note that fiducial (green dots) is properly separated from implanted seed cloud (red dots). (c) Before registration, reconstruction (red dots) is centered on the ultrasound volume with the prostate contour (red outline) (d) After registration, note that the registered seeds are positioned on the hyper-echoic regions.

3.2.5 Fluoroscopy-to-TRUS Registration

The last step of the pipeline is fluoroscopy-to-TRUS registration. The idea is to take the now computed fluoroscopy 3D seed coordinates and position them properly in the TRUS volume for dosimetry. The algorithm thus inputs the 3D reconstructed seed coordinates and the acquired TRUS volume, and outputs a registered set of seed coordinates with respect to the TRUS coordinate system (see Figure 22). The prostate contour outlined during intraoperative preplanning should also be inputted, but if it is

unavailable, a volume of interest may be manually selected. The algorithm we use for this task is the one published by Dehghan et al. [8]. It is an image-based point-to-volume registration method that affinely registers the fluoroscopy seed points to the bright hyper-echoic regions of the TRUS volume.

To summarize it briefly, the algorithm completes the following steps. It begins by thresholding the TRUS volume to isolate the outlier hyper-echoic regions of the TRUS volume which are likely to be seeds. Next, a Gaussian blurring function is applied to provide an intensity gradient to guide optimization. Imposing realistic constraints on the parameters, the registration is then formulated as the following constrained optimization:

$$\max_{\boldsymbol{\Phi},\boldsymbol{t},\lambda} S(\boldsymbol{\Phi},\boldsymbol{t},\lambda),$$

$$\text{s.t. } \boldsymbol{\Phi}_{\min} < \boldsymbol{\Phi} < \boldsymbol{\Phi}_{\max}$$

$$\mathbf{t}_{\min} < \mathbf{t} < \mathbf{t}_{\max}$$

$$\lambda_{\min} < \lambda < \lambda_{\max}$$

where $\boldsymbol{\Phi} = (\phi_1, \phi_2, \phi_3)$ and $\boldsymbol{t} = (t_1, t_2, t_3)$ are the registration rotation and translation, respectively, and λ is a registration scaling factor in the anterior-posterior direction (hence, an affine registration) to account for TRUS probe pressure which is present in the TRUS volume but not in the fluoroscopy seed reconstruction. The cost metric, $S(\boldsymbol{\Phi},\boldsymbol{t},\lambda)$, is defined as the summation of image intensity over cuboids of size $\Delta x \times \Delta y \times \Delta z$ around each fluoroscopy reconstructed seed after registration, and is computed as:

$$S(\boldsymbol{\Phi},\boldsymbol{t},\lambda) = \sum_{i=1}^{N} \int_{-\frac{\Delta z}{2}}^{\frac{\Delta z}{2}} \int_{-\frac{\Delta y}{2}}^{\frac{\Delta y}{2}} \int_{-\frac{\Delta x}{2}}^{\frac{\Delta x}{2}} I_G\left(T(\boldsymbol{\Phi},\boldsymbol{t},\lambda;\boldsymbol{s}_i) + \begin{bmatrix} x \\ y \\ z \end{bmatrix}\right) dxdydz$$

where $I_G(x,y,z)$ is the Gaussian-blurred volume, $T(\boldsymbol{\Phi},\boldsymbol{t},\lambda;\boldsymbol{s}_i)$ is the affine registration, and $\boldsymbol{s}_i$ is the coordinates of seed i in the fluoroscopy coordinate system. The particular optimization used is a robust and efficient stochastic optimization method known as the Covariance Matrix Adaptation-Evolution Strategy (CMA-ES). The optimization is initialized by centering the reconstruction within the provided prostate contour or volume of interest. We refer readers to Dehghan et al. [8] for more details.

Putting it all together, we have an ultrasound-fluoroscopy intraoperative dosimetry system which localizes seeds already implanted into the prostate. A straightforward calculation based on seed activity information and these registered seed coordinates results in our final desired intraoperative dosimetry.

3.3 Results

The system has been evaluated on 37 patients under approval of the Institutional Review Board at the Johns Hopkins Hospital (Baltimore, MD, USA) using an OEC 9800 C-arm (GE Healthcare, Milwaukee, WI, USA) and Pro Focus ultrasound scanner (BK Medical, Peabody, MA, USA). While most of the TRUS volumes were acquired in slices at 1 mm intervals, there were 2 exceptions which had 2.5 mm intervals, which are identified in Table 7. For the first 24 patients, the TRUS images had pixel size of 0.1793×0.1793 mm^2, while those of the last 13 patients had pixel size of 0.1652×0.1652 mm^2. Although only 3 fluoroscopic images are required to run our system, a total of 6 images were acquired for research purposes. Each fluoroscopic image had a pixel size of 0.44×0.44 mm^2. The total time for TRUS and fluoroscopy image acquisition was approximately 2 minutes. For each patient case, the C-arm was calibrated to determine distortion and camera parameters (focal length and image center). Each step in the pipeline has been thoroughly tested.

The results for seed segmentation are found in Table 6. Out of all 37 patients, the overall false negative rate was 1% and false positive rate was 5%. False negatives are defined as actual seeds or markers that were in the field of view but were either completely missed in segmentation or resulted in an incorrect reconstruction due to failed separation of slightly overlapping seeds, while false positives are defined as segmented coordinates that are not actually seeds or markers. 10 of these patient cases, each identified in Table 6, had implants or otherwise radio-opaque objects in the field of view and therefore generated a significant number of false positives. If these 10 patients were excluded, the overall false positive rate would reduce to 2%.

After correcting any errors in seed segmentation, the results for fiducial detection with pose estimation are also found in Table 6. While overall fiducial detection rate is 98%, it is 100% for most patient cases.

Table 6 Seed Segmentation and Fiducial Detection Results

(Grayed patients had other radio-opaque objects in the field of view)

Patient	Actual Number of Seeds and Markers	Average Number of Segmented Coordinates	Average Number of False Negatives	Average Number of False Positives	Fiducial Detection Rates
1	112	108	1	1	100%
2	87	85	1	3	83%
3	70	70	0	3	100%
4	86	83	2	2	100%
5	84	88	2	8	100%
6	66	64	1	2	100%
7	87	81	1	1	96%
8	75	73	1	1	100%
9	110	103	5	2	100%
10	91	88	1	1	100%
11	102	97	1	1	100%
12	87	98	1	14	100%
13	121	116	1	2	100%
14	101	105	0	7	100%
15	119	129	1	16	100%
16	114	116	1	10	91%
17	98	114	1	21	100%
18	123	119	1	2	100%
19	101	103	1	6	100%
20	115	120	3	15	100%
21	83	90	1	14	96%
22	106	100	2	3	96%
23	106	103	0	1	100%
24	101	95	1	2	100%
25	89	86	1	1	96%
26	92	94	2	8	100%
27	110	108	0	4	100%
28	81	78	2	3	96%
29	113	113	1	7	93%
30	89	86	1	1	83%
31	107	102	1	3	100%
32	103	99	1	1	100%
33	102	103	1	4	100%
34	108	104	0	0	100%
35	104	100	1	3	100%
36	112	107	1	4	96%
37	97	97	1	4	100%
Overall Rate		99%	1%	5% (2%)	98%

The results for seed matching with reconstruction are found in Table 7. The 6 fluoroscopic images captured per patient were partitioned into 2 sets of 3 images each, thus forming 2 reconstructions per patient. There are no ground truth seed positions for these clinical cases, so instead we used reconstructions of 5 or all 6 images as our ground truth. This resulted in an overall mean reconstruction rate of 0.4 mm for our system, very close to the 0.5 mm mean reconstruction rate reported by Lee et al. [38]. It therefore shows that the marker-based fiducial does not alter the effectiveness of APC-REDMAPS.

Finally, the results for fluoroscopy-to-TRUS registration are also found in Table 7. Like reconstruction, there are no ground truth seed positions for these clinical cases, so instead we manually selected some seed-like hyper-echoic spots close to the registered seeds that we examined carefully to confirm they were true seeds. 10 seeds were manually segmented per patient in this way. This resulted in an overall mean registration error of 1.3 mm, with 0.4 mm, 0.5 mm, and 0.9 mm errors along the x, y, and z axes, respectively. This agrees closely to the overall mean registration error of 1.5 mm, with 0.5 mm, 0.5 mm, and 1.1 mm errors along the x, y, and z axes, respectively, reported by Dehghan et al. [8]. This therefore also shows that the marker-based fiducial does not alter the effectiveness of the registration algorithm.

Table 7 Reconstruction and Registration Results

(Grayed patients had 2.5 mm TRUS slice intervals while others has 1 mm)

Patient	Reconstruction Error (mm) Mean ± Std	Registration Error (mm) Mean ± Std			
	Overall	x	y	z	Overall
1	0.8±0.3	0.4±0.5	0.4±0.4	1.2±0.9	1.6±0.8
2	0.4±0.4	0.3±0.2	0.2±0.3	0.7±1.0	0.9±0.9
3	0.3±0.2	0.4±0.4	0.9±0.8	0.9±0.9	1.6±1.0
4	0.4±0.2	0.3±0.3	0.7±0.3	0.8±0.7	1.2±0.6
5	0.6±0.4	0.3±0.3	0.5±0.4	0.5±0.3	0.9±0.4
6	0.6±0.5	0.6±0.9	0.8±0.7	0.7±0.3	1.4±0.9
7	0.6±0.3	0.3±0.4	0.4±0.3	0.9±0.7	1.1±0.7
8	0.5±0.3	0.5±0.4	0.5±0.4	0.6±0.3	1.1±0.4
9	1.2±1.3	0.4±0.3	0.5±0.4	0.9±0.6	1.2±0.4
10	0.5±0.5	0.2±0.2	0.5±0.5	0.9±0.7	1.2±0.7
11	0.4±0.3	0.4±0.3	0.5±0.5	1.1±0.7	1.4±0.6
12	0.4±0.2	0.4±0.4	0.5±0.4	0.8±0.6	1.2±0.5
13	0.3±0.2	0.4±0.5	0.7±0.6	0.8±0.7	1.4±0.5
14	0.3±0.2	0.3±0.3	0.5±0.2	0.8±0.7	1.1±0.6
15	0.9±0.6	0.2±0.2	0.6±0.5	1.0±0.7	1.3±0.6
16	0.3±0.4	0.2±0.2	0.4±0.3	0.8±0.7	1.1±0.6
17	0.4±0.4	0.2±0.1	0.4±0.3	0.9±0.8	1.2±0.7
18	0.5±0.5	0.4±0.5	0.7±0.6	0.8±0.5	1.4±0.5
19	0.4±0.3	0.2±0.1	0.4±0.3	0.5±0.3	0.8±0.3
20	0.4±0.3	0.5±0.5	0.2±0.2	0.9±0.5	1.2±0.5
21	0.4±0.3	0.3±0.2	0.8±0.6	1.0±0.6	1.4±0.6
22	0.2±0.2	0.1±0.1	0.7±0.8	1.0±0.5	1.3±0.8
23	0.5±0.7	0.3±0.2	0.9±0.5	0.8±0.6	1.3±0.7
24	0.4±0.3	0.4±0.4	0.5±0.6	1.3±1.0	1.7±0.8
25	0.3±0.7	0.4±0.4	0.5±0.4	1.4±1.3	1.7±1.2
26	0.3±0.2	0.2±0.2	0.6±0.6	0.9±0.6	1.2±0.5
27	0.3±0.4	0.5±0.4	0.6±0.4	0.7±0.5	1.1±0.5
28	0.3±0.2	0.1±0.0	0.4±0.3	0.9±0.6	1.0±0.6
29	0.5±0.4	0.4±0.4	0.5±0.6	0.9±0.8	1.2±0.9
30	0.3±0.2	0.5±0.3	0.6±0.6	1.0±0.7	1.4±0.6
31	0.5±0.3	0.3±0.4	0.4±0.4	1.0±1.1	1.3±1.0
32	0.3±0.2	0.5±0.6	0.4±0.3	0.8±0.7	1.2±0.7
33	0.2±0.2	0.6±0.6	0.6±0.4	1.2±0.7	1.7±0.7
34	0.2±0.2	0.4±0.4	0.4±0.4	0.5±0.3	0.9±0.3
35	0.3±0.2	0.3±0.2	0.4±0.4	1.0±0.7	1.3±0.6
36	0.3±0.2	0.3±0.3	0.4±0.3	0.5±0.6	0.9±0.5
37	0.2±0.2	0.6±0.3	0.7±0.6	0.8±0.6	1.4±0.5
Overall	0.4±0.5	0.4±0.4	0.5±0.5	0.9±0.7	1.3±0.7

3.4 Discussion

As mentioned previously, there are 10 cases when our revised seed segmentation algorithm performs poorly due to radio-opaque implants or objects in the field of view. In these cases, it is necessary to rerun the segmentation on a user-selected ROI and manually correct the segmentation result. However, it is interesting to note that if we manually segment these undesired radio-opaque objects, we may use our system in an unconventional way to determine the location of these objects. Figure 23 shows an example where a cloth with embedded radio-opaque loops was accidentally placed in the fluoroscopy field of view. Reconstruction confirms that the loops were located far from the implanted seed cloud, indicating that they were indeed not part of an object implanted in the patient but actually within the cloth lying on the patient's abdomen. Although not part of the original intent of our system, this suggests that our system may be applied to localize other objects besides brachytherapy seeds in applications beyond the scope of PPB.

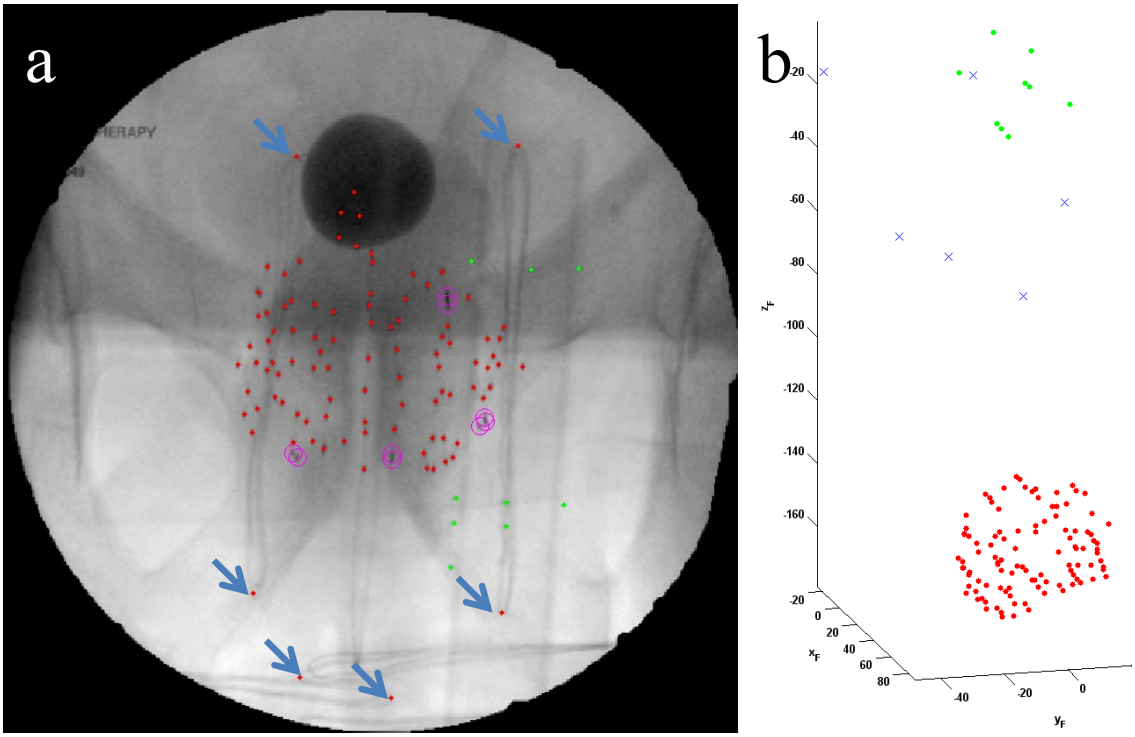

Figure 23 Reconstruction of extraneous objects. (a) Fluoroscopic image with ends of radio-opaque loops segmented (blue arrows). (b) Reconstruction showing loops (blue crosses) between seeds (red dots) and fiducial (green dots).

While our new fiducial detection algorithm detects the fiducial perfectly most of the time, in the instances when it is imperfect, the algorithm at least detects some of the markers in all our patient cases. The most common partial detection occurs when the lower portion of the fiducial overlaps with the seed cloud, resulting in the misdetection of 2 fiducial markers (see Figure 24). This suggests that a fiducial configuration with the markers more separated may result in higher detection rates, although the current configuration is sufficient for our purposes.

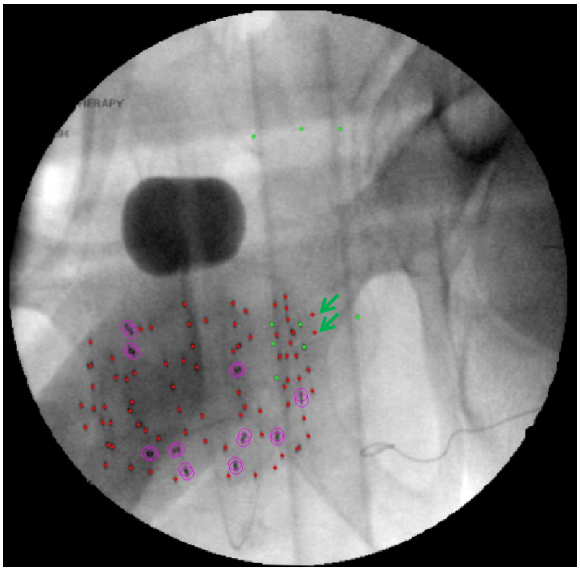

Figure 24 Misdetection of two fiducial markers (green arrows).

Finally, the system as a whole also has the capability of detecting cold spots as shown in Figure 25. This highlights the utility of the system, as cold spots may then be addressed immediately in the OR rather than requiring the patient to return for additional therapy after being discharged.

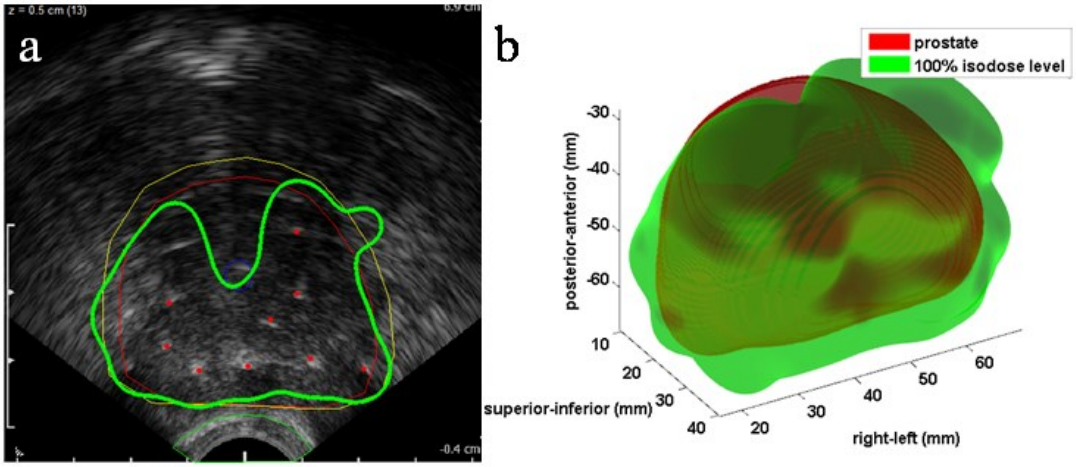

Figure 25 Intraoperative dosimetry result showing cold spot. (a) TRUS image is overlaid with the 100% isodose level (thick green line) computed from the registered seed reconstruction (red dots). Contours are also displayed as thin lines (red for prostate, blue for urethra, green for rectum, and yellow for planning target volume). (b) 3D rendering of the same prostate and 100% isodose level; cold spot is evident at the anterior-superior end of the prostate.

3.5 Conclusion

In this chapter, we presented an image-guidance system for PPB intraoperative dosimetry. With the help of a marker-based fiducial and four robust image processing algorithms, dose is accurately and quickly computed with unprecedented convenience. While there are other alternative dosimetry systems in development, our system may be readily adopted in clinics worldwide, being inexpensive, easily implementable, and simple to use. The system therefore ultimately leads to saved time and money while improving the surgical outcome for prostate cancer patients.

Chapter 4. Photoacoustic Imaging of Seeds Using a Clinical Ultrasound System

Seed localization systems based on TRUS and fluoroscopy are rather mature and may be adopted into clinics worldwide in the near future. Still, there are reasons to pursue better ways to localize seeds that avoid giving extra radiation to the patient and may be operated in real-time. The primary contribution of this work, previously presented at SPIE Medical Imaging [33] and published in the Journal of Biomedical Optics [34], is a prototype photoacoustic imaging system based on a clinical ultrasound scanner to detect seeds in gelatin phantoms and in an *ex vivo* dog prostate. Photoacoustic imaging is a modality that has only been recently applied to PPB. It is also challenging to put such a system together because its sensitive components must be integrated appropriately. Nonetheless, results of this system in preclinical phantom experiments demonstrate that seeds indeed may be imaged with high contrast, even with changes in various parameters, and shows promise of viability as the system is continually improved.

4.1 Introduction

Researchers have long been investigating imaging systems that would resolve the issue of intraoperatively visualizing and localizing seeds in relation to the prostate. These systems include TRUS-fluoroscopy [14, 63, 56], cone-beam CT [75], MRI [6], and more, each of which has its strengths and weaknesses for PPB. Nonetheless, photoacoustic imaging has recently emerged as a promising imaging modality for various biomedical applications [76], and may be particularly fitting for PPB. This technology is centered on a physical phenomenon known as the photoacoustic effect, in which electromagnetic energy, such as pulsed light from a laser source, is absorbed by a target material, converted into acoustic energy through rapid thermoelastic expansion, and may consequently be detected with ultrasound transducers. Photoacoustic imaging would be effective in localizing seeds due to the strong contrast it generates between seeds and tissue at certain wavelengths of light. It would also be practical for PPB since it takes advantage of already-existing ultrasound equipment in the OR, thus reducing any additional burden on the

surgeon. Photoacoustic imaging could also be cost-effective, since it would not require any large imaging equipment such as a CT or MRI scanner, but only the addition of a laser.

There are other groups who have worked on photoacoustic imaging of metal needles [59], brachytherapy seeds in chicken tissue [19], and iodine seeds in bovine prostate tissue [60]. However, we provide an alternative photoacoustic imaging system [2, 33], validating it by imaging palladium seeds in the prostate tissue of a dog, which is a common animal model for the human prostate. Although this research area is still in its infancy, we present initial results to demonstrate the possibility of applying photoacoustic imaging to PPB.

4.2 Materials and Methods

4.2.1 Photoacoustic imaging system hardware

The hardware for our photoacoustic imaging system consisted of three parts: 1) the laser, 2) the ultrasound system, and 3) the data acquisition device (see Figure 26).

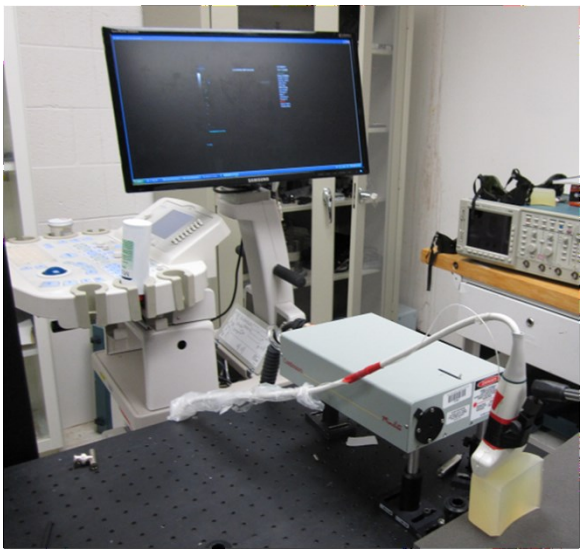

Figure 26 Figure of photoacoustic imaging system setup. System was composed of laser (bottom right), ultrasound system (top left), and data acquisition device (not in view).

A neodymium-doped yttrium aluminum garnet (Nd:YAG) laser called the Minilite II (Continuum, Santa Clara, CA, USA) was used for the laser component of our system. Its pulse repetition rate could be

varied from 1 to 15 Hz, and the energy of the laser could also be adjusted from 0 to 50 mJ/pulse. The laser spot size could be altered by optics, but for our purposes, it was kept at the default beam diameter of 3 mm ($1/e^2$ full width). The wavelength was centered at 1064 nm, which provided good contrast between the metallic seeds that strongly absorb such light and the soft tissue of the prostate that does not [60]. As far as human safety is concerned, the maximum permissible exposure (MPE) at this wavelength is 100 mJ/cm^2. Finally, the pulse duration was approximately 5 ns, which well satisfied the thermal and stress confinement conditions for generating the photoacoustic effect efficiently.

The ultrasound system in this setup was the SonixRP (Ultrasonix, Richmond, BC, Canada). It is a diagnostic ultrasound system packaged with an Ultrasound Research Interface that allowed some features for research purposes that are not available on a purely clinical system. We equipped this system with a standard 128-element 60 mm linear array transducer (model L14-5W). Note that all our ultrasound equipment was commercialized and approved for clinical use. This made our setup rather distinct, since most other photoacoustic groups used customized ultrasound transducers rather than equipment that is already clinically approved [76].

The final hardware was the data acquisition device, which was necessary to acquire photoacoustic images in real-time. Although photoacoustic and ultrasonic data may both be acquired by ultrasound transducers, their acquisition processes are fundamentally different. In ultrasound, most images are acquired using focused beams transmitted along lines. After transmission, the signals received by the transducer elements are then combined in such a way as to tune to the area excited by the focused ultrasound beam (a process known as beamforming) to form a single line of data. The process repeats until all lines (generally, 128 lines, or however many elements there are in the transducer) are acquired to form one frame. On the other hand, in photoacoustic imaging, rather than exciting a single line, a single laser pulse may excite the whole field of view, implying that acquisition should be done frame-by-frame rather than line-by-line. Moreover, we are no longer interested in the post-beamformed data of a single line but the raw pre-beamformed data of the entire frame, which may then be reconstructed as we choose. Unfortunately, clinical ultrasound systems generally do not provide access to this level of data due to the lack of current clinical interest and the vast size of pre-beamformed data that is generally collected.

However, Ultrasonix (Richmond, BC, Canada) had recently made available the SonixDAQ, a data acquisition device that allowed the acquisition of raw pre-beamformed data in parallel to standard imaging. Our group initialized the development of this SonixDAQ module specifically for this application in collaboration with the University of Hong Kong and Ultrasonix. It supports 128 elements with 12-bit sampling along with external triggering for synchronous data acquisition. In addition, the SonixDAQ has 16 GB internal memory, a 40 MHz internal clock, and a USB port for transferring data.

All the hardware also needed to be synchronized to ensure proper imaging. To accomplish this task, we used the SonixRP to trigger the SonixDAQ, as the SonixDAQ was so designed to work with Ultrasonix ultrasound systems. We also used the same SonixRP signal to trigger the Minilite II. However, the unmodified signal from the SonixRP was incompatible with the Minilite II, so we built a monostable multivibrator circuit to transform the SonixRP impulse train trigger signal into the proper Minilite II transistor-transistor logic signal. Even so, there was a delay of approximately 150 μs between the trigger signal and the actual firing of the laser because of the Q-switched nature of the Minilite II. We accounted for this by adding in software the same delay after the trigger signal before acquiring data with the SonixDAQ.

4.2.2 Real-time photoacoustic imaging software

Some software was also needed to acquire and reconstruct photoacoustic images in real-time. While the SonixDAQ provided us the functionality of acquiring pre-beamformed data, it only allows the user to download the data off the device after acquisition and does not provide real-time streaming of the data. To circumvent this limitation, we developed a software module we called the MUSiiC-DAQ-Server [27] which we incorporated into our larger software architecture known as MUSiiCToolkit [57]. The MUSiiC-DAQ-Server was therefore a module that streamed packets of data from the SonixDAQ and was created based on the Software Development Kit (SDK) provided by Ultrasonix. The data was then communicated via the network using an extended version of OpenIGTLink [67], which we called OpenIGTLinkMUSiiC [26]. The pre-beamformed data was finally loaded into MATLAB by Mathworks (Natick, MA, USA) using the OpenIGTLink/MATLAB interface.

Once the data was loaded into MATLAB, we had several beamforming and reconstruction algorithms available to generate photoacoustic images. While we implemented the standard delay-and-sum beamforming algorithm, we also utilized the one-step image reconstruction function for linear measurement surfaces provided in the photoacoustic simulation MATLAB toolbox known as k-Wave [68]. This reconstruction algorithm is based on the exact frequency-domain reconstruction formula provided by Xu et al. for thermoacoustic tomography [77], therefore generating in theory more accurate photoacoustic images than delay-and-sum. The resulting reconstruction was then envelope-detected and the dynamic range compressed by a square root function to produce our final photoacoustic image.

4.2.3 Phantom experiments

We performed several phantom experiments to analyze how our photoacoustic imaging system responded to various situations as applicable in PPB, such as variations in laser parameters and variations in phantom set up. The seeds we used were decayed Palladium-103 seeds from Theragenics Corporation (Buford, GA, USA) encapsulated in titanium cylindrical shells 0.8 mm in diameter and 4.5 mm long implanted into gelatin from porcine skin. Due to the limited power of our laser, we imaged a single or, at most, a few seeds in these experiments. These numbers were not nearly sufficient for thorough validation, since dozens of seeds are typically implanted in an actual brachytherapy operation. However, the purpose of these experiments was not to thoroughly validate this photoacoustic imaging system but to provide an initial understanding of its basic capability and feasibility. A more thorough validation may then be provided given a more powerful laser.

The first two experiments involved imaging a single seed while varying laser parameters, which were the pulse repetition rate and the laser energy. The first experiment therefore involved acquiring a series of images by varying pulse repetition rate from 1 to 15 Hz with a step size of 1 Hz, keeping all other parameters constant. The second experiment involved varying the energy from 50 to 0 mJ/pulse with a step size of 10 mJ/pulse, likewise keeping all other parameters constant. Except for the particular parameter that was being studied, the standard settings for these parameters were: 1) a repetition rate of 10 Hz, 2) an energy of 10 mJ/pulse, 3) the seed implanted 1 cm deep with respect to the laser source, 4) the seed

implanted 2 cm deep with respect to the linear transducer probe, and 5) the probe oriented perpendicular to the seed (see Figure 27).

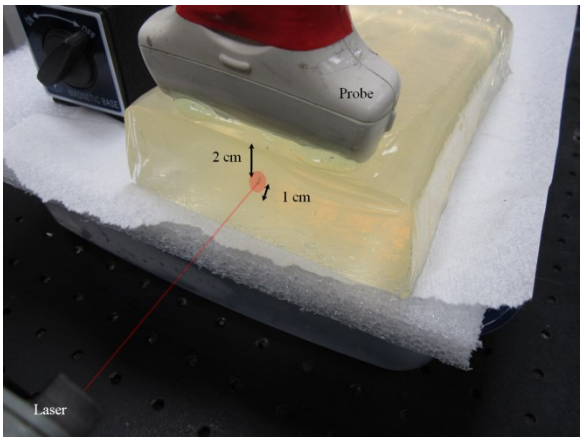

Figure 27 Photograph of baseline setup. Note that laser was directed independently of transducer probe.

We also varied several parameters involving the phantom (see Figure 28). Thus, the third experiment involved varying the depth of the seed implanted into the gelatin with respect to the laser, varying from 0 to 10 cm with a step size of 1 cm. This was done by starting with a large 10 cm slab of gelatin and gradually cutting away the gelatin down to 0 cm. In the fourth experiment, we varied the depth from the probe from 0 to 5 cm with a step size of 0.5 cm, again starting with a larger slab and cutting down to 0 cm. Finally, we also changed the orientation of the probe with respect to the seed, starting at 0 degrees and ending at 90 degrees with a step size of 15 degrees. Like the laser parameters, we kept all other parameters at the standard settings indicated earlier with a few exceptions. The first exception was for the third experiment, that in addition to the standard data for the energy of 10 mJ/pulse, we also acquired data for the maximum energy of 50 mJ/pulse to see the effect of varying the depth of the seed with respect to the laser more clearly. The second exception was for the last experiment in that the seed was implanted 4 cm deep with respect to the laser, rather than the usual 1cm deep, to make room for a full 90 degree probe rotation.

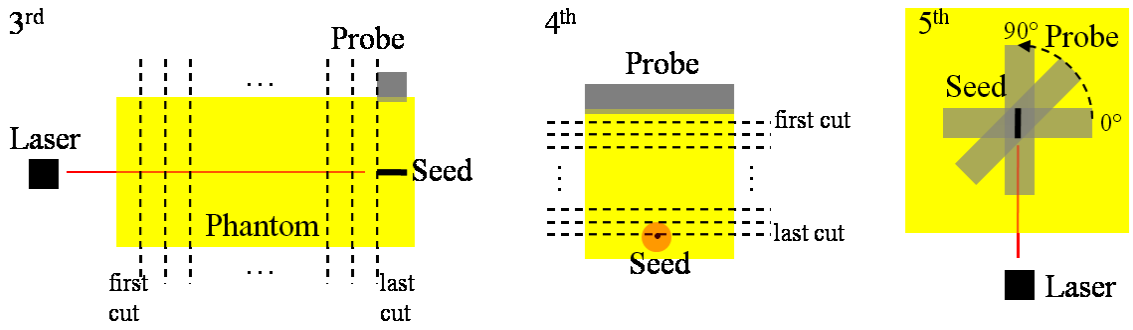

Figure 28 Illustration of phantom parameter experiments. The left figure illustrates a side view of how the third experiment was conducted involving the parameter of the depth of the seed with respect to the laser. The center figure illustrates a front view of how the fourth experiment was conducted involving the parameter of the depth of the seed with respect to the probe. The right figure illustrates a top view of how the fifth experiment was conducted involving the parameter of the orientation of the probe with respect to the seed.

Finally, we also imaged a phantom consisting of an *ex vivo* dog prostate implanted with four seeds and again embedded in gelatin from porcine skin. This particular experiment was taken at a repetition rate of 10 Hz and at an intensity of 40 mJ/cm^2 using different but similar components to the previously described setup. Here we used the Surelite II, a larger more powerful sibling to the Minilite II, and the SonixCEP, a close kin to the SonixRP.

4.3 Results and Discussion

The results for the first experiment with varying pulse repetition rate are shown in Figure 29. Note that the signal-to-noise ratio (SNR) after reconstruction reduces slightly with increasing pulse repetition rate. On the other hand, theory suggests that the strength of the photoacoustic effect is independent of the pulse repetition rate and should therefore be constant. The slight reduction in signal may be due to the fact that the photoacoustic effect is inherently a vibration which moves the light-weight seed and phantom. Such movements, although miniscule, may cause slight misalignment of the seed within our especially small Gaussian-profiled laser spot. Less intense signals therefore resulted from the suboptimal laser energy flux reaching the seed, and would have accumulated as the experiments were conducted from 1 to 15 Hz. Although the slight reduction is apparent here, we would expect to have a more uniform and larger laser flux in a clinical setting, and could therefore expect that repetition rate would have little effect when

applying photoacoustic imaging to PPB. SNR here has been calculated as the difference of the maximum and minimum of the reconstructed data divided by the root mean squared of a constant ROI representative of noise. Each data point was averaged over 8 frames, and error bars in the figure represent standard deviation around this mean data point.

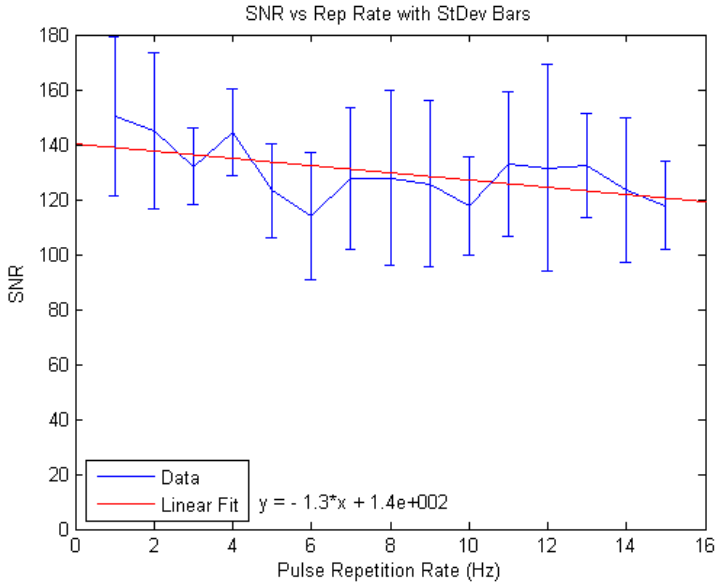

Figure 29 Results of the first experiment showing signal-to-noise ratio with respect to repetition rate.

Likewise, the results for the second experiment with varying pulse energy are shown in Figure 30. Note that SNR here is roughly linear, or perhaps slightly exponential, with respect to laser pulse energy. This generally agrees with the theoretical equation [68]:

$$p_0 = \Gamma \mu_a \Phi$$

where p_0 is the initial pressure distribution caused by the photoacoustic effect, Γ is the Grüneisen parameter, which is a constant that relates absorbed light with the initial pressure, μ_a is the optical absorption coefficient, and Φ is the light fluence. Thus in theory, as laser energy increases, the light fluence, Φ, increases proportionally while the Grüneisen parameter, Γ, and the absorption coefficient, μ_a, remain constant, causing a linear increase in the signal due to the linear increase in initial pressure distribution, p_0. However, the slightly exponential nature of the curve may again be due to miniscule seed movement within the sensitive alignment of the laser spot. Since the experiments were conducted starting from 50 mJ/pulse and ending at 0 mJ/pulse, the higher energy samples would have slightly more signal

than expected compared to the lower energy samples. Nonetheless, assuming a larger and more uniform laser spot, we expect a linear increase in signal with increasing pulse energy in a clinical experiment.

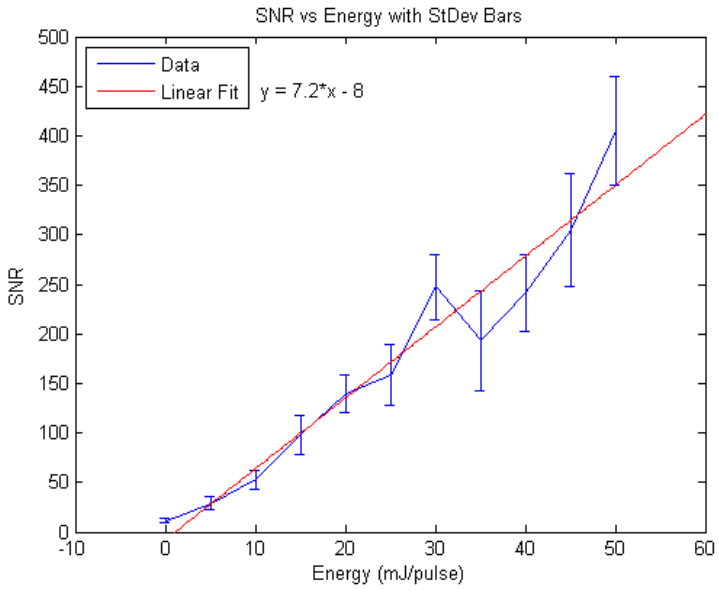

Figure 30 Results of the second experiment showing signal-to-noise ratio with respect to energy.

The results for the third experiment with varying seed depth from the laser are shown in Figure 31. Except for the first few centimeters, a roughly exponential decay in SNR is seen for both the 10 mJ/pulse case and the 50 mJ/pulse case. This agrees with the theory of Beer's Law that is applicable to photoacoustic imaging which states:

$$I(z) = I_0 e^{-\mu_a z}$$

where $I(z)$ is the light intensity as a function of the depth z, I_0 is the initial intensity, and μ_a is the optical absorption coefficient of the medium. However, note that the first few centimeters of depth (0 to 2 cm) do not correspond at all with exponential decay. This may be due to inevitable inconsistencies in laser spot alignment mainly caused from cutting the gelatin phantom, which becomes much more difficult to do at smaller depths than larger ones. Inconsistent alignment would therefore cause the inconsistencies seen in the first few centimeters of our plot. However, it may be concluded that sufficient signal can be generated up to 5 cm (roughly the length from base to apex of a human prostate) using 10 mJ/pulse and up to 9 cm using the max energy of 50 mJ/pulse.

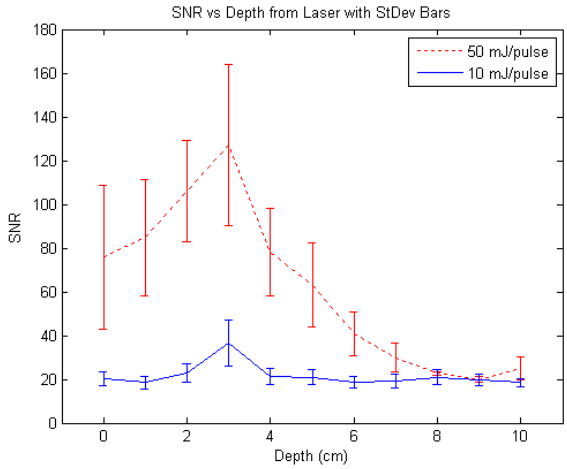

Figure 31 Results of the third experiment showing signal-to-noise ratio with respect to depth of seed from laser.

Figure 32 shows photoacoustic images from our fourth experiment with varying seed depth from the probe. In this experiment, SNR does not play as significant of a role, since signal related to depth may easily be accounted for using the time-gain control of the ultrasound system. However, note the shape of the seed in these photoacoustic images remains relatively the same. This again agrees with theory as the acoustic waves generated by the photoacoustic effect should reconstruct to the same shape regardless of its location with respect to the probe. An ultrasound echo may also be seen below the actual location of the seed due to its closeness to the edge of the phantom (about 1 cm away). Echoes may be expected since the impedance mismatch at the edge of the phantom causes the ultrasound waves generated by the photoacoustic effect to reflect and eventually be detected by the probe. Such echoes may also occur in a patient setting, particularly at tissue-air and tissue-bone interfaces, but such interfaces are generally far from the imaging area of the seeds and are not expected to be an issue. Reflections from tissue-seed interfaces are more concerning, but it is yet to be seen if such small interfaces would cause a significant problem. In addition, streaking artifacts are somewhat noticeable in the image, but this is due to the reconstruction algorithm being applied on data acquired with a probe of finite length, whereas a complete and clean reconstructed image would require a probe of infinite length.

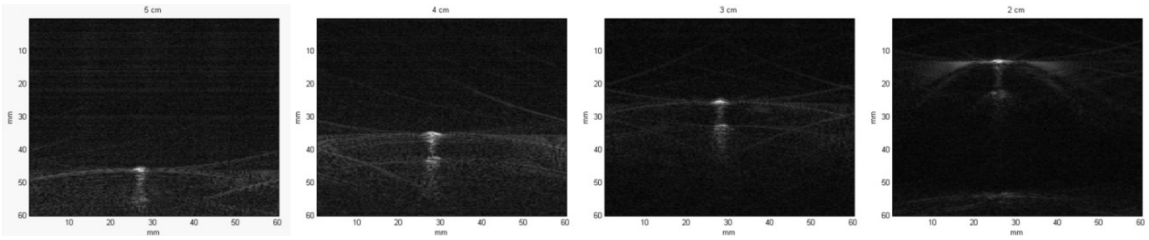

Figure 32 Results of the fourth experiment showing images for 5 cm (far left), 4 cm (middle left), 3 cm (middle right), and 2 cm (far right) depths of the seed from the ultrasound probe.

Figure 33 then shows photoacoustic images from our fifth experiment with varying seed orientation with respect to the probe. Note that the orientation of the seed is clearly seen in the reconstructed photoacoustic images, growing from a small axial cross-section in the 0° orientation to a long longitudinal cross-section in the 90° orientation of the cylindrical seed. As the orientations of the many seeds implanted in the prostate may differ in an actual brachytherapy procedure, this capability to visualize orientation differences may prove useful.

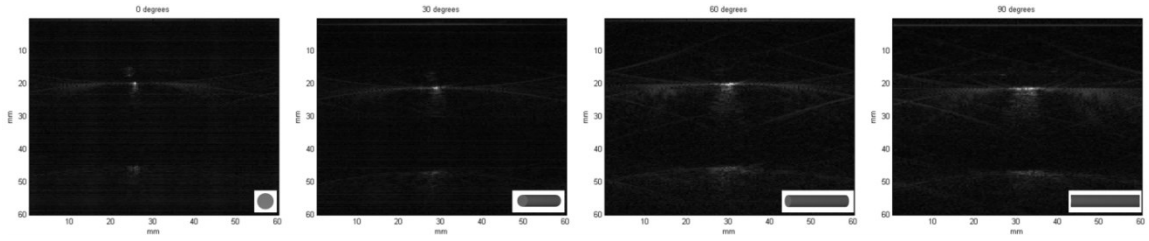

Figure 33 Results of the fifth experiment showing images for 0 degrees (far left), 30 degrees (middle left), 60 degrees (middle right), and 90 degrees (far right) of the probe oriented with respect to the seed.

Finally, Figure 34 shows the results of our final *ex vivo* dog prostate phantom experiment. Although four seeds were implanted in the prostate, only two seeds may be seen in this plane of view. Using standard delay-and-sum reconstruction, only one seed is visible. However, we may also take advantage of the linear geometry of the probe to apply to the same raw data the exact reconstruction formula provided in the k-Wave toolbox. The two seeds are consequently more visibly distinguishable.

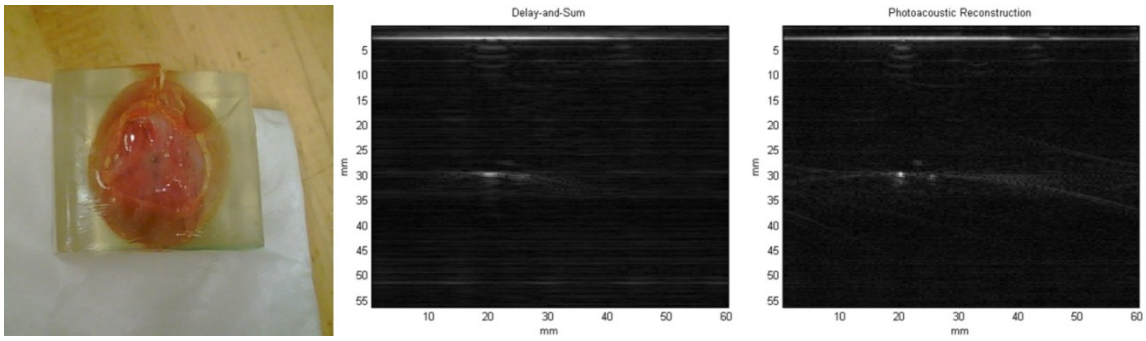

Figure 34 Results from *ex vivo* phantom, including photograph (left), delay-and-sum image (middle), and exact photoacoustic reconstruction image (right).

4.4 Conclusion

In this chapter, we presented a photoacoustic imaging system that is capable of imaging prostate brachytherapy seeds. We studied the capabilities of our system by varying laser and phantom parameters. Finally, we also showed the results on an *ex vivo* dog prostate phantom to show the potential of applying this system to a clinical PPB procedure.

However, it is obvious that there is much more to be done before this system can become a viable clinical system. For one, we need a more powerful laser system to enable the imaging of larger volumes and multiple seeds. Imaging of many seeds may be a potential issue in photoacoustic imaging as it is in ultrasound, since seeds closer to the transducer may obstruct the acoustic waves from seeds that are farther away. However, photoacoustic imaging has a distinct advantage over ultrasound since it captures more acoustic data using the full transducer aperture compared to the windowed aperture used in ultrasound, so image quality is not anticipated to suffer so significantly. Testing also needs to be done with a transrectal probe to ensure proper translation into the OR. Most probes used in brachytherapy have two transducers, one for transverse imaging and the other for longitudinal imaging. Functionality and scan conversion for both modes of operation should be made available for a complete photoacoustic imaging system. Light delivery of the laser to the prostate is also an issue that needs to be considered. While external radiation via the perineum would theoretically penetrate sufficiently deep to image the prostate, it would be advantageous to incorporate optical fibers to ease light delivery. However, considering the laser intensity required to image the entire prostate, it would be challenging to develop a fiber setup to channel the laser

power that is required. Finally, *in vivo* clinical studies should incorporate all these factors to eventually deliver a fully capable system into the OR.

Chapter 5. *In vivo* Photoacoustic Imaging of Prostate Brachytherapy Seeds

The photoacoustic imaging system presented in the previous chapter was sufficient for imaging seeds *ex vivo* in the laboratory, but was still far from the ideal system which would image seeds *in vivo* in the OR. The greatest challenge to this transition is obtaining sufficient photoacoustic signal with the laser energy now channeled to the *in vivo* prostate via fiber optics. The primary contribution of this work, previously presented in the Ultrasound Imaging and Tissue Characterization Symposium [35], is therefore the ability to visualize multiple seeds *in vivo* in the OR with photoacoustic imaging. Results of an *in vivo* dog experiment show that this next generation photoacoustic system is capable of visualizing multiple seeds at safe energies.

5.1 Introduction

As mentioned previously, photoacoustic imaging is a promising method combining the techniques of optical imaging and ultrasound for solving the seed localization problem of ITP. While ultrasound alone generates numerous false positives and negatives as seeds are implanted, photoacoustic imaging produces the wavelength-specific contrast required to visualize the seeds. Moreover, the transrectal probe used in contemporary PPB practice may be utilized both for ultrasound and photoacoustic imaging, therefore requiring minimal effort in the registration of the prostate and the seeds, while also being practical for brachytherapists to eventually adopt.

While we presented a prototype photoacoustic system in the previous chapter [34], several key components were missing which prevented it from being clinically usable. Additional hardware components were needed such as a more powerful laser system and a clinical transrectal probe. Laser energy delivery issues also needed to be addressed to make the system viable in a clinical setting. While other research groups have also presented their prototype photoacoustic systems for PPB [59, 60, 19, 48], none of them have successfully applied their systems in an *in vivo* setting.

In this chapter, we therefore present our next generation photoacoustic system for PPB intraoperative dosimetry. Our system overcomes the limitations of alternative intraoperative dosimetry systems because it is effective, easily implementable, and safe. It is also an improvement to existing photoacoustic systems because it clearly images multiple seeds in the OR.

5.2 Materials and Methods

5.2.1 Photoacoustic imaging system

Our photoacoustic system is basically composed of a the laser system and the ultrasound scanner. Our system also consists of several additional components to acquire photoacoustic data and make it more clinically usable in the operating room (see Figure 35).

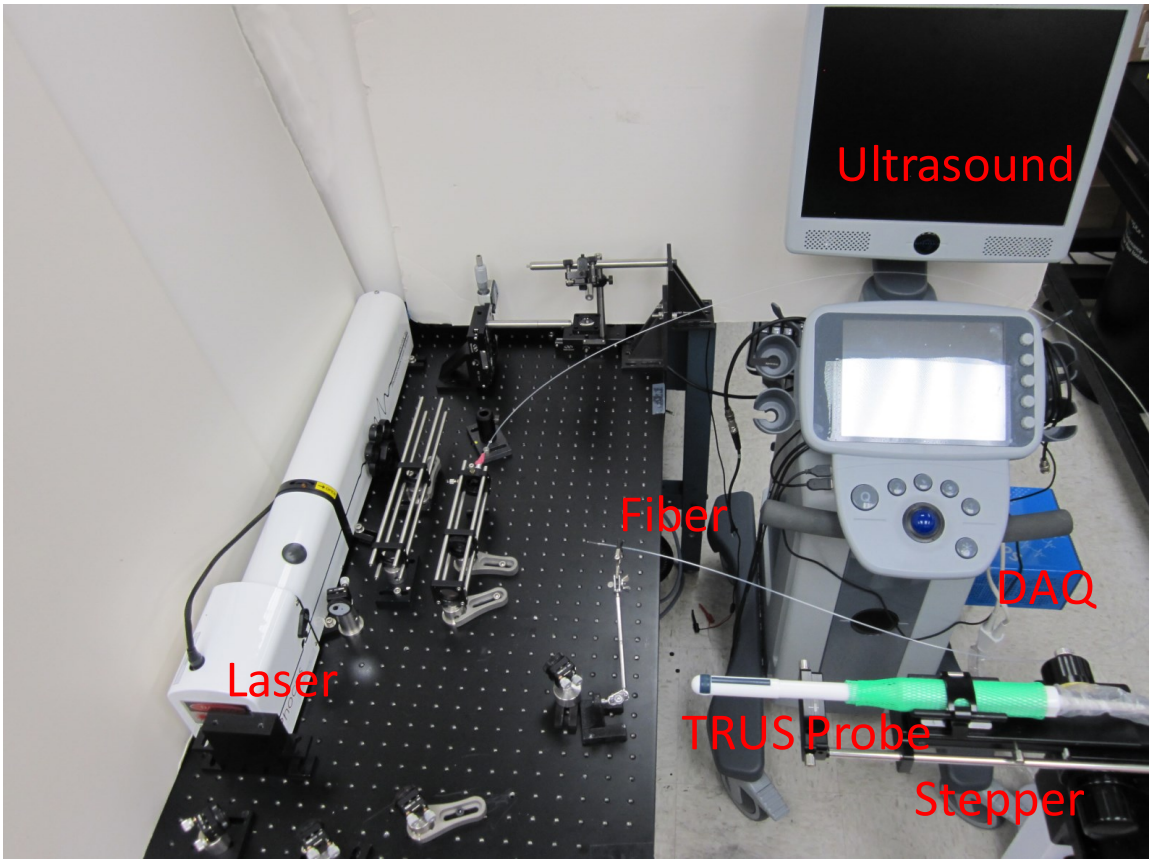

Figure 35 Photograph of photoacoustic imaging system setup in the laboratory.

The first component in our system was a tunable laser called the Phocus, which is composed of an optical parametric oscillator (Opotek Inc., CA, USA) attached to a neodymium-doped yttrium aluminum garnet (Nd:YAG) pump laser (Quantel, Bozeman, MT, USA). Even though the laser output of the optical parametric oscillator could have been used, we chose instead to operate from the alternative 1064 nm access port of the laser due to its high power. The maximum energy of the pump laser at this fundamental wavelength is 360 mJ/pulse, the pulse repetition rate was 10 Hz, and the pulse duration was 5 ns, therefore easily satisfying the thermal and stress confinement conditions for generating the photoacoustic effect efficiently. The laser was air-coupled into a 1 mm core diameter optical fiber with a 0.37 numerical aperture (Newport, CA, USA). All optics were securely positioned on a portable optical table (Thorlabs, Newton, NJ, USA) for transportation between the laboratory and OR.

The second component in our system was the SonixTouch (Ultrasonix, Richmond, BC, Canada), a diagnostic ultrasound system packaged with additional research functions. We equipped this ultrasound scanner with a standard clinical TRUS probe which has two 128-element transducers, a linear one to acquire sagittal images (model BPL9-5/55) and a curvilinear one to acquire axial images (model BPC8-4/10). The probe was locked into a clinical brachytherapy stepper (Nucletron, Veenendaal, The Netherlands). In addition, a data acquisition device known as the SonixDAQ (Ultrasonix, Richmond, BC, Canada) was attached to the ultrasound scanner to access the raw prebeamformed data that is required for photoacoustic imaging. The sampling rate of the SonixDAQ is 40 MHz, and was triggered by the flashlamp output signal of the Phocus. Any delays between the trigger signal and the emission of light were accounted for in the custom software of the SonixDAQ.

5.2.2 Delivering Laser Energy to the Seeds

Even though the photoacoustic setup described delivers sufficient laser energy through an optical fiber to generate the photoacoustic effect in seeds, there are several different approaches of light delivery for an actual patient setting. These include the external, needle, transrectal, and transurethral approaches (see Figure 36). The simplest of the approaches, the external approach, would not require the fiber to be inserted into the body, but would illuminate the seeds from outside the patient. Although it may be the most convenient option, it is doubtful that the external approach would generate images due to the amount of

tissue that would attenuate the laser energy between the fiber and the seeds. The second approach, the needle approach, which we opted to implement for the experiments in this chapter, would insert the fiber into the prostate like a brachytherapy needle. This has a significant advantage due to the proximity of the fiber to the seeds, but also has a major disadvantage because the tissue surrounding the fiber has a tendency to generate a photoacoustic effect of its own. The third approach, the transrectal approach, is also a feasible approach requiring a side-shooting fiber to be inserted along with the probe into the rectum, but there are concerns that fat, known to absorb 1064 nm light, would strongly attenuate the laser energy between the rectum and prostate. Finally, the last approach, the transurethral approach, would insert a side-shooting fiber through the urethra within a catheter to be in close proximity to the seeds, like the needle approach; however, it would be challenging to know which direction the fiber is oriented once inserted into the patient. As mentioned, we chose the needle approach for our experiments, but these alternatives may also be investigated to determine the configuration which produces the best results.

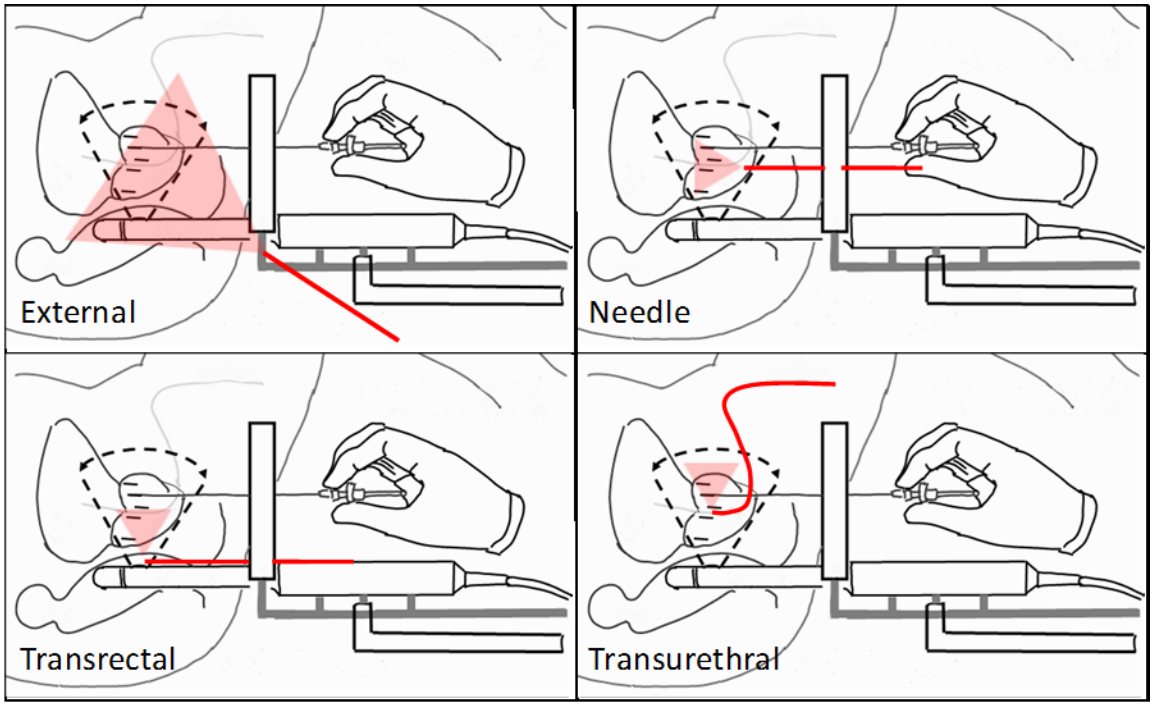

Figure 36 Illustrations of various feasible configurations to position the optical fiber (thick red line) for seed illumination (transparent red triangle) – external (top left), needle (top right), transrectal (bottom left) and transurethral (bottom right) approaches.

5.2.3 Maximizing Photoacoustic Signal

Even with a large optical fiber, it was difficult to generate sufficient photoacoustic signal, being especially limited by the MPE of 100 mJ/cm^2 at 1064 nm as defined by the American National Standard Institute. To satisfy this safety requirement while delivering sufficient laser energy, the free end of the optical fiber was inserted into a translucent plastic ProGuide needle (Nucletron, Veenendaal, The Netherlands), which is typically used for high-dose-rate brachytherapy (see Figure 37). These 24 cm long ProGuide needles have a hollow opening on one end with an inner diameter of 1.5 mm and outer diameter of 2 mm, and a closed conical pointed tip of 2 mm on the other end. The optical fiber, having a total diameter of 1.4 mm (including core, cladding, and coating) happened to fit snugly into the hollow needle. Since the needle is not fully transparent, a fiber sheathed with the needle was found to have approximately half the energy output as compared to an unsheathed fiber; at the same time, a sheathed fiber had eight times the surface area as compared to an unsheathed fiber. Both of these factors aid in reducing the energy density to satisfy the clinically safe energy density limit. In addition, a sheathed fiber was found to have an output that was more omnidirectional than an unsheathed fiber, which was favorable in attempting to image seeds that were to the side of the fiber.

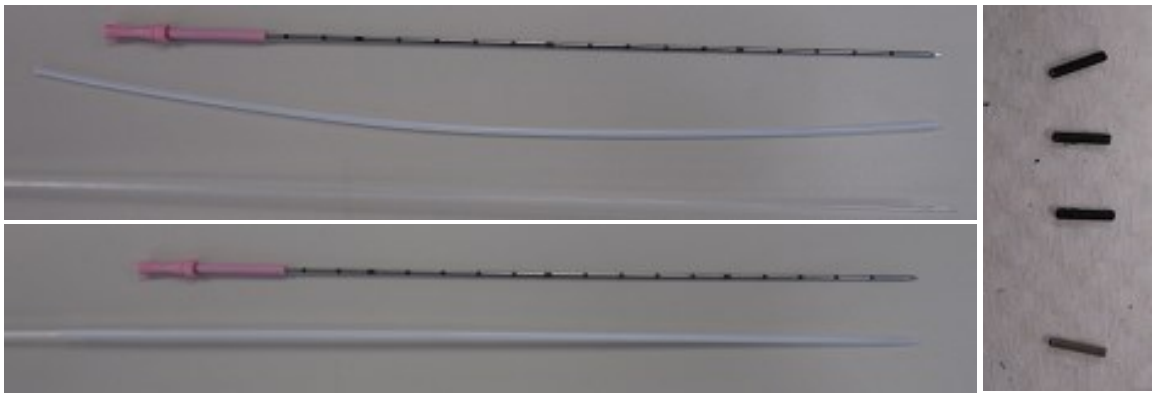

Figure 37 Photographs of needles and seeds. On the top left, PPB needle, ProGuide needle, and optical fiber are shown separately, while on the bottom left, the optical fiber is inserted into the ProGuide needle. On the right, three decayed seeds coated in India ink are shown above an uncoated seed.

Also in effort to maximize photoacoustic signal, decayed Palladium-103 brachytherapy seeds (Theragenics, Buford, GA, USA) of length 4.5 mm and diameter 0.8 mm were coated in black India ink

(see Figure 37). Black ink is reported to increase optical absorption in brachytherapy seeds, with approximately 18.5 dB increase in SNR and a doubling of imaging depth [48]. The seeds were coated by immersing the seeds in the ink and allowing them to air dry before applying another coat of ink. Each seed was coated at least three times before being used in experiments.

5.2.4 Signal Processing and Analysis

Once the raw prebeamformed data was acquired by the ultrasound transducer, the data needed to be reconstructed to form an image. The MATLAB simulation toolbox known as k-Wave [68] has a fast one-step image reconstruction function for linear and planar measurement surfaces which we used for reconstructing our sagittal data acquired by the linear transducer. While the k-Wave toolbox also has a slower time-reversal reconstruction for measurement surfaces of other geometries that may be used for reconstructing axial data acquired by the curvilinear transducer, most of our photoacoustic data were acquired by the linear transducer because of convenience. The resulting reconstruction was then envelope-detected and normalized to produce our final photoacoustic images.

To compare between reconstructions, several metrics were also calculated, including seed contrast (C), contrast-to-noise ratio (CNR), and signal-to-noise ratio (SNR). The equation used to compute contrast was:

$$C = 20\log_{10}\left(\frac{S_i}{S_o}\right)$$

where S_i and S_o are the mean signals at the same depth inside and outside the brachytherapy seed, respectively. Designating σ_o as the standard deviation of the signal outside the seed, CNR was calculated based on the following equation:

$$CNR = \frac{|S_i - S_o|}{\sigma_o}$$

Finally, SNR was calculated as:

$$SNR = \frac{S_i}{\sigma_o}$$

To make fair comparisons between reconstructions, the window size for determining S_i, S_o, and σ_o was also kept consistent within each dataset.

5.2.5 *In vivo* Dog Experiment

An *in vivo* dog experiment was conducted at the Johns Hopkins Medical Institutions (Baltimore, MD, USA) under the approval of the Animal Care and Use Committee. After the imaging equipment was transported and set up in the OR, the dog was anesthetized and placed on its back on the operating table under the care of veterinary technicians (see Figure 38). A prostate stepper template (Nucletron, Veenendaal, The Netherlands) was then inserted onto the stepper to guide the positioning of needles for both seed and fiber placement. Needles (brachytherapy and ProGuide), seeds (coated and uncoated), and the optical fiber were all implanted by an expert radiation oncologist with many years of experience treating human patients with PPB. Seeds were implanted by the standard method of puncturing the perineum with a PPB needle and dropping seeds through the hollow core of the needle. The optical fiber was implanted by first puncturing the perineum with the ProGuide needles stiffened by metal obturators; afterwards, the obturators were removed from within the needles to insert the fiber. Ultrasound images and photoacoustic data were then collected for different scenarios of fiber and seed placement within the prostate of the dog. Since tissue at the tip of the optical fiber also generates a photoacoustic effect and may consequently obscure the signal from seeds, images were intentionally taken with the transducer directed away from the fiber but towards the seeds, verified by ultrasound. At the end of the experiment, a cone-beam CT was taken of the seed-filled prostate with the dog still positioned on its back on the operating table.

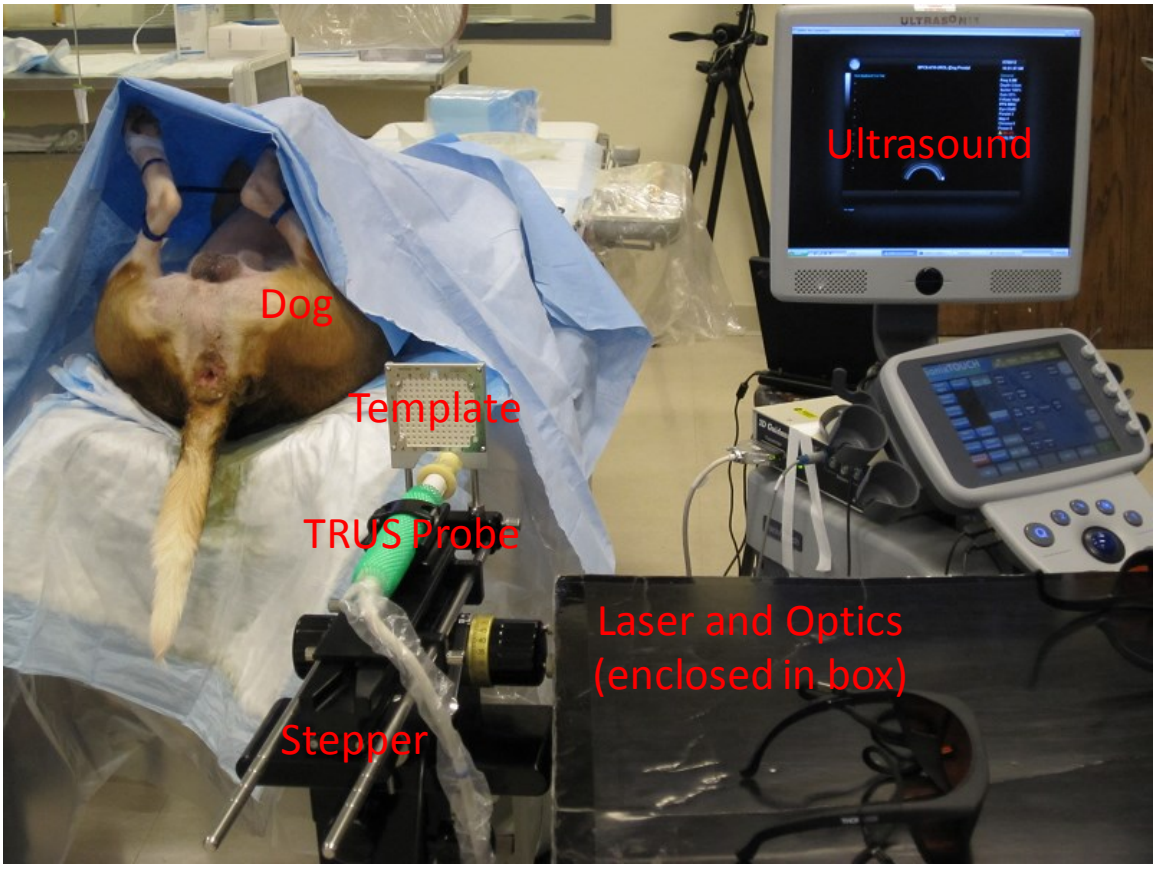

Figure 38 Photograph of photoacoustic imaging system setup in the OR.

Three particular scenarios were conducted in the dog (see Figure 39), all acquired by the linear transducer of the transrectal probe. In the first scenario, one uncoated seed was placed approximately 5 mm away from the sheathed optical fiber in the elevation direction. The second scenario was similar to the first, except a coated seed was placed instead of an uncoated seed. In the last scenario, three coated seeds were placed in a line along the axial direction, each approximately 5 mm apart from another (see Figure). The sheathed optical fiber was also positioned out of plane approximately 5 mm away in the elevation direction from the seed closest to the probe. In all these scenarios, photoacoustic images were acquired at various sampled energies between 0 to 11 mJ/pulse (i.e. approximately 0 to 175 mJ/cm^2), measured from the tip of the sheathed fiber, to determine how the images change with respect to energy.

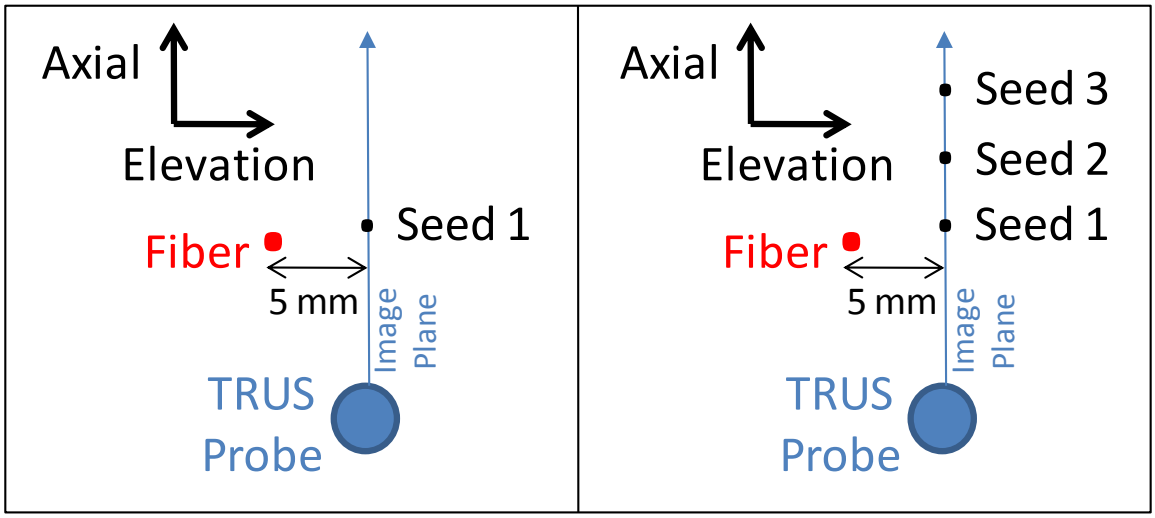

Figure 39 Illustrations of the positions of seed(s), fiber, and probe in the experiment. The left represents the first and second scenario with one uncoated and coated seed, respectively. The second represents the final scenario with three coated seeds.

5.3 Results and Discussion

The results of the first scenario with one uncoated seed are shown in Figure 40. The photoacoustic image clearly shows a signal at the location of the seed, even at the MPE of 100 mJ/cm^2. Contrast, CNR, and SNR also decrease in magnitude with decreasing energy, until finally reaching the sensitivity limit of the probe at around 3 mJ/pulse. Even though the photoacoustic image clearly shows a signal at the location of the seed, the undefined shape of the signal brings into question whether the signal is truly from the uncoated seed, or if it is actually from the photoacoustic effect of the tissue at the tip of the fiber. Even though the transducer was directed away from the fiber to avoid detecting the signal at the tip, it is possible that the transducer is still sensitive enough in the elevation direction at this distance to detect this photoacoustic effect, especially in the absence of other stronger signals.

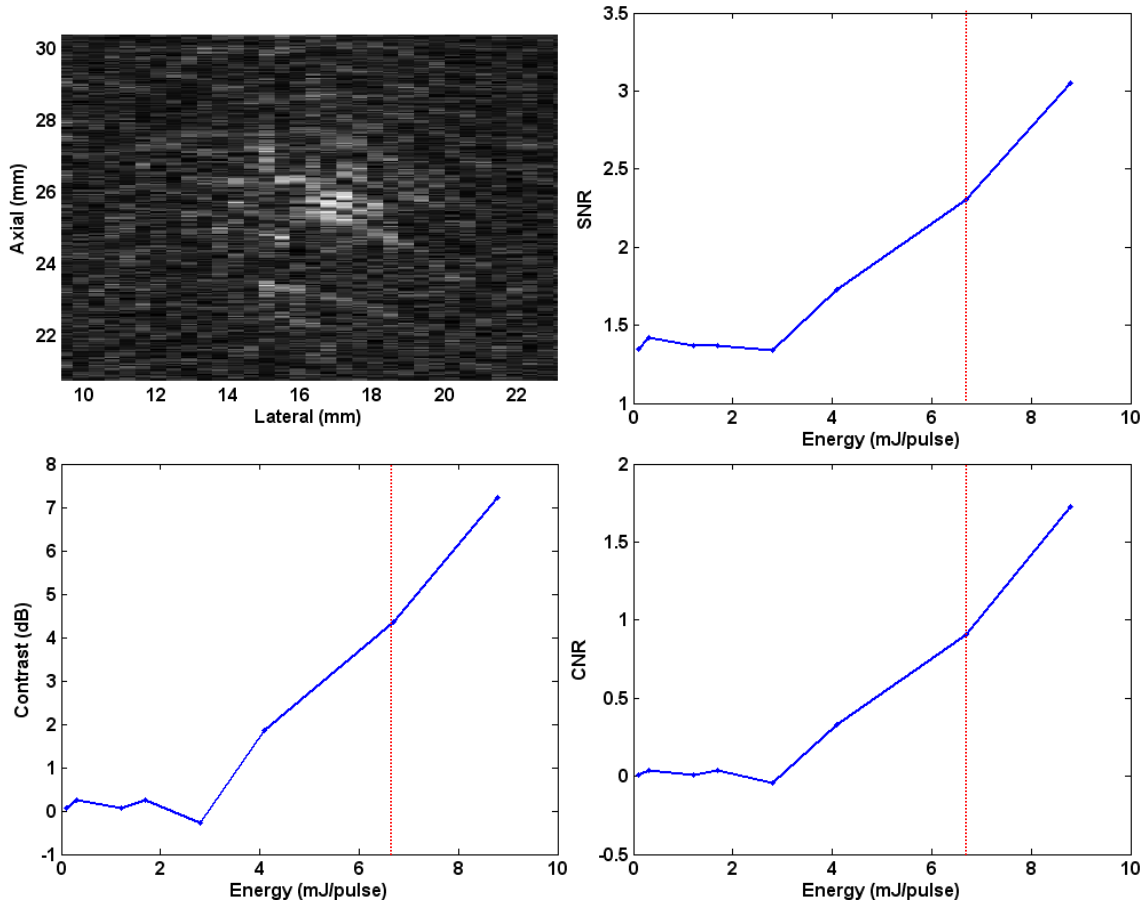

Figure 40 Results of imaging a single uncoated seed. Top left shows the processed photoacoustic image at MPE (red dotted line in plots); top right shows SNR with respect to energy; bottom left shows contrast with respect to energy; and bottom right shows CNR with respect to energy.

As opposed to the first scenario, the results of the second scenario with one coated seed clearly display the photoacoustic signal from the seed rather than the fiber, and are shown in Figure 41. The photoacoustic image, even at MPE, shows an approximately 4.5 mm bright linear-shaped signal, as would be expected from a seed, rather than a nebulous spot that would be expected of fiber. Two lines are also seen at the seed, which may be attributed to signal coming from the sides of the seed, or reverberations occurring within the seed. Furthermore, contrast, CNR, and SNR all decrease in magnitude with decreasing energy, until reaching the sensitivity limit of the transducer at around 2 mJ/pulse. Note, however, that the numbers between the coated seed and uncoated seed cases may not be directly compared since the scenarios, although similar, are not identical, especially having a large difference in imaging depth (26 mm

for the uncoated seed compared to 14 mm for the coated seed). Nonetheless, one of the main concerns for conducting photoacoustic imaging for PPB in live animals was the effect that tissue, water, and blood would have on image quality. Even though these constituents do absorb 1064 nm light, evident by signal at the tip of the fiber, this particular experiment shows that seeds may still be imaged clearly in their presence.

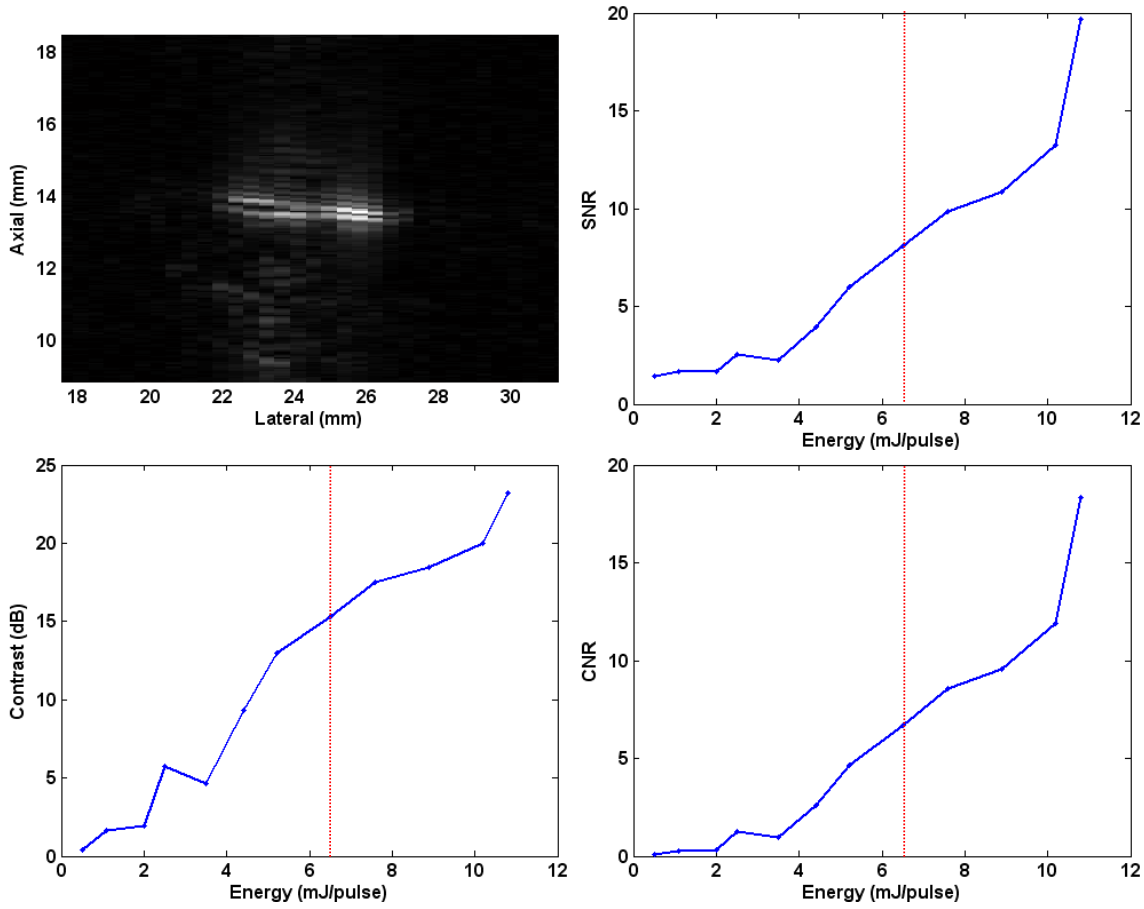

Figure 41 Results of imaging a single coated seed. Top left shows the processed photoacoustic image at MPE (red dotted line in plots); top right shows SNR with respect to energy; bottom left shows contrast with respect to energy; and bottom right shows CNR with respect to energy.

The results of the third scenario are finally shown in Figure 42. Although three seeds were implanted, evident in both ultrasound and CT images, only two seeds are visible in the photoacoustic image. Moreover, the contrast, CNR, and SNR of both seeds decrease with decreasing energy as expected, with Seed 1 having higher magnitudes than Seed 2 because it is both closer to the fiber and to the probe. There are also two other signals visible in the photoacoustic image. The one at an imaging depth of 8 mm is

confirmed to be from the fiber, which although is outside the imaging plane, is still detected. The other, located at an imaging depth of 20 mm, is an unknown artifact, being not visible in either ultrasound or CT. It is possible that it is the edge of the third seed, but its location is a bit too far from the probe to be the third seed. Another possible reason for this artifact is an accumulation of blood at that specific location which may especially absorb laser energy to generate such a photoacoustic signal. However, a more plausible explanation is that the artifact is a reflection of the fiber tip photoacoustic signal from Seed 2. The fiber tip was inserted approximately 7 mm away from Seed 2 (more precisely, $\sqrt{5^2 + 5^2} = 5\sqrt{2} \approx 7$ mm), and Seed 2 is approximately 13 mm from the probe, explaining the artifact's 20 mm position that is equivalent to the sum of the two distances. The higher intensity of the artifact compared to the fiber may also be due to the fact that the probe is oriented toward the reflection off Seed 2 but away from the fiber, therefore being more sensitive to the reflection rather than the fiber.

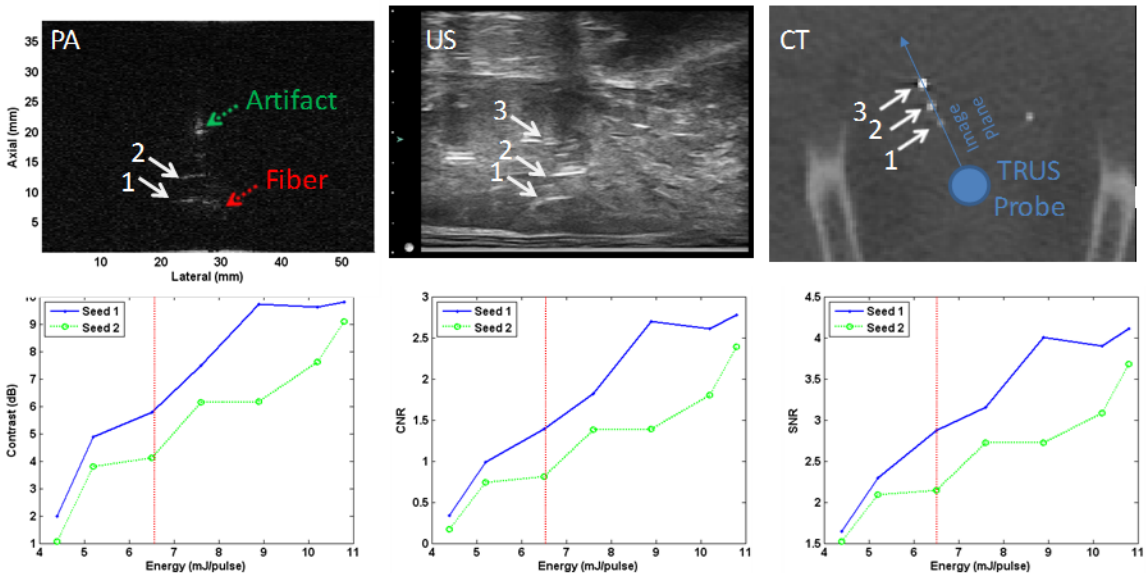

Figure 42 Results of imaging three coated seeds. Top row, from left to right, shows the sagittal photoacoustic image at MPE (red dotted line in plots), the sagittal ultrasound image aligned with the photoacoustic image, and an axial CT slice, respectively. Bottom row, from left to right, shows contrast with respect to energy, CNR with respect to energy, and SNR with respect to energy, respectively.

5.4 Conclusion

In this chapter, we presented a next generation photoacoustic imaging system for visualizing brachytherapy seeds in the OR. It is a vast improvement to our previous system as it includes a more powerful laser system, a more advanced ultrasound scanner, and additional essential components to make it viable in the OR. In addition, a translucent fiber sheath and coating of seeds enables the system to obtain stronger photoacoustic signals. Finally, experiments of an *in vivo* dog prostate demonstrate that single and multiple seeds are clearly visible in a live animal.

It is clear, however, that there are also potential problems with photoacoustic imaging for use in PPB that may be considered for future directions. First, the photoacoustic effect of tissue at the tip of the fiber is often detected, even when the probe is oriented so the fiber tip is outside the imaging plane. This may likely be avoided by another method of laser energy delivery such as the transurethral approach, which would have the fiber inserted into a catheter to allow more space between fiber and tissue, thus preventing a strong photoacoustic effect from occurring. Another option is to alter the tip of the fiber, perhaps by extending the surface area into a cylinder by which the laser energy may be emitted, so that the energy density may be reduced to diminish the photoacoustic effect from tissue. The most concerning issue, however, is the possible presence of false positive reflection artifacts in the photoacoustic images. More study is necessary to confirm if reflection artifacts are significant in photoacoustic imaging, and if so, innovative methods will be required to overcome such an issue.

Nonetheless, generating photoacoustic images of multiple seeds in a live animal is a significant step in making photoacoustic imaging possible for PPB patients. With additional research, photoacoustic imaging may become a standard means of intraoperative dosimetry in PPB.

Chapter 6. Conclusions and Future Directions

Two intraoperative dosimetry systems have been proposed. The first uses TRUS and mobile non-isocentric C-arm X-ray fluoroscopy to localize the seeds in relation to the prostate. The second takes the novel approach of photoacoustic imaging by adding a laser to the standard PPB clinical ultrasound system.

Both proposed systems are effective for seed localization. The TRUS-fluoroscopy system generates a mean registration error of 1.3 mm, while the photoacoustic system generates a contrast of up to 5.8 dB at MPE for multiple seeds simultaneously acquired in an *in vivo* dog prostate. Both systems are economical. Compared to other approaches that require expensive CT or MRI scanners, the system based on TRUS-fluoroscopy only adds a simple marker-based fiducial, while the one based on photoacoustic imaging requires just an addition of a laser. Finally, both systems are practical. Both the TRUS-fluoroscopy and photoacoustic systems incur few changes to contemporary clinical PPB procedures.

Specifically, my individual contributions in this dissertation were the following:

1. I have demonstrated an algorithm that simultaneously segments the tracking fiducial and brachytherapy seeds in fluoroscopic images, thereby minimizing the need for manual intervention. This algorithm successfully segmented the FTRAC with a rate of 88.3% on over 150 clinical images. Mean pose estimation errors were less than 1° in rotation and approximately 2 mm in translation. It also produced excellent seed segmentation results, with a false negative rate of 1.1% and false positive rate of 2.6% on over 7000 clinically implanted seeds. A majority of overlapping seeds were also detected and separated. The algorithm easily completed all the image processing within the several seconds it takes to position the C-arm from pose to pose. Moreover, segmentation did not require an ROI, allowing for direct pipelining from fluoroscopic image acquisition to seed reconstruction.
2. I have a demonstrated our next generation TRUS-fluoroscopy intraoperative dosimetry system based around a simple marker-based fiducial. The system portrayed a paradigm shift, requiring only a fiducial with at least 4 seed-like markers to significantly simplify workflow. The 4 image processing steps were all thoroughly tested and validated on 37 patients as approved by the

Institutional Review Board at the Johns Hopkins Hospital. Seed segmentation resulted in a 1% false negative rate and 2% false positive rate. Fiducial detection with pose estimation successfully detected 98% of the markers. Seed matching with reconstruction produced a mean reconstruction error of 0.4 mm. And fluoroscopy-to-TRUS registration generated a mean registration of 1.3 mm. Moreover, the system successfully identified cold spots that are so crucial to detect within the OR.

3. I have demonstrated a prototype photoacoustic imaging system for the localization of brachytherapy seeds. Starting with a clinical ultrasound scanner, a photoacoustic system was integrated with an addition of a pulsed laser using 1064 nm light. The photoacoustic system agreed closely with theory, showing minimal changes in SNR with variations in pulse repetition rate, but a linear increase in SNR with laser energy per pulse, and an exponential decrease in SNR with laser-to-seed distance. Moreover, the shape of the seed did not change with probe-to-seed distance, but displayed in correspondence with the respective orientation of the probe with the seed. Finally, the clinical feasibility of this system was shown as two seeds were clearly reconstructed in an *ex vivo* dog prostate.
4. I have demonstrated the next generation photoacoustic imaging system for the localization of brachytherapy seeds in a clinical setting. Fiber optics and equipment specific to PPB were included in the system, and the first known *in vivo* study of imaging seeds for PPB was conducted until the approval of the Animal Care and Use Committee at the Johns Hopkins Medical Institutions. While results for bare seeds proved inconclusive due to the possible detection of the photoacoustic effect at the fiber tip, coated seeds are clearly imaged with a contrast of 15 dB at MPE. Two seeds were also imaged simultaneously, showing that photoacoustic imaging is indeed feasible in an *in vivo* setting, despite possible negative effects of blood, water and tissue.

These individual contributions present solid progress towards bringing ITP into clinics worldwide. However, there are still several shortcomings that may be considered as future directions for research. Although the TRUS-fluoroscopy system is a mature project, there is still room for improvement, since the system requires a fiducial as well as a phantom for C-arm calibration. Fiducial-less reconstruction has been

attempted and has thus far has proven unfruitful, but it would be a valuable improvement if it can be made robust. C-arm calibration is also quite cumbersome but is required to correct image distortions and compute intrinsic camera calibration parameters. It may be possible to estimate these parameters without a calibration phantom, but doing so would require the system to be more robust to any imprecision that may result. For the photoacoustic system, there is much more room for future work as it is still in its adolescent stages. While we have implemented a real-time photoacoustic system, there are many limitations which cause it to have an unsatisfactory slow frame rate. Hardware upgrades to the DAQ device and software improvements are required to overcome this bottleneck. In addition, more investigation is required to determine if reflection artifacts are significant in photoacoustic imaging. If so, innovation is needed to eliminate these artifacts, including already present artifacts such as the one generated by the fiber tip. Imaging of many seeds has also not yet been done since it is difficult to fully illuminate the prostate. More advanced laser energy delivery methods beyond the standard optical fiber, including side-shooting or cylindrically-shooting fibers, should be investigated. Finally, the work presented in this dissertation show 2D photoacoustic images but 3D photoacoustic volumes should eventually be collected. If energy delivery becomes resolved so a large volume is illuminated, the 2D slices should then be integrated to image the seeds in 3D.

Despite these shortcomings, the work presented in this dissertation lays a foundation for future research in this area. The contributions have also made significant strides for improving healthcare technology in our world. Only time will tell how much impact these contributions will have, but it is conceivable that we will see these two intraoperative dosimetry systems being used on a loved one, or even on ourselves, some day.

Appendix A.The Registration of Ultrasound and Fluoroscopy Graphical User Interface

The contents of this appendix present an overview of the MATLAB graphical user interface (GUI) we have developed to aid the Registration of Ultrasound and Fluoroscopy (RUF) project. Although the software is by no means intended for commercial use, it has proved to be indispensible in the transition from the previous generation of the TRUS-fluoroscopy intraoperative dosimetry system presented by Jain et al. [20, 21] to the latest generation of the RUF system. The following may be considered as a user manual for the readers who are interested in operating the software.

A.1 The rufMainGUI Window

The RUF GUI is executed by running rufMainGUI.m within MATLAB, the simplest method of which is to enter "rufMainGUI" in the command window once the current folder is set to the Main_GUI directory of the RUF program. Once executed, the rufMainGUI window should appear (see Figure 43).

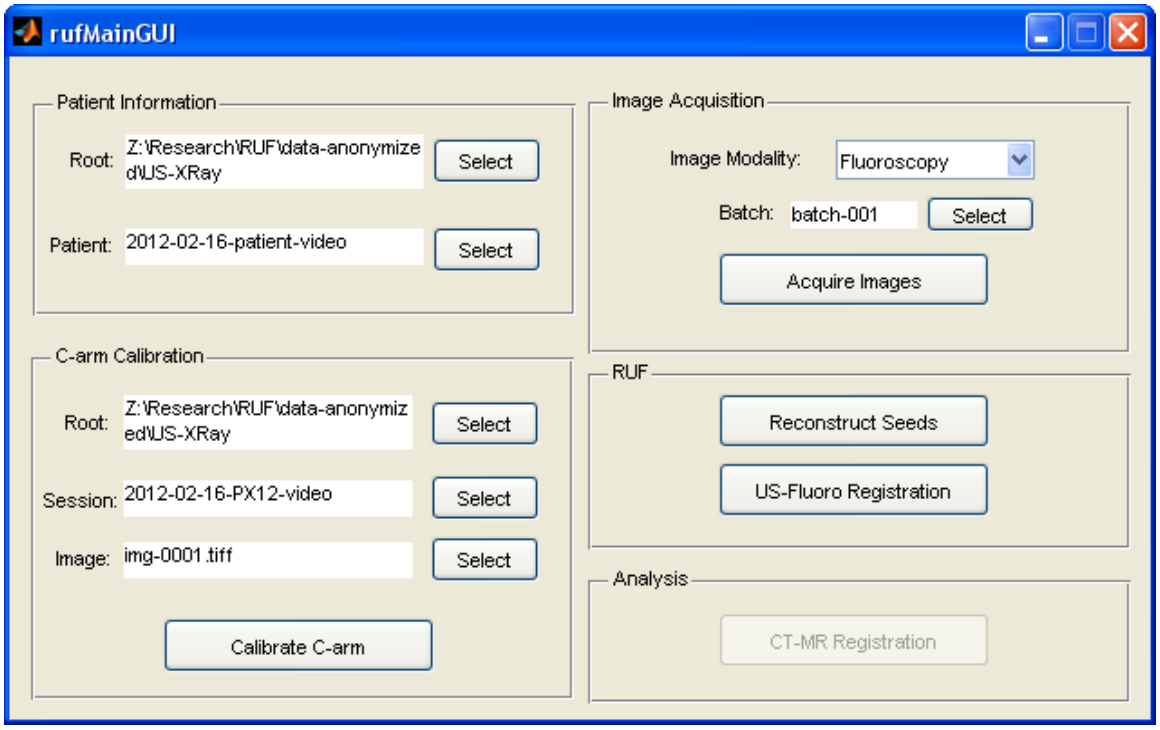

Figure 43 The rufMainGUI window

There are several panels in the rufMainGUI window each with their own title – Patient Information, C-arm Calibration, Image Acquisition, RUF, and Analysis. The final panel of Analysis is under development and beyond the scope of this dissertation and will therefore be excluded from this manual. Within the remaining panels are several buttons, but the ones named Calibrate C-arm, Reconstruct Seeds, and US-Fluoro Registration are the lengthiest to describe and are thus saved for later sections. The remaining buttons are explained in this section, which have the function of selecting identifiers, directories and files that are essential for the algorithms in the program to operate.

First, the root directory, located as the first entry in both the Patient Information and C-arm Calibration panels, indicates the file path in which all data will be stored. The Select buttons next to these root directory entries pop up a window that allows the user to select or make a new folder to serve as the root directory. As a convenient feature, the root directory path is saved every time the program is closed so it may begin with the most recently selected root directory when the program is reopened.

Next is the patient ID, which is located as the second entry of the Patient Information panel. This entry contains the date of an operation as well as an identifier for the specific patient. It also selects the

appropriate patient directory in the internal file system of the GUI to store the patient's data. The Select button next to the patient ID entry pops up a window to select the directory of a previous patient or to create a new patient directory for which to acquire data (see Figure 44). If adding a new patient is desired, the patient ID indicated by the user is automatically prefixed with the current date. By default, the latest patient ID is selected when the RUF program is opened.

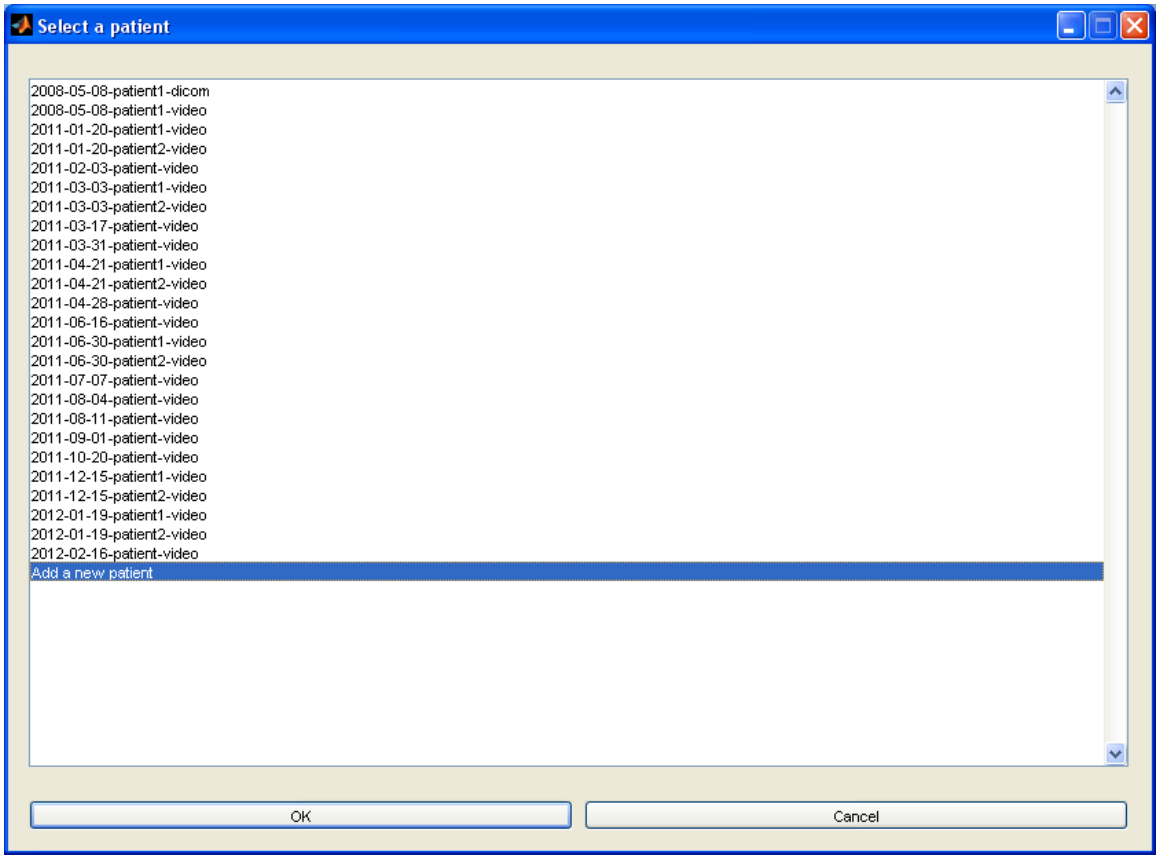

Figure 44 Selecting a patient ID

Similar to patient ID is the calibration session, located as the second entry of the C-arm calibration panel. Like patient ID, this entry contains the date of a C-arm calibration as well as an identifier for that particular calibration. It also selects the appropriate internal directory to store the calibration data. The corresponding Select button is very similar to the one for patient ID, in that the user may select a previous calibration session or create a new calibration session which is automatically prefixed with the current date (see Figure 45). By default, the latest calibration session is selected when the main program is opened.

Also, since C-arm calibration must be done the day of each patient case, the dates on the patient ID and calibration session must agree or a warning message will appear.

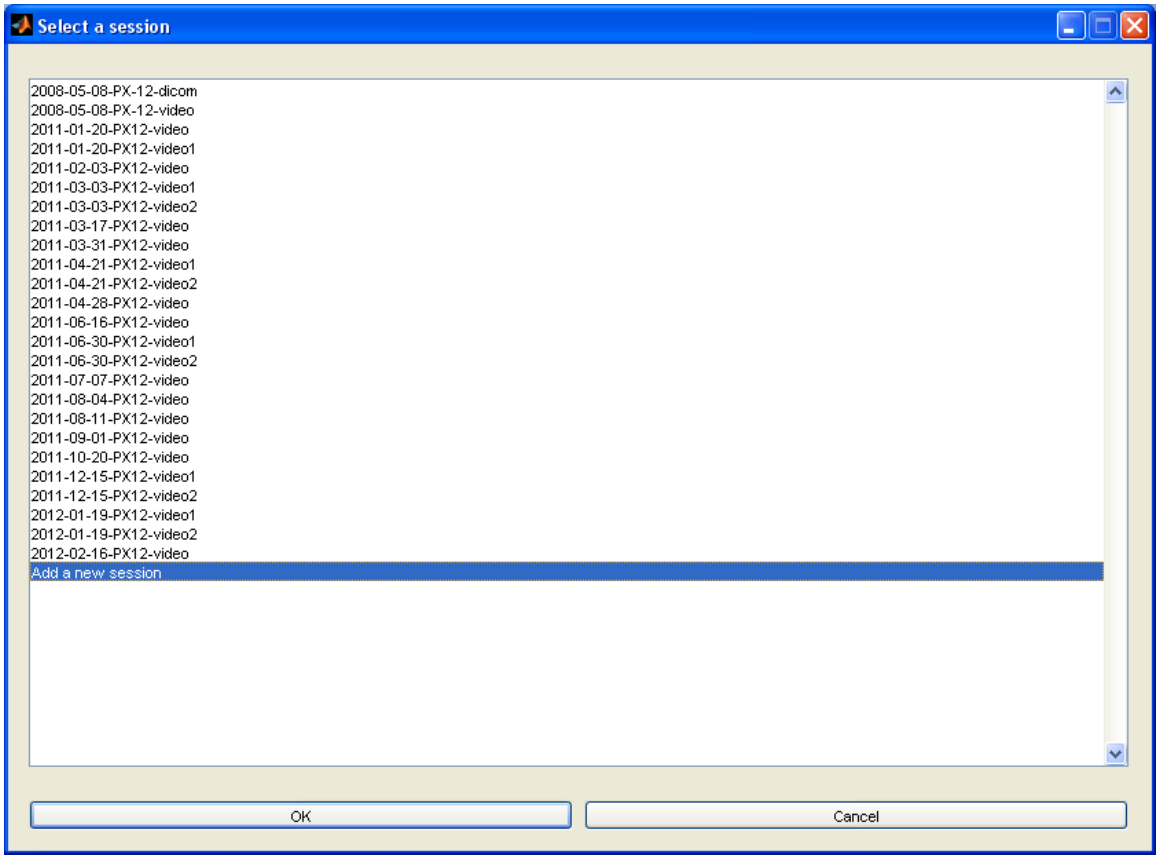

Figure 45 Selecting a calibration session

Once the calibration session has been identified, the particular calibration image must also be selected. This is indicated by the third Image entry in the C-arm Calibration panel. Multiple images may be collected for C-arm calibration although only one is needed. The corresponding Select button therefore pops up the rufCalibImageSelection window which allows the user to select a previous calibration image or to acquire/import a new one (see Figure 46). By default, the latest calibration image for the chosen calibration session is selected when the program is opened. Fluoroscopic images, including calibration images, may be acquired directly by the RUF program, assuming a framegrabber is connecting the C-arm to the computer. However, it is often more convenient to acquire images by the framegrabber's own software. There is therefore also an option to import, rather than acquire, images when the Acquire New button in the rufCalibImageSelection window is pushed. Thus, images are often acquired by the

framegrabber's software and then imported into RUF by this function. Whether acquired or imported, each calibration image is automatically named sequentially for easy identification.

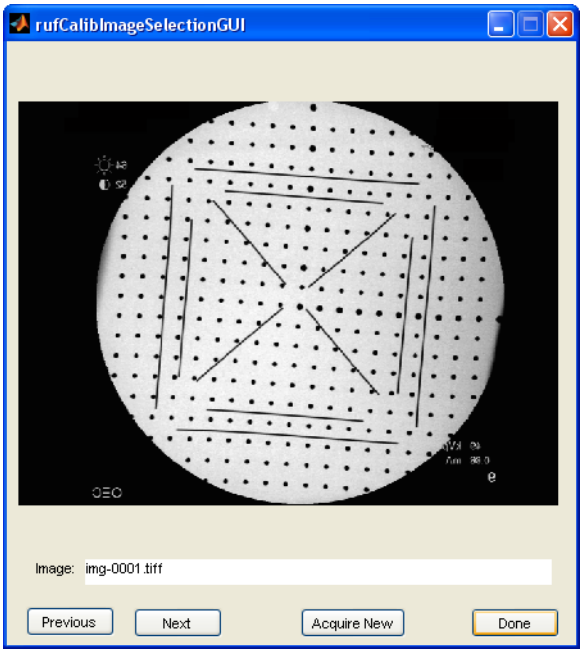

Figure 46 Selecting a calibration image

While one image is required for calibration, multiple images are required for patient data, since a set of three or more distinct images is needed for fluoroscopic reconstruction, and a collection of images is needed to form an ultrasound volume. These groups of images are referred to as "batches", and may be selected for both fluoroscopy and ultrasound using the Select button next to the Batch entry and depending on the entry selected in the Image Modality drop-down menu within the Image Acquisition panel of the rufMainGUI window (Figure 47). While more images may be acquired, the RUF program can only display 12 fluoroscopy images within a batch at a time; for ultrasound, the images are stacked to form a volume so the only limit to the number of images is from memory constraints. By default, the latest fluoroscopy and ultrasound batches for the chosen patient ID are selected when the program is opened. Note that the images within a batch should be acquired at the same time point within the brachytherapy operation, i.e. no additional seeds should be implanted until all images in a batch are acquired. Like calibration images, fluoroscopic patient images may be acquired directly by the RUF program but it is often more convenient to import images. The Acquire Images button of the Image Acquisition panel will offer both options of

acquiring and importing for fluoroscopy. For ultrasound, there is no option to directly acquire images into RUF, and therefore the Acquire Images button will only import images when the Image Modality menu is selected as Ultrasound. Ultrasound images are typically acquired by the treatment planning software (e.g. VariSeed or RadVision) and then imported into RUF through this function. Like for calibration images, whether acquired or imported, each batch and each image is automatically named sequentially for easy identification.

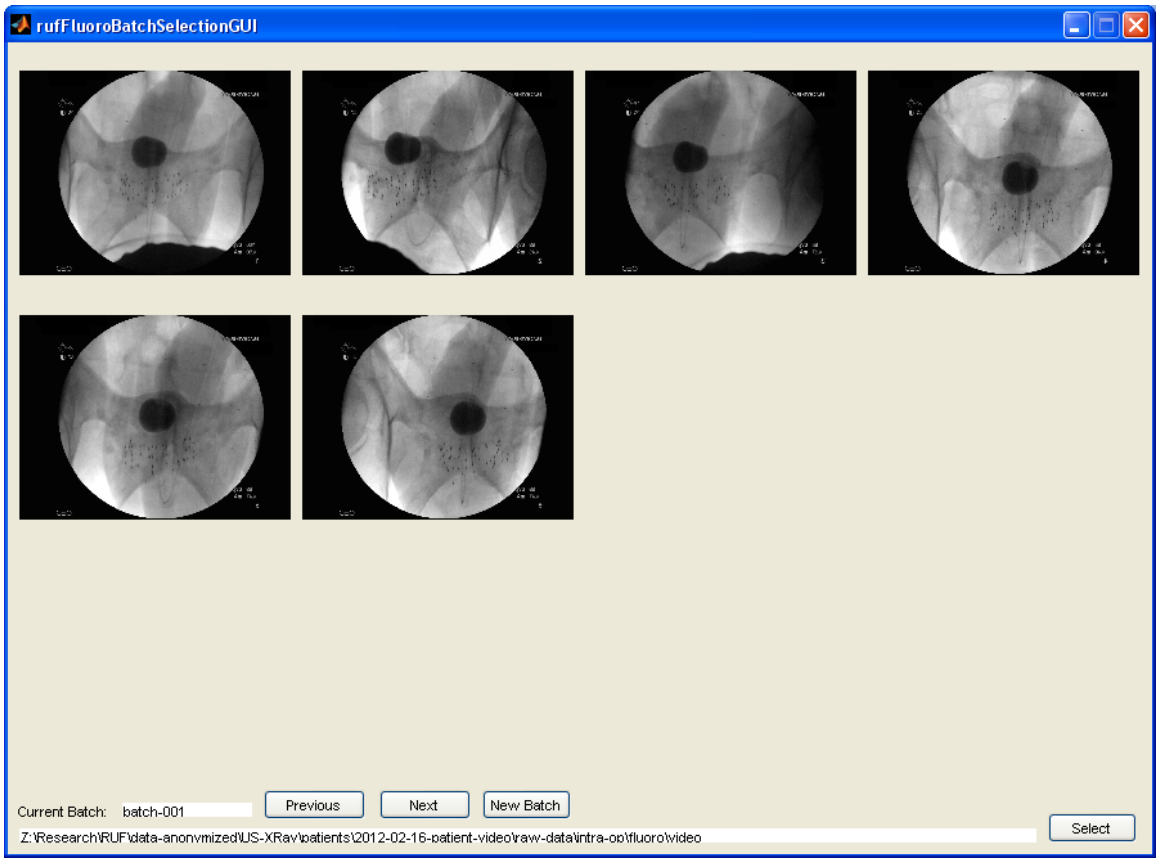

Figure 47 Selecting a fluoroscopic batch

Before acquiring fluoroscopy images, however, note that C-arm calibration (see Section A.2) must be completed before the Acquire Images button is pushed. The reason for this is that a series of algorithms that depend on C-arm calibration are immediately executed once a fluoroscopy image is acquired or imported. Those particular algorithms include image masking, distortion correction, seed segmentation, fiducial detection, and pose estimation, altogether taking less than 10 seconds per image to run. The results

of these algorithms may later be manually corrected by pushing the Reconstruct Seeds button under the RUF panel of the rufMainGUI.

Finally, to exit the program, simply press the red X at the top right corner. The root directory will be saved automatically for the next time the program is opened.

A.2 The rufCalibrationGUI Window

The rufCalibrationGUI window appears when the button called Calibrate C-arm under the C-arm Calibration panel in the rufMainGUI window is pushed (see Figure 48). This window performs the functions of calibrating the C-arm using the selected calibration image, which is initially displayed in the window. The calibration image is a shot of a two-plane calibration phantom (made of a grid of BBs on the first plane closer to the C-arm detector and a series of lines on the second plane farther from the detector) that should be taken on the day of patient image acquisition.

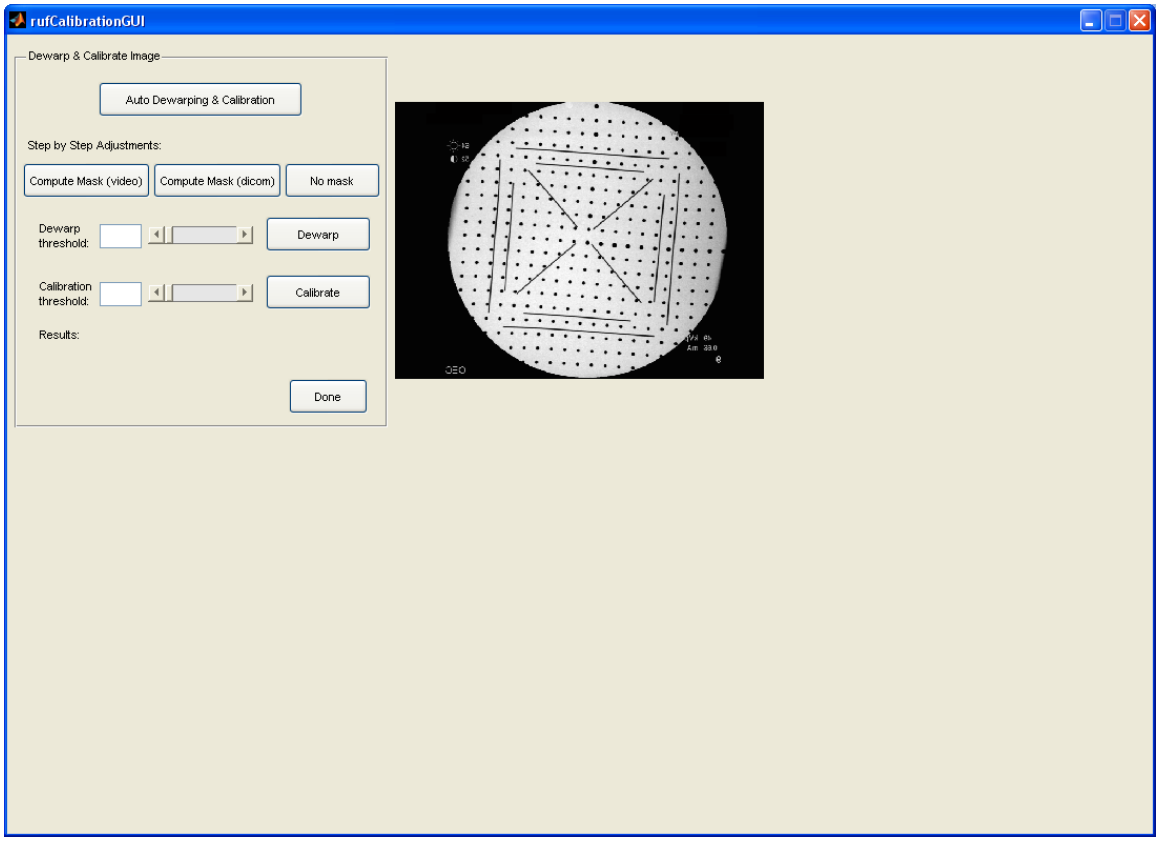

Figure 48 The rufCalibrationGUI window before calibration.

The selected calibration image is automatically displayed.

The rufCalibrationGUI window has three main buttons – Compute Mask (video), Dewarp, and Calibrate. Each of these buttons executes an algorithm that is necessary to calibration the C-arm. There is also a fourth button called Auto Dewarping & Calibration. This button pipelines the three tasks of calibration so that the algorithms run sequentially without the need for the user to push each of the three buttons individually. When each calibration algorithm is executed, rufCalibrationGUI displays the relevant images and numbers that result from each algorithm for verification purposes (see Figure 49). All algorithms together generally take less than 20 seconds to run.

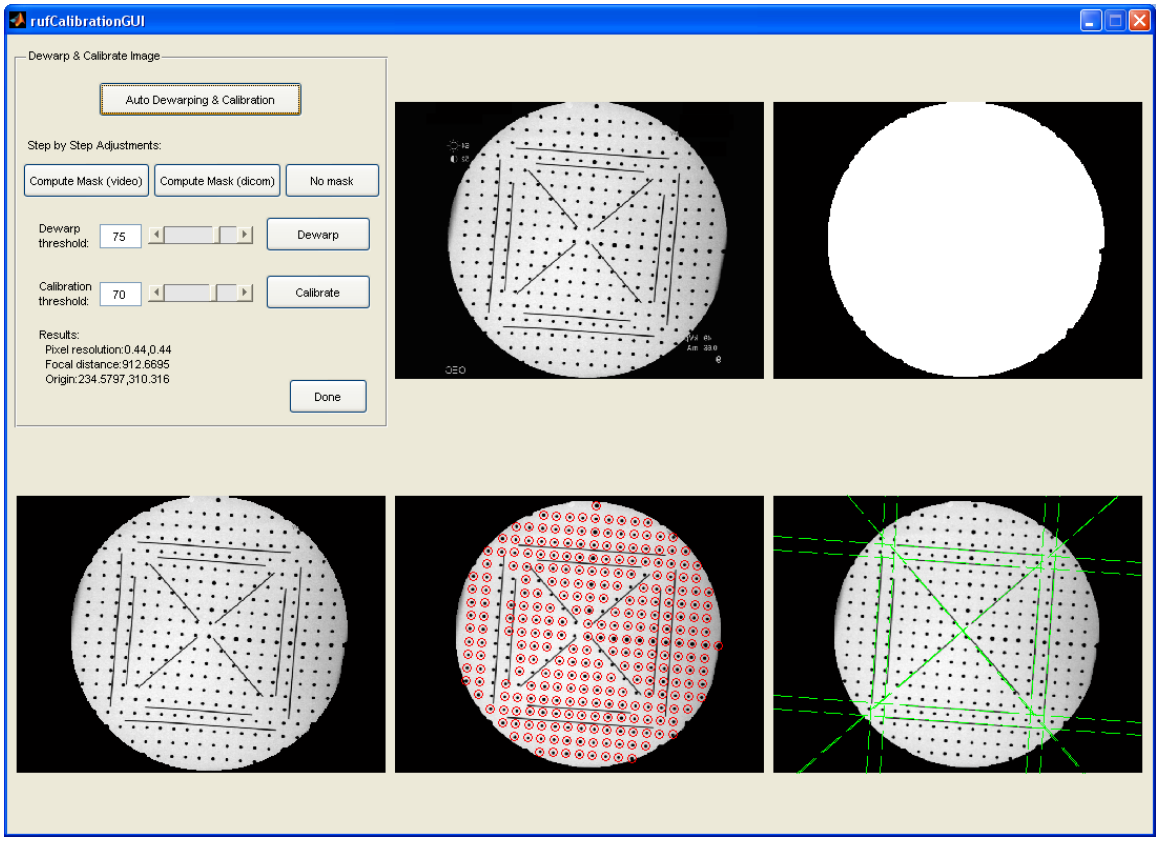

Figure 49 The rufCalibrationGUI window after calibration.

The image mask (top right), masked image (bottom left), bead-segmented image (bottom middle), and line-segmented image (bottom right) are displayed as the calibration algorithms are executed.

The first of the three calibration functions is Compute Mask. Its purpose is to compute an image mask to apply to the calibration image. Images taken with the C-arm generally include information, such as patient and surgeon names, contrast information, and X-ray imaging parameters, within the image but outside the C-arm field of view. This information needs to be removed because image processing algorithms that are to be later applied would generate erroneous results with the information remaining in the image. There are three different masks that may be computed, including Compute Mask (video), Compute Mask (dicom), and No mask. Of these three, Compute Mask (video) is most commonly used and is in fact the default method of computing mask when the Auto Dewarping & Calibration button is selected, since calibration images are generally video captured by a framegrabber. Although much less frequently used, Compute Mask (dicom) is still available in case DICOM calibration images are available.

The user also has the option of choosing No Mask, which skips the step of computing a mask, in case that method is desired. Moreover, all three of these options automatically compute a Dewarping threshold based on the histogram of the calibration image for the next step in the calibration pipeline.

The second of the three calibration functions is Dewarp. Its purpose is to segment the BBs of the calibration image and compute a distortion map from the segmentation. This step is needed to produce the precise calculations that are needed to reconstruct the implanted seeds from the C-arm images. The calibration phantom that is imaged was designed with a perfectly aligned grid of BBs. However, even though the image should theoretically display the grid of BBs perfectly aligned with proper perspective projective geometry, the image is warped due to magnetic field distortions caused by the environment affecting the C-arm electronics. Dewarp therefore segments the BBs, matches each BB with its true grid location and reverses the image distortion generated by the C-arm. It also enforces a fixed pixel resolution of 0.44 mm/pixel. Moreover, it automatically computes a Calibration threshold for the next step of the calibration pipeline.

Finally, the last of the three calibration functions is Calibrate. Its purpose is to compute the intrinsic camera parameters of the C-arm, particularly, focal distance and origin. These parameters are necessary for other image processing steps, particularly fiducial detection, pose estimation, and reconstruction. To compute these parameters, Calibrate first segments the 12 lines in the second plane of the calibration phantom. It then calculates the intersection of planes generated by these segmented lines in the imaging plane and the true manufactured positions of these lines to compute the focal length and origin.

All outputs are automatically saved in files within appropriate internal folders as each algorithm is executed. To exit the rufCalibrationGUI window, press Done or close the window by pushing the red X at the top right corner.

A.3 The rufReconGUI Window

The rufReconGUI window appears when the button called Reconstruct Seeds under the RUF panel in the rufMainGUI window is pushed (see Figure 50). This window performs the function of processing the batch of fluoroscopic images, which is initially displayed in the window, to eventually form

a 3D reconstruction of seeds. As mentioned in Chapter 2, there are four main steps to our TRUS-fluoroscopy system. This window covers three of these steps, particularly seed segmentation, fiducial detection with pose estimation, and seed matching with reconstruction. The window for the fourth of these steps, i.e. fluoroscopy-to-TRUS registration, is covered in Section A.4. The first two steps, i.e. seed segmentation and fiducial detection with pose estimation, have already been performed on the images by this stage since they were executed immediately when the images were acquired. The results of those algorithms are displayed under each image in the form of the number of seeds segmented, shown in brackets by the image name, and the mean residual error of the estimated pose.

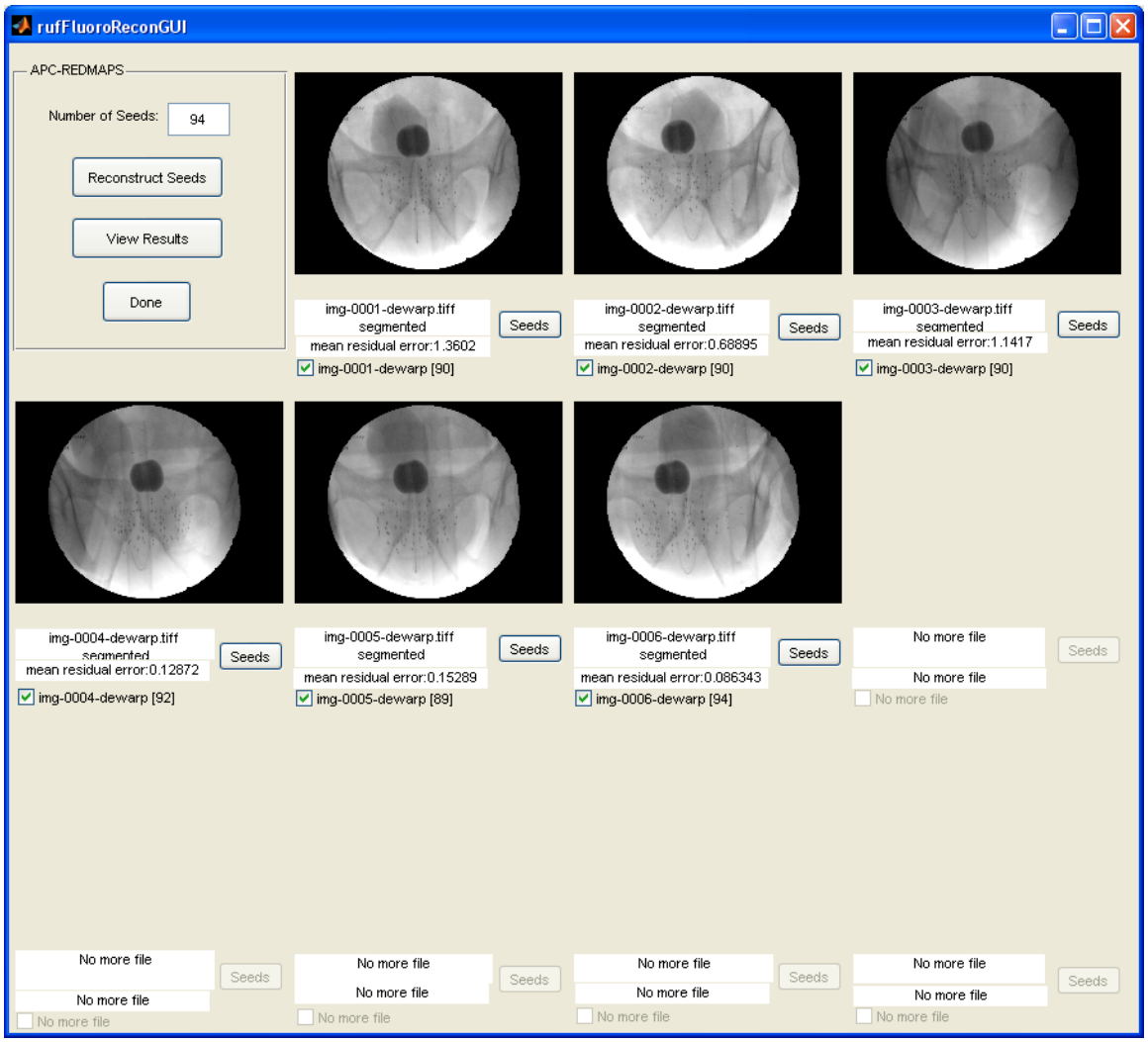

Figure 50 The rufReconGUI window.

The batch of fluoroscopic images is initially displayed.

Even though seed segmentation and fiducial detection with pose estimation have already been executed on these images, there may be some errors in the automatic processing of these images. To manually correct errors, select the Seed button by the particular image that needs to be corrected. When selected, the following seed segmentation window with the corresponding image should appear (see Figure 51).

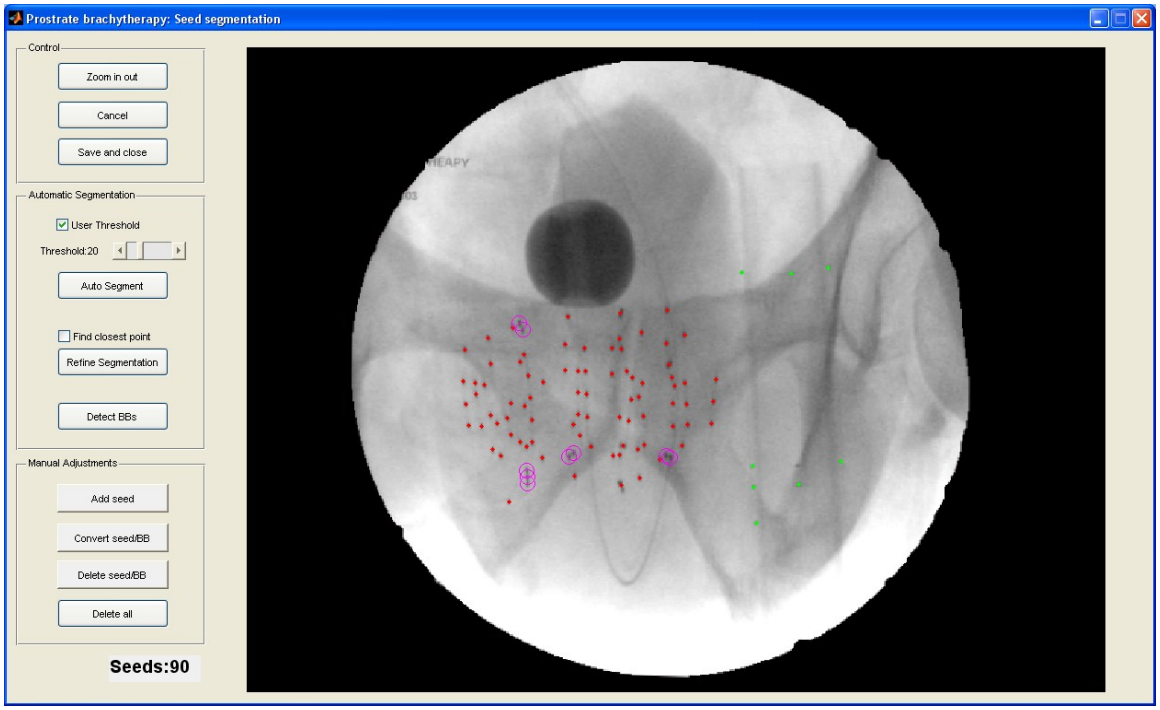

Figure 51 The seed segmentation window.

In this seed segmentation window, points identified as single seeds appear as red dots, points identified as overlapping seeds appear as magenta circles, and points identified as fiducial markers appear as green dots. Some points may not actually be seeds or markers, however, and are therefore false positives; there may also be some seeds or markers that have not been identified and are therefore false negatives. There are two main options to correct the segmentation. First, one may reuse the automatic seed segmentation and fiducial detection algorithms. To apply the seed segmentation algorithm, push the Auto Segment button, and the entire image will be resegmented. Since seed segmentation depends on a threshold to binarize the image, there is also an option to apply a user selected threshold or to use an automatic threshold for more accurate seed segmentation. To apply a user selected threshold, check the User

Threshold checkbox and adjust the Threshold slider bar to select an appropriate threshold; otherwise, to use an automatic threshold, uncheck the User Threshold checkbox. It may also be advantageous to select an ROI for seed segmentation. To do so, press the Zoom In Out button, then click-and-drag the mouse over an ROI. Then push Auto Segment to apply auto segmentation again. Fiducial detection with pose estimation may also be reused. To do so, simply push the Detect BBs algorithm, and the fiducial detection algorithm will run on the segmentation currently in the window. The other option to correct the segmentation is to do so manually. There are three methods to manually correct segmentation, all of them rather self-explanatory. To add seeds, choose the Add Seed button and click on the image to add red segmented points to the image. For some computer assistance, the Find Closest Point checkbox may be checked to automatically segment the closest darkest point to the user's mouse clicks. To delete segmented points, choose the Delete Seed/BB button and click near a segmented point (whether red, green, or magenta). If the mouse is clicked far from a segmented point, an error message will appear to advise the user to select closer to a segmented point. And finally, to identify a segmented point as a seed or fiducial marker, choose the Convert Seed/BB button and click near a segmented point to change the color from red/magenta to green (for marker) or from green to red (for seed). Again, an error message will appear if the mouse is clicked too far from a segmented point. There is also one more function in the seed segmentation window, which is Refine Segmentation. This function will perturb all the segmented points so each will fall on the darkest spot in its vicinity. This may be useful, but could also cause errors, especially for overlapping seeds. Finally, to close the segmentation window, either click the Save and Close button or click the Cancel button. Save and Close will estimate pose if not already done so for the new segmentation, save the results, and close the window. Cancel will close the window without saving, and pushing the red X at the top right corner performs the same function as Cancel.

Once the images have been corrected, we may proceed to the next step of the pipeline, which is seed matching with reconstruction. To run reconstruction with APC-REDMAPS, simply check the checkboxes next to the images that are to be used for reconstruction (as few as 3 and as many as 6 images). If there are more images than necessary in a batch, a good rule of thumb to obtain the best reconstruction is to select the combination of images with the lowest mean residual pose errors and have seed segmentation

numbers close to the true number of seeds. Once the images are selected, enter the actual number of implanted seeds in the Number of Seeds entry (by default, it is set to the maximum number of segmented seeds among all images in the batch), and push the Reconstruct Seeds button. The program will then execute APC-REDMAPS, save the results, and show a message box when it is finished. While the program is running, the user may look at the MATLAB command window to see how the APC-REDMAPS computations are going. A rule of thumb to see if it is running well is to verify that eta (the dimensionality reduction threshold) is decreasing per iteration. The ultimate solution (sometimes the penultimate solution if the ultimate iteration fails) should also be optimal with a low eta. Completion may take as little as a minute to as much as a few hours to run, depending mostly on the number of images and the number of implanted seeds. Once APC-REDMAPS is done, click the View Results button and select the reconstruction file to open (identifiable by the image names concatenated together) to open the rufFluoroResultsGUI for that reconstruction to verify correctness.

The rufFluoroResultsGUI window allows the user to check if the reconstruction is accurate. If it is not accurate, the user must go back to the rufFluoroReconGUI window to correct any problems in seed segmentation or pose estimation. The rufFluoroResultsGUI has two main methods to verify reconstruction: 1) the back-projected images, and 2) the projection views. Click the Previous or Next buttons to rotate among the back-projected images and the projection views.

The back-projected images (see Figure 52) show the back-projected points of the reconstruction overlaid on each of the segmented images. Segmented seeds are identified as red dots, while the back-projected reconstructed seeds are identified as magenta circles. Likewise, segmented markers are identified as green dots, while the back-projected reconstructed markers are identified as yellow circles. The user should verify that for each image, each segmented seed (red dot) has a corresponding reconstructed seed (magenta circle), and each segmented marker (green dot) has a corresponding reconstructed marker (yellow circle). The user should also verify that reconstructed single seeds (lone magenta circle) are indeed single seeds while reconstructed hidden seeds (magenta circles closely overlaid on each other) may indeed truly be hidden seeds.

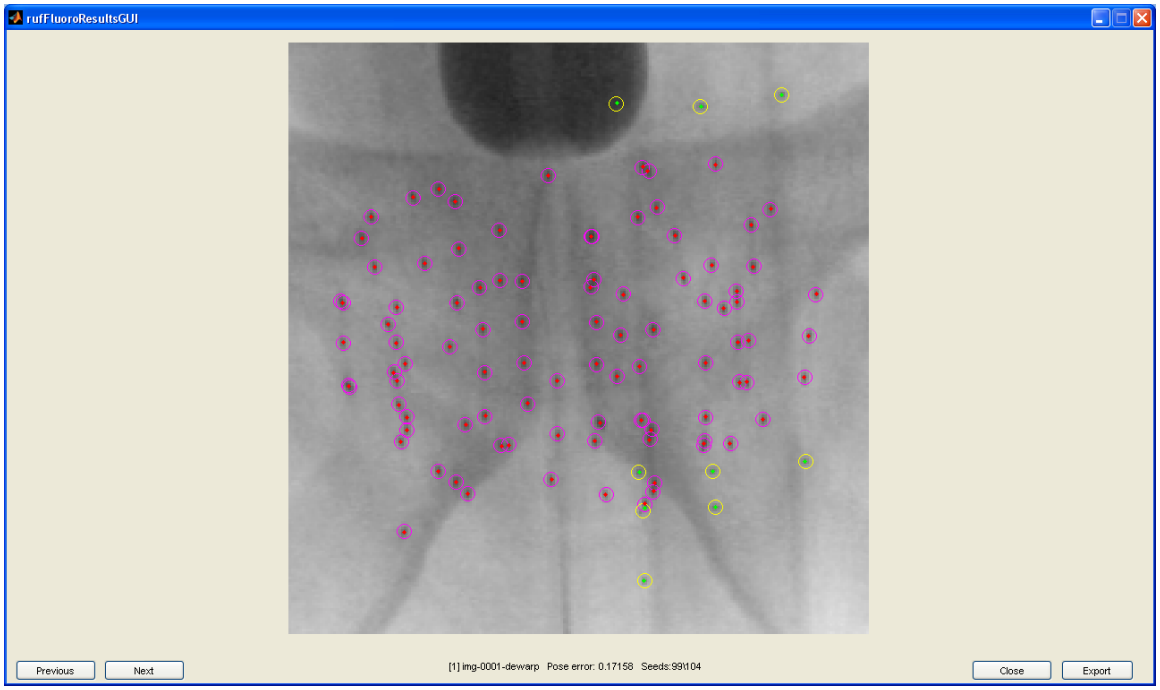

Figure 52 The rufFluoroResultsGUI window: Back-projected image

The projected views (see Figure 53) show the reconstruction projected on each of the coordinate axes – axial, coronal, sagittal. This is helpful to identify any errors that are not obvious in the back-projected images. The user should verify that the seeds are clustered in a cloud and that there are no stray reconstructed seeds separate from the others. Stray reconstructed seeds often mean a matching error and the user should therefore go back to the segmented images to especially segment overlapping seeds that may be manually resolved. Note that the grids on the projected views are inaccurate since they were first implemented in conjunction with the FTRAC but have now become obsolete.

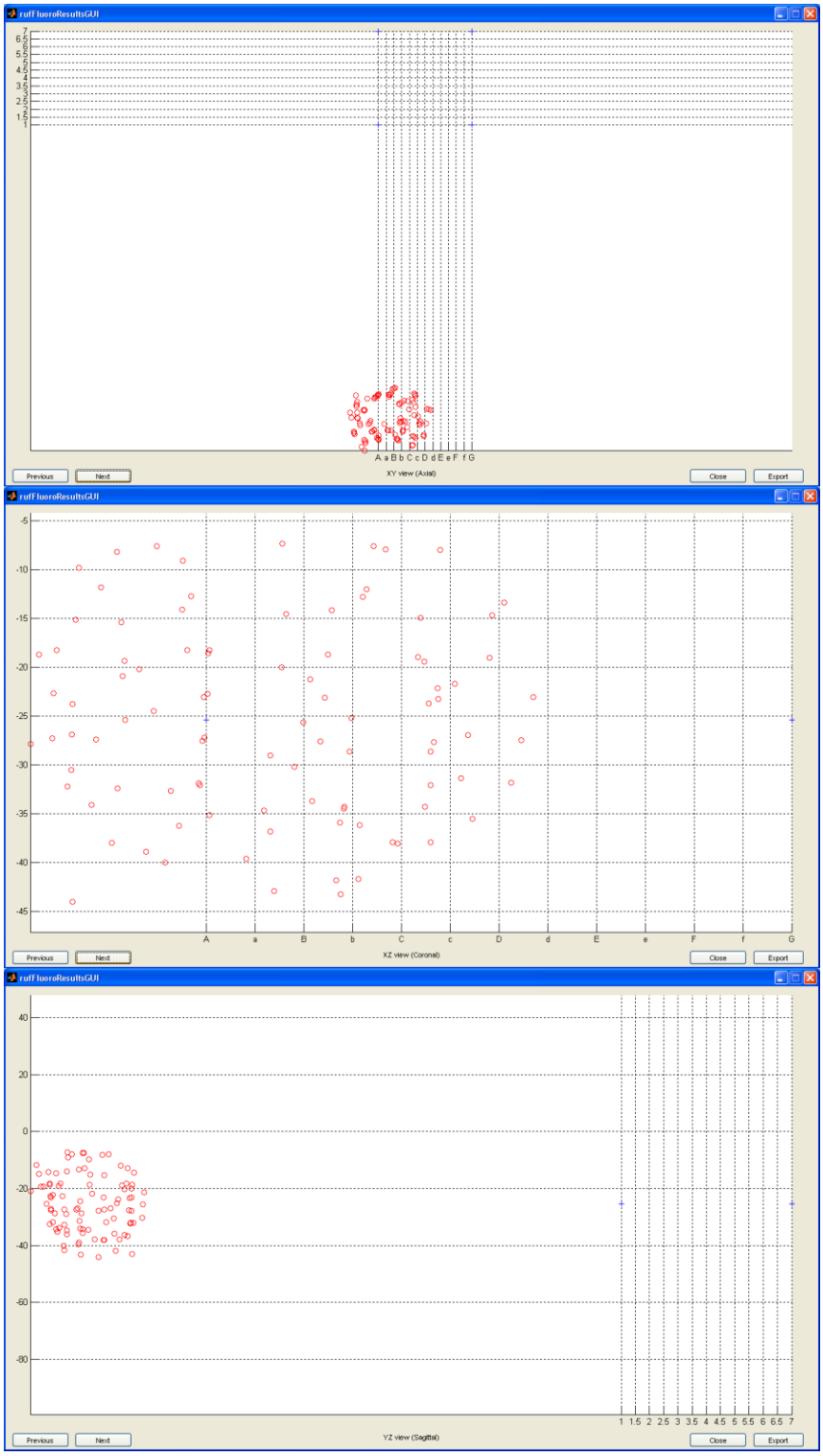

Figure 53 The rufFluoroResultsGUI window: Projected views – axial (top), coronal (middle), sagittal (bottom)

Finally, the remaining buttons in the rufFluoroResultsGUI are the Export button and the Close button. The Export button saves the 3D coordinates of the reconstructed seed cloud in a designated file location, but since a text file is automatically saved when reconstruction is run, this function is rarely used. The Close button closes the rufFluoroResultsGUI, which may also be done by pushing the red X in the top right corner.

Once reconstruction is completed, we may move on to the fourth step of the pipeline, which is fluoroscopy-to-TRUS registration. Press Done or the red X to close the rufFluoroReconGUI window and to go back to the rufMainGUI window.

A.4 The rufRegistrationGUI Window

The rufRegistrationGUI window appears when the button called US-Fluoro Registration under the RUF panel in the rufMainGUI window is pushed (see Figure 54) and a specific reconstruction is selected. This window covers the last of the four steps of the processing pipeline, which is fluoroscopy-to-TRUS registration. It also has the feature of computing dose. By the time this window is opened, it is assumed that all prior steps have already been completed. It therefore initially shows the volume of the selected ultrasound batch and the selected reconstruction (red dots) either centered (if a previous registration has not been saved) or registered (if a previous registration has been saved) on the ultrasound volume. The ultrasound image information, including the origin and pixel spacing, as well as the numbers of this initial registration, including the rotation matrix, translation vector, and scale, are also initially displayed.

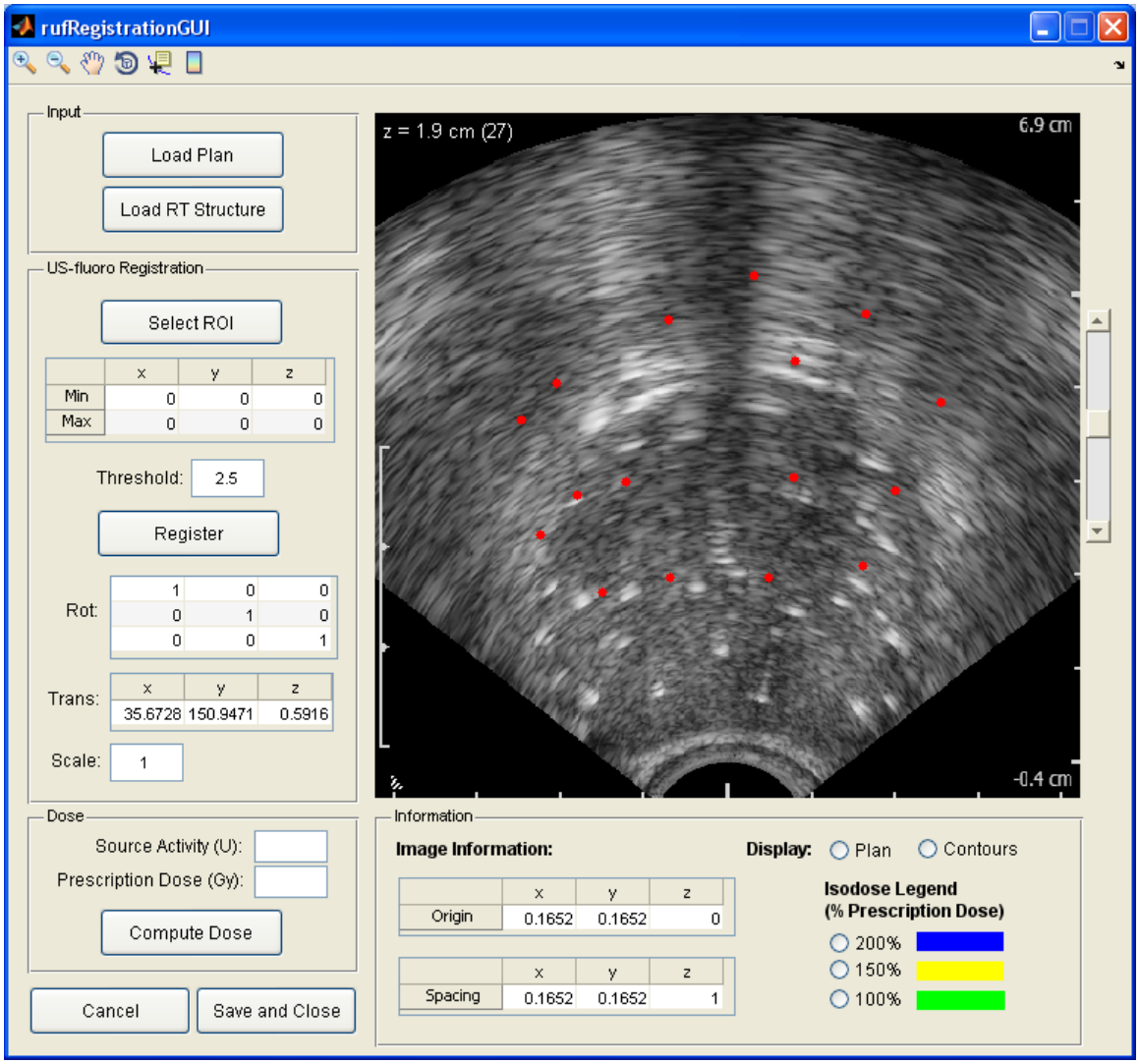

Figure 54 The rufRegistrationGUI window before registration.

The selected ultrasound volume and reconstruction are initially displayed.

To run the fluoroscopy-to-TRUS registration algorithm, several inputs must first be set. The plan must be loaded; or, if the plan is unavailable, an ROI may be selected instead. Both inputs are used to initialize optimization in the registration algorithm. To load a plan, select the Load Plan button and find the DICOM images which contain the planned seed locations. Otherwise, to select an ROI, the user may push the Select ROI button, click-and-drag across the ultrasound image, and double-click to accept the drawn ROI. The user may also manually input the limits (minimums and maximums) of the desired ROI. Finally, the user should also set a threshold for segmenting the bright hyperechoic spots in the volume which is

used for the point-to-volume registration. By default, this value is set to 2.5. The origin and spacing are also inputs into the registration algorithm; while the values may be changed, they should generally be kept to their default values. Once all inputs are set, push Register to run the fluoroscopy-to-TRUS registration. While the program is running, the user may look at the MATLAB command window to see how the iterations are going. Registration generally completes within one minute. The registered reconstruction should appear immediately on the ultrasound volume once registration is finished (see Figure 55). The corresponding numbers, i.e. rotation matrix, translation vector, and scale, should also be updated in their appropriate locations. Click the arrows on the slider bar to go through slices of the ultrasound volume and registration. The images may also be zoomed, panned and rotated by the mini-toolbar located at the top left corner of the window. The user should verify that the registered reconstructed seeds (red dots) generally overlap the bright hyperechoic spots on the ultrasound volume.

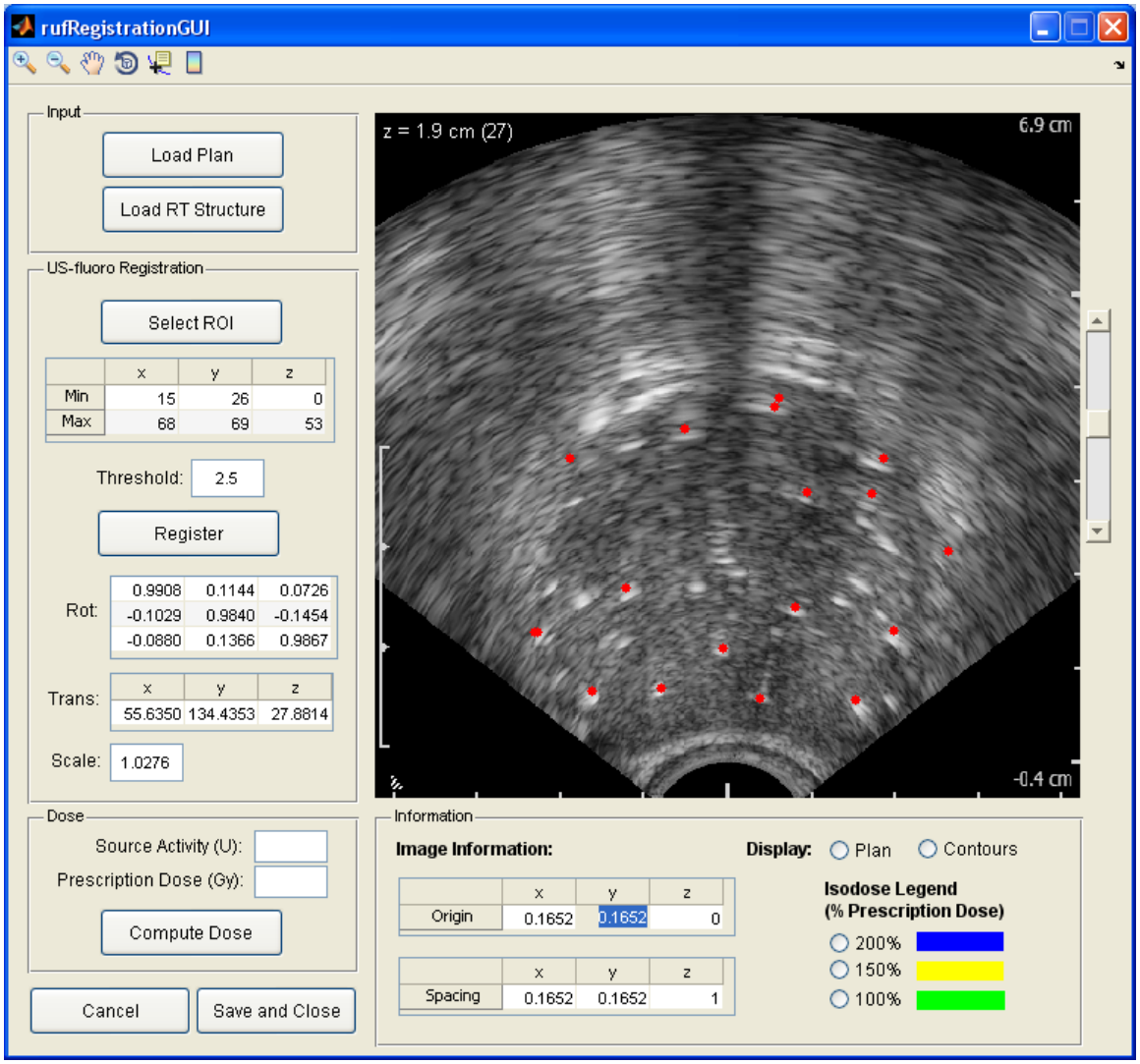

Figure 55 The rufRegistrationGUI window after registration.

Although registration is the last algorithm of the pipeline, it may be helpful to also see other information overlaid in this window, including the plan, the contours, and the dose (see Figure 56). As indicated earlier, the plan may be loaded by the Load Plan button. The display of the plan may be turned on or off by pressing the appropriate radio button under the Display section of the Information panel. When turned on, the planned seed locations will display as green squares on the ultrasound volume. The contours may be loaded by the Load RT Structure button and choosing the appropriate DICOM files that contain the contours. Like the plan, the contours may be displayed by pressing the appropriate radio button. When turned on, the contours will display as thin lines – red for the prostate, yellow for the planning target

volume, blue for the urethra, and green for the rectum. Dose may also be displayed after the Compute Dose button is pressed. This button calculates dose from the current registered seeds once inputted source activity and prescription dose are entered. To display the dose, choose the appropriate radio buttons next to the desired isodose level to display. The dose will then display as thick lines – blue for 200%, yellow for 150%, and green for 100%. Displaying the contours along with the dose helps in identifying cold spots.

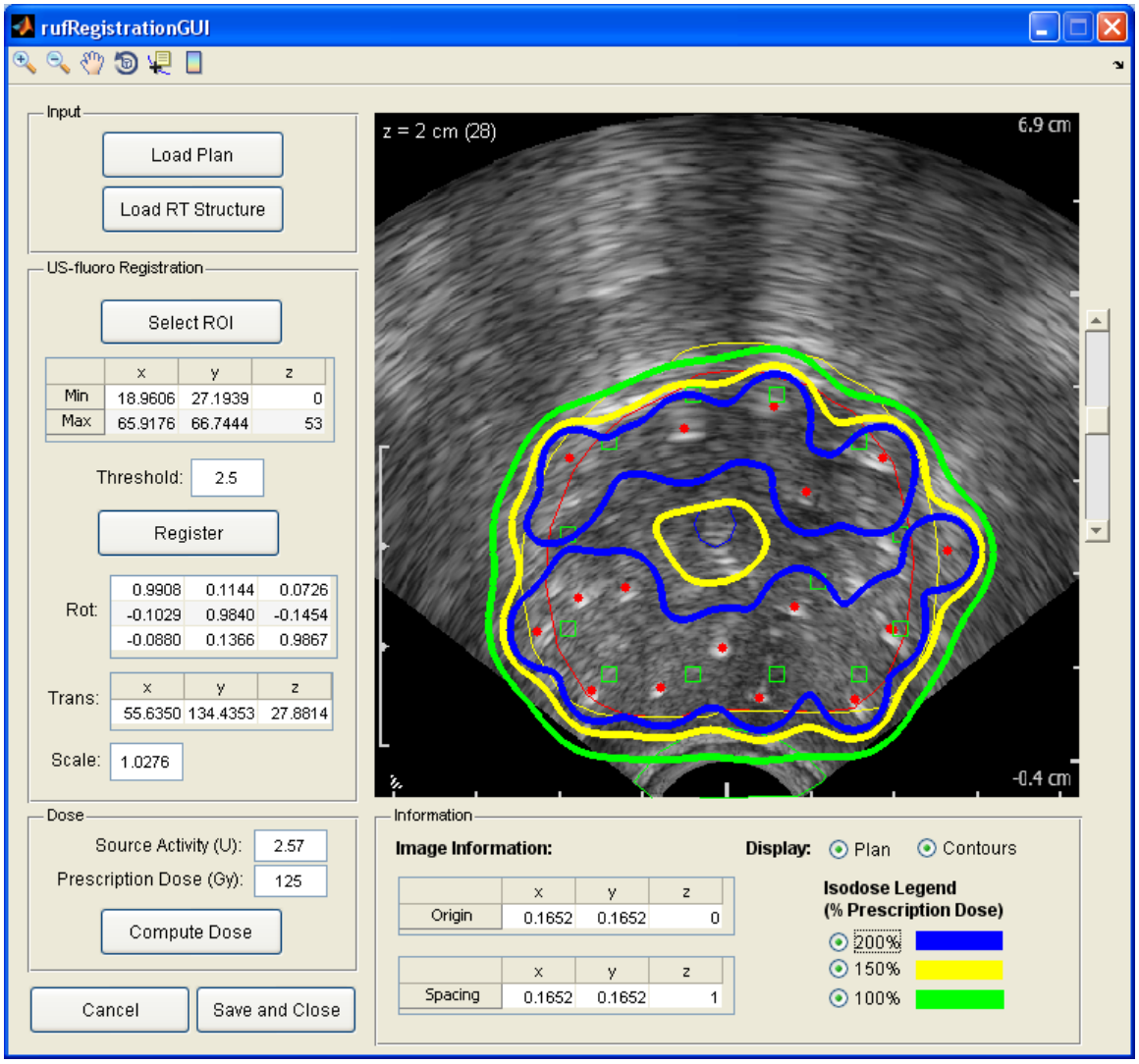

Figure 56 The rufRegistrationGUI window after registration with all plan, contours, and dose overlaid.

Finally, the remaining buttons in the rufRegistrationGUI are the Cancel button and the Save and Close button. Cancel will close the window without saving, and pushing the red X at the top right corner

performs the same function. Save and Close will save all the results, including the registration, the plan, the contours, and the dose.

In this appendix, we presented an overview and user manual of our RUF GUI. It has proved an invaluable tool, as more than 50 patients have been acquired and analyzed with the RUF GUI. It has also played an important role to make RUF more accessible to other clinics, as its design has served as a model for the ultrasound-fluoroscopy portion of the commercial treatment planning software produced by Acoustic MedSystems, Inc. known as RadVision.

Appendix B. Localization of Brachytherapy Seeds in Magnetic Resonance Imaging

While seed localization may be best achieved by ultrasound and fluoroscopy, or by photoacoustic imaging, they are by no means the only imaging modalities that may be applied. MRI is another method that may be used to both visualize and localize seeds. Being closely related to the topic of this dissertation but not sufficiently significant to be included as a chapter, this appendix, originally presented at the IEEE International Symposium on Biomedical Imaging [37], demonstrates some preliminary results toward this objective.

B.1 Introduction

MRI is a promising modality for guiding brachytherapy, since it provides excellent substructure imaging of the prostate. Currently, many practitioners use TRUS accompanied by X-ray to guide seed placement in the OR. While TRUS is useful for prostate imaging, it is an inadequate modality for visualizing seeds and substructures such as tumors. X-ray displays seeds well but images the prostate poorly. Since MRI can image both the prostate and the needles used during seed deployment, MRI-guided brachytherapy has been tested and validated in over 500 patients using the Signa SP 0.5T open-bore scanner [5] and is now progressing toward conventional closed-bore scanners through the aid of robotics [64, 9].

Localizing seeds within MR images has been problematic because the seeds generally appear as diffuse, dark voids (see Figure 57). Previous studies have assessed MR pulse sequences in imaging brachytherapy seeds [10, 50]. However, recent developments in pulse sequences that image local changes in susceptibility provide a new opportunity to revisit this topic. In this paper, we provide an initial demonstration of the potential to image and localize brachytherapy seeds using the Inversion-Recovery with ON-Resonant Water Suppression (IRON) pulse sequence [58]. Our results demonstrate a clarity of seed visualization that is unprecedented. The potential for localization of seeds using non-invasive MRI has

implications both for in-scanner delivery of seeds and for postoperative evaluation of implant dosimetry profiles.

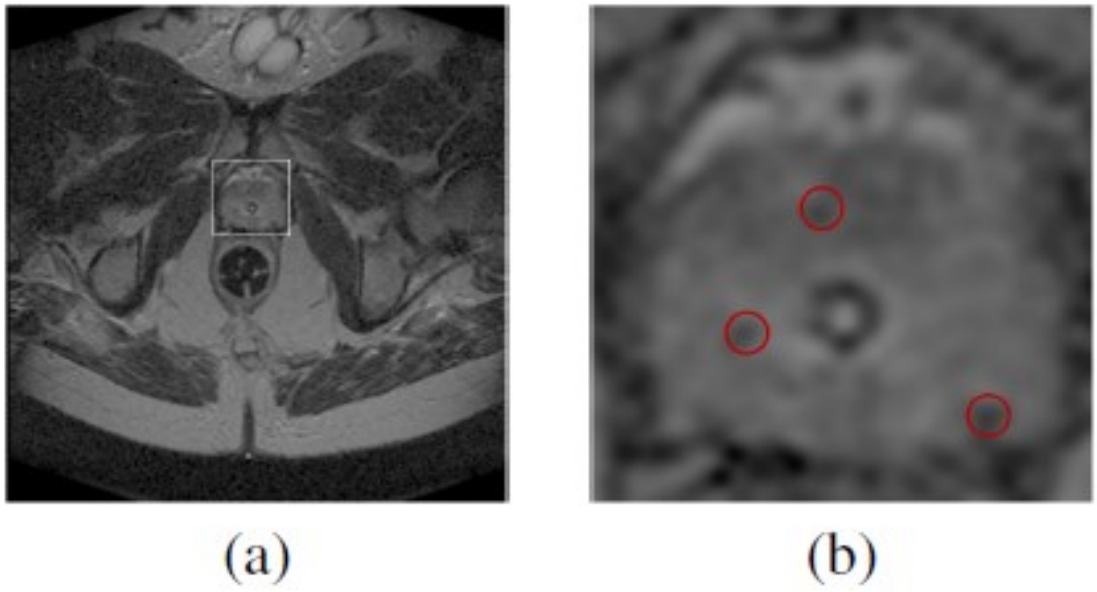

Figure 57 (a) Fast Spin Echo (FSE) image of the prostate. (b) Magnified view of the prostate area (white box) in (a). Red circles indicate three implanted seeds.

B.2 Materials and Methods

B.2.1 Inversion-Recovery With ON-Resonant Water Suppression

IRON is a versatile MRI methodology that enables positive contrast visualization in regions of magnetic field susceptibility [58]. It is based on the principle that a particle (e.g., a seed) with a magnetic susceptibility different than that of its surroundings (e.g., tissue) causes a disturbance to the static magnetic field of the MR scanner [52]. If a sphere of magnetic susceptibility Xand radius a is placed at the origin in a homogeneous static magnetic field of magnitude B_0 along direction z, the resulting field disturbance is described by the equation

$$\Delta B_z = \frac{\Delta \mathrm{X} B_0 a^3}{3} \frac{2z^2 - x^2 - y^2}{(x^2 + y^2 + z^2)^{5/2}}$$

where $\Delta X = X - X_{surroundings}$. The total magnetic field disturbance may be characterized as a dipole with positive ΔB_z values along the axis of the magnetic field surrounded by negative ΔB_z values in the form of an annulus (see Figure 58). Such a particle therefore causes an external frequency shift of

$$\Delta\omega_{external} = \gamma \Delta B_z$$

where γ is the gyromagnetic ratio of hydrogen. It is clear from these equations that the presence of the particle produces components in the MR frequency spectrum that are distinct from the Larmor frequency of $\omega_0 = \gamma B_0$ [see Figure 59(a)].

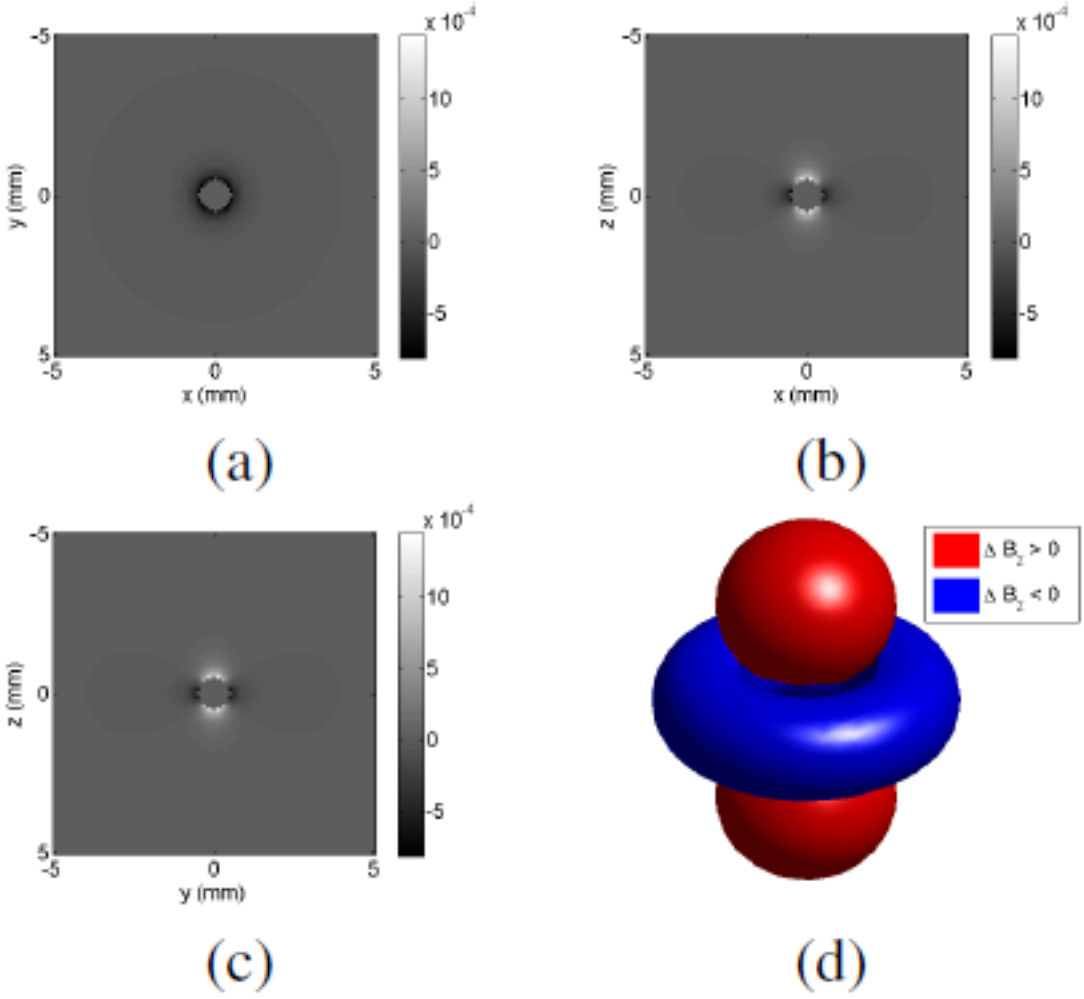

Figure 58 Simulation of the magnetic field disturbance caused by a palladium sphere of radius 0.5 mm in water. (a) XY view. (b) XZ view. (c) YZ view. (d) Isosurface.

IRON selects these off-resonant protons near the susceptibility generating particle by deliberately applying a spectrally selective on-resonant radio frequency (RF) saturation pulse with a limited bandwidth (BW_{Sat}) prior to the imaging part of the pulse sequence [see Figure 59(b)]. This suppresses the on-resonant water protons of the background tissue but leaves the off-resonant protons near the particle unaffected. The area around the susceptibility-generating particle may thus be seen with positive contrast. Moreover, the size of the area with positive signal may be controlled by BW_{Sat} and the level of background suppression may be controlled by the flip angle, α_{Sat}.

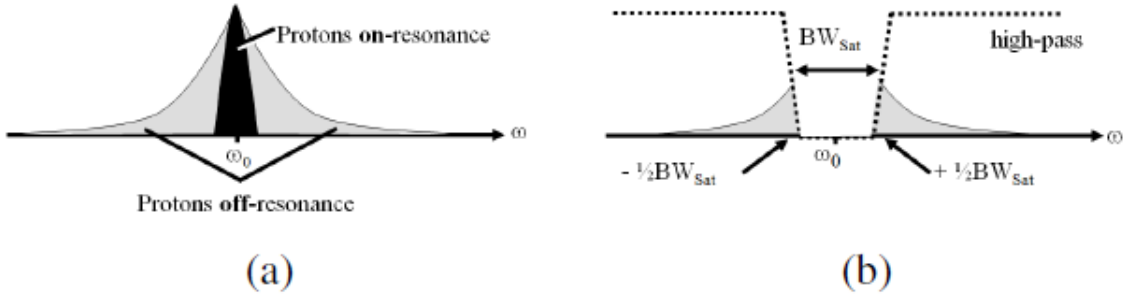

Figure 59 (a) MR frequency spectrum without IRON prepulse. (b) MR frequency spectrum with IRON prepulse.

B.2.2 Seed Localization

Once IRON images have been acquired, the brachytherapy seeds must be localized for dosimetry calculation. We thus developed a localization algorithm based on the blob detection technique of the Laplacian of a Gaussian (LoG) [41] to determine seed coordinates from the IRON volume.

In order to apply the LoG, the first step to our localization algorithm is to apply morphological preprocessing so each seed appears more blob-like. To do so, a morphological top hat by reconstruction is applied to the complemented volume, resulting in an image with only the blob-like centers of the dipoles. Next, the volume is filtered by a LoG to narrow down the seed locations. The minima to this resulting image may be thresholded to obtain a binary image volume, each region containing one or more seeds.

Once we have a binary image, each region is then analyzed to determine the number of seeds in the region and, ultimately, the seed locations. By this point in the algorithm, due to scaling issues, seeds are generally well localized in the XY plane but not so well in the Z direction. We thus determine the number of seeds in each region by analyzing the region volume statistics. Once each region's seed count is

determined, the region is divided into equal subregions along the Z axis, where finally, the centroids of each subregion determine the seed coordinates.

B.2.3 Experiment

We built two MRI compatible phantoms to assess the potential of using IRON for prostate brachytherapy seed visualization and localization. Typical seed compositions were first researched to determine which materials should be included in the phantom. In general, seeds consist of radioactive agents such as iodine-125 or palladium-103. The outer cylindrical shell is often composed of titanium or stainless steel. Seeds also contain gold or silver spheres to serve as X-ray markers.

The first phantom is made of gelatin (Knox; Kraft Foods, Tarrytown, NY, USA) embedded with five layers of three “seeds” each, for a total of fifteen seeds. The ``seeds'' in each of the five layers are made of different seed-related materials (dimensions shown in Table 8), in particular, 99.95% pure nonradioactive palladium, 99.95% pure silver, titanium alloy Ti6Al, nonmagnetic stainless steel, and training seeds (Theraseed; Theragenics Corporation, Buford, GA, USA). The training seeds, however, are not equivalent to actual seeds because they are not radioactive. The second phantom is also made of gelatin, but this time in a 61 nonradioactive palladium “seed” configuration inserted using an actual treatment plan.

Table 8 Actual sizes of cylindrical seeds

Material	Diameter (mm)	Length (mm)
Palladium	0.8	4.0
Silver	0.8	4.0
Titanium	0.6	4.0
Stainless Steel	0.7	5.0
Theraseed	0.8	4.5

MR imaging was carried out on a 3T Achieva MRI system (Philips Medical Systems). For the first phantom, the parameters for the on-resonant water suppression prepulse were BW_{Sat} = 100 Hz and α_{Sat} = 90°, determined and optimized for the first palladium layer. Imaging time was 3.7 minutes per layer. The parameters for the second phantom were BW_{Sat} = 40 Hz and α_{Sat} = 110° with total imaging time of 15 minutes. Typical parameters for the 3D segmented k-space gradient-echo (GRE) imaging sequence that followed the IRON prepulse were as follows: 3.9/1.5, 19 broadband on-resonant radiofrequency excitations

per k-space segment with a constant 15° flip angle, 74 msec acquisition window, 140 × 112 mm field of view, partial echo, 642 Hz/pixel bandwidth, and 288 × 220 image matrix.

B.3 Results

The resulting MR images of the first phantom are shown in Figure 60 and Figure 61. Table 9 shows volume magnetic susceptibilities [52] as well as summarized statistics.

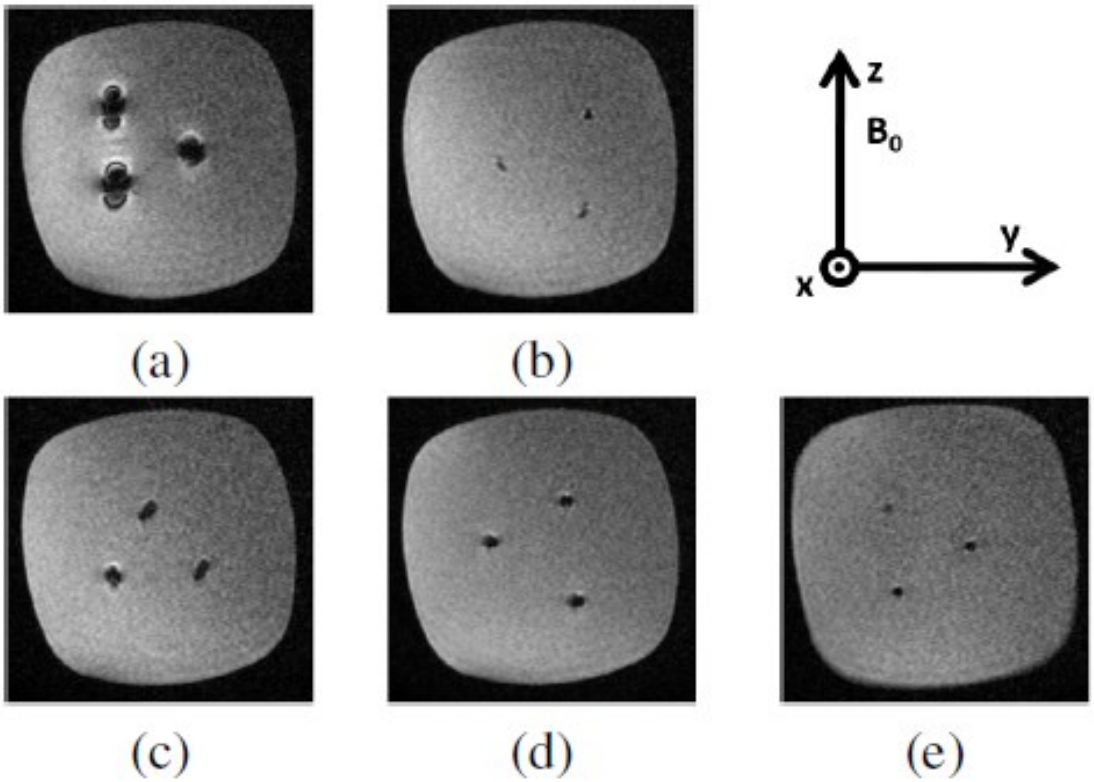

Figure 60 GRE slice images of the five phantom materials without the IRON prepulse. (a) Palladium. (b) Silver. (c) Titanium. (d) Stainless steel. (e) Training seed (Theraseed).

The difference that the IRON prepulse makes in the appearance of the seeds is clearly evident in these figures. In Figure 60, the cylinders appear as dark unclear voids. On the other hand, images with the IRON prepulse in Figure 61 show strong positive contrast with a characteristic dipole shape. The background is also significantly darkened due to the suppression of on-resonant protons in the gelatin. Although this background suppression is inhomogeneous near the boundaries (red arrows in Figure 61),

this is expected behavior as susceptibility differences near the phantom borders also generate off-resonant protons.

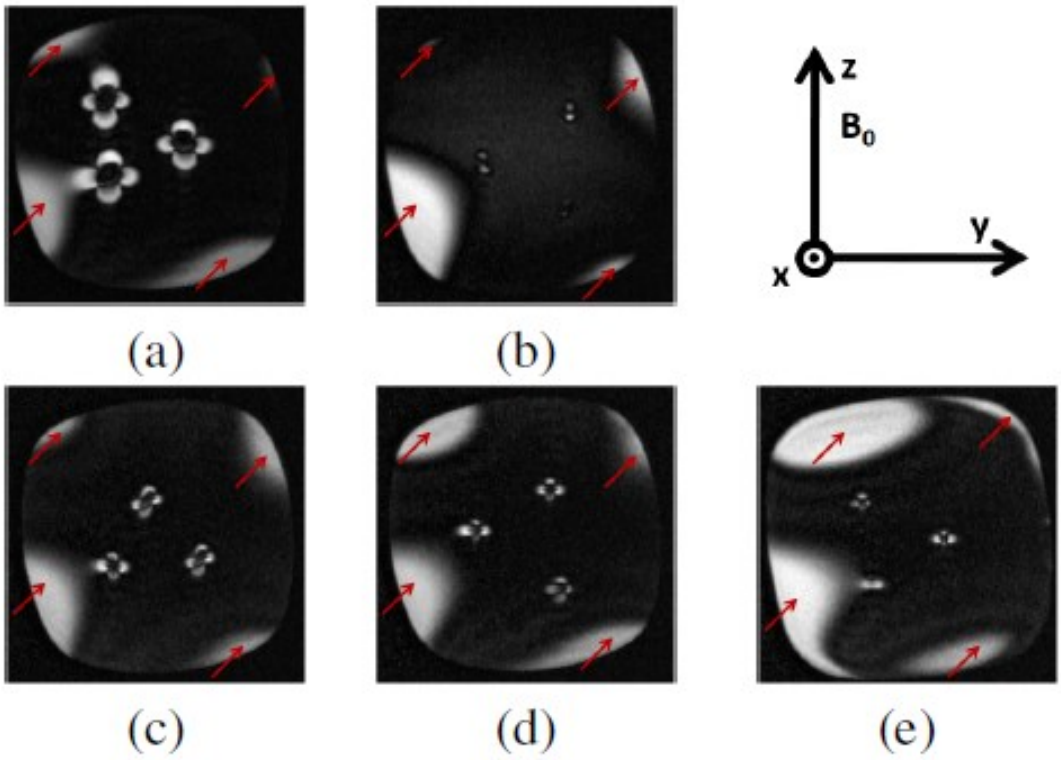

Figure 61 GRE slice images of the five phantom materials with the IRON prepulse. Red arrows show areas of inhomogeneous background suppression. (a) Palladium. (b) Silver. (c) Titanium. (d) Stainless steel. (e) Training seed (Theraseed).

The size and contrast of each material also generally correlate with ΔX (see Table 9), and therefore follows our theoretical equations. Stainless steel seems to be an exception, since it appears smaller than palladium although theoretically it has a larger ΔX. However, the actual ΔX of the stainless steel seeds in the phantom is uncertain and may truly be less than palladium. This is suggested not only by Figure 61 and Table 9 but also by Figure 60 taken prior to any IRON imaging.

Table 9 Average statistics for IRON images in Figure 61.

Material	X ($\times 10^{-6}$)	ΔX ($\times 10^{-6}$)	Y (mm)	Z (mm)	Contrast
Palladium	806	~815	12	14	32
Silver	-24	~-15	3.4	5.4	3
Titanium	182	~191	8.7	8.3	15
Stainless Steel	3520 to 6700	~5120	8.3	6.1	24
Theraseed	Unknown	Unknown	6.7	4.5	13
Gelatin/Tissue	-11.0 to -7.0	0	-	-	-

This agreement with theory is further exemplified in the isosurface shown in Figure 62. The shapes of the three palladium cylinders in Figure 62(a) are clearly similar to the characteristic dipole shape shown for a sphere in Figure 58(d). Our theoretical equations suggest both positive and negative magnetic field distortions; however, IRON shows both distortions with positive contrast. Although simulations of a finite cylinder would be more suitable, the physics of such a magnetic field distortion is not easily described and was therefore not simulated. Nonetheless, the similarity of the phantom's short finite cylinders to the spherical model shows that IRON produces images as was expected through theory.

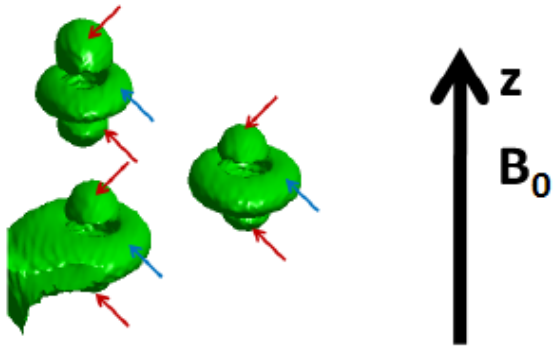

Figure 62 Isosurface of palladium layer using IRON imaging. Red arrows show areas of positive distortion shown with positive contrast; blue arrows show areas of negative distortion shown with positive contrast.

Finally, it may appear at first glance that it is not easy to localize the seeds because of the extended pattern that is characteristic of the IRON images. However, we developed the localization algorithm described in Section B.2.2 and applied it to the more realistic 61 seed configuration of the second phantom as an initial demonstration to determine its feasibility.

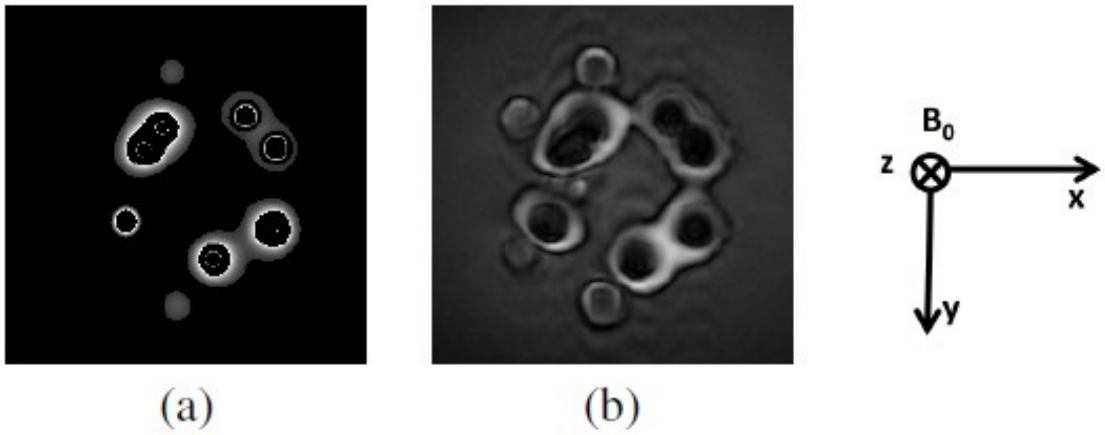

Figure 63 (a) Slice in the simulation volume of 61 seed phantom. (b) Slice in the MRI IRON volume of 61 seed phantom.

Figure 63 shows a slice through the simulated and actual IRON MRI volumes, while Figure 64 shows steps along the process of the localization algorithm. In the simulation, 61 of 61 seeds were correctly localized with a mean localization error of 1.1643 mm (standard deviation 0.7412). Running time in MATLAB was 70 s for the $512 \times 512 \times 60$ double precision volume on a 2.33 GHz Intel Core 2 Duo CPU. In the IRON MRI case, 62 seeds were identified (1 false positive) with a mean localization difference of 2.5660 mm (standard deviation 1.6851) when compared to manual segmentation. Running time was longer at 123 s since the algorithm needed to be adjusted for the longer cylindrical seeds in the IRON volume as compared to the spheres in the simulation.

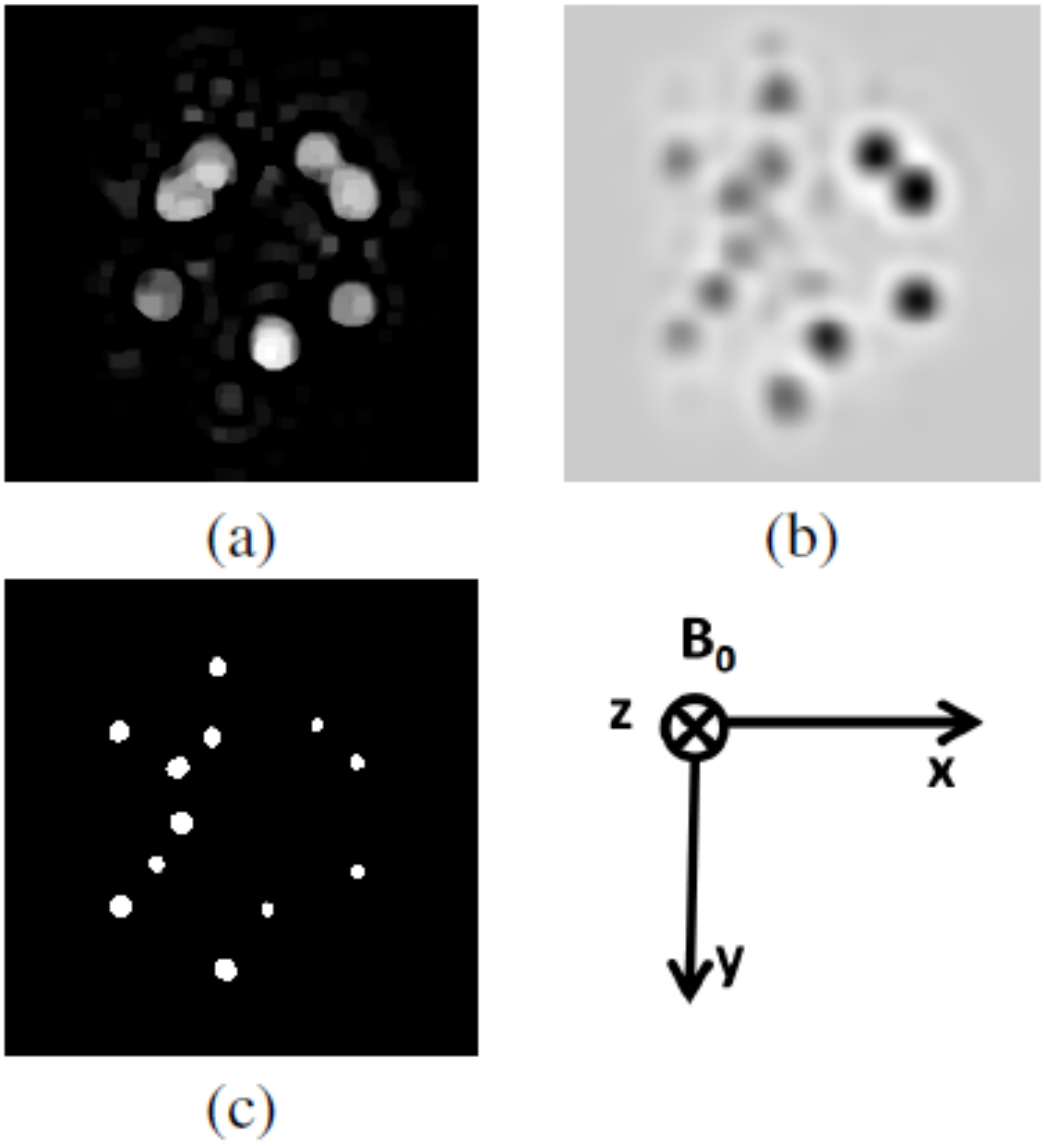

Figure 64 Steps of localization algorithm on IRON volume. (a) Slice after morphological top hat by reconstruction. (b) Slice after LoG. (c) Slice after binarizing volume.

B.4 Discussion

In all, this study shows the feasibility of using the IRON pulse sequence for seed localization in MRI. With palladium depicted very well in the phantom images, we expect actual palladium-103 seeds to be similarly well visualized through IRON imaging. Even iodine-125 seeds should be visible with IRON

MRI as they often have titanium or stainless steel shells, both of which produce large signals. As signal strength may be adjusted with BW_{sat}, this also leaves room for an adjustment in size should seeds of either type appear too large or too small.

The initial localization algorithm also shows that seeds imaged by IRON can be easily detected. Without IRON imaging, seed localization may be challenging for a human, much more so for a localization algorithm. With IRON imaging, however, simple localization algorithms can complete the task well.

In the future, more realistic phantom experiments need to be carried out in order to properly discern the appearance of brachytherapy seeds in a clinical setting. This involves replacing pure materials with more seed-like objects, while also increasing the density of seeds. Moreover, as air may result in positive contrast signals through IRON, air-prone organs near the prostate, such as the rectum or the urethra, must also be emulated to assess such an effect. Lastly, a clinical study with patients and actual seeds should also be conducted to make intraoperative seed localization and real-time dosimetry in MRI a reality.

In summary, this study presents exciting opportunities in MRI brachytherapy research. IRON has shown to be a promising methodology for imaging seeds, avoiding the disadvantages of conventional MR pulse sequences. With proper seed localization techniques, it consequently allows MRI to be more effective in guiding brachytherapy operations than TRUS or X-ray. Finally, as intraoperative seed localization and real-time dosimetry are a near possibility, prostate cancer patients can receive more optimized cancer treatment with IRON enhanced MRI-guided prostate brachytherapy.

References

1 Ballard, D.H. 1981, "Generalizing the Hough transform to detect arbitrary shapes", Pattern Recognition, vol. 13, no. 2, pp. 111.

2 Boctor, E.M., Verma, S., Clarke, C.C., DeJournett, T., Spicer, J.B. & Kang, J.U. 2010, "Prostate brachytherapy seed localization using combined photoacoustic and ultrasound imaging", Abstract in SPIE Medical Imaging.

3 Bostwick, D.G. & Cheng, L. 2008, "Urologic surgical pathology", Elsevier Health Sciences.

4 Canny, J. 1986, "Computation approach to edge detection", IEEE Transactions on Pattern Analysis and Machine Intelligence, vol. PAMI-8, no. 6, pp. 679-698.

5 D'Amico, A., Cormack, R., Tempany, C., Kumar, S., Topulos, G., Kooy, H. & Coleman, C.N. 1998, "Real-time magnetic resonance image-guided interstitial brachytherapy in the treatment of select patients with clinically localized prostate cancer", International Journal of Radiation Oncology Biology Physics, vol. 42, no. 3, pp. 507-515.

6 D'Amico, A.V., Cormack, R., Kumar, S. & Tempany, C.M. 2000, "Real-time magnetic resonance imaging-guided brachytherapy in the treatment of selected patients with clinically localized prostate cancer", Journal of Endourology, vol. 14, no. 4, pp. 367-370.

7 Davis, B.J., Horwitz, E.M., Lee, W.R., Crook, J.M., Stock, R.G., Merrick, G.S., Butler, W.M., Grimm, P.D., Stone, N.N., Potters, L., Zietman, A.L. & Zelefsky, M.J. 2012, "American Brachytherapy Society consensus guidelines for transrectal ultrasound-guided permanent prostate brachytherapy", Brachytherapy, vol. 11, no. 1, pp. 6-19.

8 Dehghan, E., Lee, J., Fallavollita, P., Kuo, N., Deguet, A., Le, Y., Clif Burdette, E., Song, D.Y., Prince, J.L. & Fichtinger, G. 2012, "Ultrasound-fluoroscopy registration for prostate brachytherapy dosimetry", Medical Image Analysis, vol. 16, no. 7, pp. 1347-1358.

9 DiMaio, S.P., Fischer, G.S., Maker, S.J., Hata, N., Iordachita, I., Tempany, C.M., Kikinis, R. & Fichtinger, G. 2006, "A system for MRI-guided prostate interventions", BioRob 2006, The First IEEE/RAS-EMBS International Conference on, pp. 68.

10 Dubois, D.F., Prestidge, B.R., Hotchkiss, L.A., Bice Jr., W.S. & Prete, J.J. 1997, "Source localization following permanent transperineal prostate interstitial brachytherapy using magnetic resonance imaging", International Journal of Radiation Oncology Biology Physics, vol. 39, no. 5, pp. 1037-1041.

11 Fischler, M.A. & Bolles, R.C. 1981, "Random sample consensus: a paradigm for model fitting with applications to image analysis and automated cartography", Communications of the ACM, vol. 24, no. 6, pp. 381-395.

12 French, D., Morris, J., Keyes, M., Goksel, O. & Salcudean, S. 2005, "Computing intraoperative dosimetry for prostate brachytherapy using TRUS and fluoroscopy", Academic Radiology, vol. 12, no. 10, pp. 1262-1272.

13 Fuller, D.B. & Jin, H. 2007, "Computed tomography–ultrasound fusion brachytherapy: Description and evolution of the technique", Brachytherapy, vol. 6, no. 4, pp. 272-279.

14 Gong, L., Cho, P.S., Han, B.H., Wallner, K.E., Sutlief, S.G., Pathak, S.D., Haynor, D.R. & Kim, Y. 2002, "Ultrasonography and fluoroscopic fusion for prostate brachytherapy dosimetry", International Journal of Radiation Oncology Biology Physics, vol. 54, no. 5, pp. 1322-1330.

15 Halır, R. & Flusser, J. 1998, "Numerically stable direct least squares fitting of ellipses", Proc. 6th International Conference in Central Europe on Computer Graphics and Visualization. pp. 125.

16 Han, B.H., Wallner, K., Merrick, G., Butler, W., Sutlief, S. & Sylvester, J. 2003, "Prostate brachytherapy seed identification on post-implant TRUS images ", Medical Physics, vol. 30, no. 5, pp. 898.

17 Haralick, R.M. & Shapiro, L.G. 1992, *Computer and robot vision*, Reading, Mass.: Addison-Wesley Pub. Co.

18 Haralick, R.M., Sternberg, S.R. & Zhuang, X. 1987, "Image analysis using mathematical morphology", Pattern Analysis and Machine Intelligence, IEEE Transactions on, vol. PAMI-9, no. 4, pp. 532-550.

19 Harrison, T. & Zemp, R.J. 2011, "Coregistered photoacoustic-ultrasound imaging applied to brachytherapy", Journal of Biomedical Optics, vol. 16, no. 8.

20 Jain, A.K., Deguet, A., Iordachita, I., Chintalapani, G., Blevins, J., Le, Y., Armour, E., Burdette, E.C., Song, D. & Fichtinger, G. 2007, "Intra-operative 3D guidance in prostate brachytherapy using a non-isocentric C-arm", Lecture notes in computer science, vol. 4792, pp. 9.

21 Jain, A., Deguet, A., Iordachita, I., Chintalapani, G., Vikal, S., Blevins, J., Le, Y., Armour, E., Burdette, C., Song, D. & Fichtinger, G. 2012, "Intra-operative 3D guidance and edema detection in prostate brachytherapy using a non-isocentric C-arm", Medical Image Analysis, vol. 16, no. 3, pp. 731-743.

22 Jain, A.K., Mustafa, T., Zhou, Y., Burdette, C., Chirikjian, G.S. & Fichtinger, G. 2005, "FTRAC - A robust fluoroscope tracking fiducial", Medical Physics, vol. 32, no. 10, pp. 3185-3198.

23 Jain, A.K., Zhou, Y., Mustufa, T., Burdette, E.C., Chirikjian, G.S. & Fichtinger, G. 2005, "Matching and reconstruction of brachytherapy seeds using the Hungarian algorithm (MARSHAL)", Medical physics, vol. 32, no. 11, pp. 3475-3492.

24 Jemal, A., Bray, F., Center, M.M., Ferlay, J., Ward, E. & Forman, D. 2011, "Global cancer statistics", CA: A Cancer Journal for Clinicians, vol. 61, no. 2, pp. 69-90.

25 Ji, Q., Costa, M.S., Haralick, R.M. & Shapiro, L.G. 1999, "Integrated linear technique for pose estimation from different geometric features", International Journal of Pattern Recognition and Artificial Intelligence, vol. 13, no. 5, pp. 705-733.

26 Kang, H.J., Stolka, P.J. & Boctor, E.M. "OpenITGLinkMUSiiC: a standard communications protocol for advanced ultrasound research", MIDAS Journal.

27 Kang, H.J., Kuo, N., Guo, X., Song, D., Kang, J.U. & Boctor, E.M. 2012, "Software framework of a real-time pre-beamformed RF data acquisition of an ultrasound research scanner", Progress in Biomedical Optics and Imaging - Proceedings of SPIE.

28 Kaplan, I.D., Meskell, P., Oldenburg, N.E., Saltzman, B., Kearney, G.P. & Holupka, E.J. 2006, "Real-time computed tomography dosimetry during ultrasound-guided brachytherapy for prostate cancer", Brachytherapy, vol. 5, no. 3, pp. 147-151.

29 Kon, R.C., Kumar Jain, A. & Fichtinger, G. 2006, "Hidden seed reconstruction from C-arm images in brachytherapy", Biomedical Imaging: Nano to Macro, 2006. 3rd IEEE International Symposium on, pp. 526.

30 Koukourakis, G., Kelekis, N., Armonis, V. & Kouloulias, V. 2009, "Brachytherapy for prostate cancer: A systematic review", Advances in Urology.

31 © 2012 Elsevier. Reprinted, with permission, from Kuo, N., Deguet, A., Song, D.Y., Burdette, E.C., Prince, J.L. & Lee, J. 2012, "Automatic segmentation of radiographic fiducial and seeds from X-ray images in prostate brachytherapy", Medical Engineering and Physics, vol. 34, no. 1, pp. 64-77.

32 Kuo, N., Dehghan, E., Deguet, A., Song, D.Y., Prince, J.L. & Lee, J. 2013, "A dynamic dosimetry system for prostate brachytherapy", Progress in Biomedical Optics and Imaging - Proceedings of SPIE.

33 Kuo, N., Kang, H.J., Dejournett, T., Spicer, J. & Boctor, E. 2011, "Photoacoustic imaging of prostate brachytherapy seeds in ex vivo prostate", Progress in Biomedical Optics and Imaging - Proceedings of SPIE.

34 Kuo, N., Kang, H.J., Song, D.Y., Kang, J.U. & Boctor, E.M. 2012, "Real-time photoacoustic imaging of prostate brachytherapy seeds using a clinical ultrasound system", Journal of Biomedical Optics, vol. 17, no. 6, pp. 066005.

35 Kuo, N., Lediju Bell, M.A., Boctor, E.M. 2013 "Prototype system and preliminary comparison of beamforming algorithms for photoacoustic imaging of prostate brachytherapy seeds", Ultrasonic Imaging Tissue and Characterization Symposium.

36 Kuo, N., Lee, J., Deguet, A., Song, D., Burdette, E.C. & Prince, J. 2010, "Automatic segmentation of seeds and fluoroscope tracking (FTRAC) fiducial in prostate brachytherapy x-ray images", Progress in Biomedical Optics and Imaging - Proceedings of SPIE.

37 © 2010 IEEE. Reprinted, with permission, from Kuo, N., Lee, J., Tempany, C., Stuber, M. & Prince, J. 2010, "MRI-based prostate brachytherapy seed localization", Biomedical Imaging: From Nano to Macro, 2010 IEEE International Symposium on, pp. 1397.

38 Lee, J., Kuo, N., Deguet, A., Dehghan, E., Song, D.Y., Burdette, E.C. & Prince, J.L. 2011, "Intraoperative 3D reconstruction of prostate brachytherapy implants with automatic pose correction", Physics in Medicine and Biology, vol. 56, no. 15, pp. 5011-5027.

39 Lee, J., Labat, C., Jain, A.K., Song, D.Y., Burdette, E.C., Fichtinger, G. & Prince, J.L. 2011, "REDMAPS: Reduced-dimensionality matching for prostate brachytherapy seed reconstruction", IEEE Transactions on Medical Imaging, vol. 30, no. 1, pp. 38-51.

40 Lee, J., Liu, X., Jain, A.K., Song, D.Y., Burdette, E.C., Prince, J.L. & Fichtinger, G. 2009, "Prostate Brachytherapy Seed Reconstruction With Gaussian Blurring and Optimal Coverage Cost", Medical Imaging, IEEE Transactions on, vol. 28, no. 12, pp. 1955-1968.

41 Lindeberg, T. 1998, "Feature detection with automatic scale selection", International Journal of Computer Vision, vol. 30, no. 2.

42 McAleavey, S.A., Rubens, D.J. & Parker, K.J. 2003, "Doppler ultrasound imaging of magnetically vibrated brachytherapy seeds", Biomedical Engineering, IEEE Transactions on, vol. 50, no. 2, pp. 252-254.

43 Mitri, F.G., Davis, B.J., Urban, M.W., Alizad, A., Greenleaf, J.F., Lischer, G.H., Wilson, T.M. & Fatemi, M. 2009, "Vibro-acoustography imaging of permanent prostate brachytherapy seeds in an excised human prostate - Preliminary results and technical feasibility", Ultrasonics, vol. 49, no. 3, pp. 389-394.

44 Mitri, F.G., Trompette, P. & Chapelon, J.-. 2004, "Improving the Use of Vibro-Acoustography for Brachytherapy Metal Seed Imaging: A Feasibility Study", IEEE Transactions on Medical Imaging, vol. 23, no. 1, pp. 1-6.

45 Nag, S., Ciezki, J.P., Cormack, R., Doggett, S., DeWyngaert, K., Edmundson, G.K., Stock, R.G., Stone, N.N., Yu, Y. & Zelefsky, M.J. 2001, "Intraoperative planning and evaluation of permanent prostate brachytherapy: Report of the American Brachytherapy Society", International Journal of Radiation Oncology Biology Physics, vol. 51, no. 5, pp. 1422-1430.

46 Narayanan, S., Cho, P.S. & Marks, R.J. 2002, "Fast cross-projection algorithm for reconstruction of seeds in prostate brachytherapy ", Medical Physics, vol. 29, no. 7, pp. 1572.

47 Otsu, N. 1978, "A threshold selection method from gray-scale histogram", IEEE Transactions on Systems, Man and Cybernetics, vol. 8, pp. 62.

48 Pan, L., Baghani, A., Rohling, R., Abolmaesumi, P., Salcudean, S. & Tang, S. 2013, "Improving photoacoustic imaging contrast of brachytherapy seeds", Progress in Biomedical Optics and Imaging - Proceedings of SPIE.

49 Polo, A., Salembier, C., Venselaar, J. & Hoskin, P. 2010, "Review of intraoperative imaging and planning techniques in permanent seed prostate brachytherapy", Radiotherapy and Oncology, vol. 94, no. 1, pp. 12-23.

50 Poulin, R., Martin, A.G., Dufour, M., Bouchard, G., Taschereau, R., Girouard, L.M., Pouliot, J. & Moisan, C. 1999, "Mr pulse sequences for accurate localisation of seeds and prostate contour in post-implant brachytherapy dosimetry", International Society of Magnetic Resonance in Medicine.

51 Reed, D.R., Wallner, K.E., Narayanan, S., Sutlief, S.G., Ford, E.C. & Cho, P.S. 2005, "Intraoperative fluoroscopic dose assessment in prostate brachytherapy patients", International Journal of Radiation Oncology Biology Physics, vol. 63, no. 1, pp. 301-307.

52 Schenck, J.F. 1996, "The role of magnetic susceptibility in magnetic resonance imaging: MRI magnetic compatibility of the first and second kinds", Medical Physics, vol. 23, no. 6, pp. 815-850.

53 Seber, G.A. 2009, *Multivariate observations*, Wiley.com.

54 Siddon, R.L. & Barth, N.H. 1987, "Stereotaxic localization of intracranial targets", International Journal of Radiation Oncology Biology Physics, vol. 13, no. 8, pp. 1241-1246.

55 Siegel, R., Naishadham, D. & Jemal, A. 2013, "Cancer statistics, 2013", CA: A Cancer Journal for Clinicians, vol. 63, no. 1, pp. 11-30.

56 Song, D.Y., Jain, A.K., Zhang, Z., Deguet, A., Le, Y., Armour, E., Burdette, E.C. & Fichtinger, G. 2011, "Dynamic intraoperative dosimetry for prostate brachytherapy using a nonisocentric C-arm", Brachytherapy, vol. 10, no. 2, pp. 98-106.

57 Stolka, P.J., Kang, H.J. & Boctor, E.M. 2010, "The MUSiiC toolkit: modular real-time toolkit for advanced ultrasound research", MIDAS Journal.

58 Stuber, M. 2007, "Positive contrast visualization of iron oxide-labeled stem cells using inversion-recovery with on-resonant water suppression (IRON) ", Magnetic Resonance in Medicine, vol. 58, no. 5, pp. 1072.

59 Su, J., Karpiouk, A., Wang, B. & Emelianov, S. 2010, "Photoacoustic imaging of clinical metal needles in tissue", Journal of Biomedical Optics, vol. 15, no. 2, pp. 021309.

60 Su, J.L., Bouchard, R.R., Karpiouk, A.B., Hazle, J.D. & Emelianov, S.Y. 2011, "Photoacoustic imaging of prostate brachytherapy seeds", Biomedical Optics Express, vol. 2, no. 8, pp. 2243-2254.

61 Su, Y., Davis, B.J., Herman, M.G. & Robb, R.A. 2004, "Prostate brachytherapy seed localization by analysis of multiple projections: Identifying and addressing the seed overlap problem", Medical physics, vol. 31, no. 5, pp. 1277.

62 Su, Y., Davis, B.J., Herman, M.G. & Robb, R.A. 2006, "TRUS-fluoroscopy fusion for intraoperative prostate brachytherapy dosimetry", Studies in Health Technology and Informatics, pp. 532.

63 Su, Y., Davis, B.J., Furutani, K.M., Herman, M.G. & Robb, R.A. 2007, "Seed localization and TRUS-fluoroscopy fusion for intraoperative prostate brachytherapy dosimetry", Computer Aided Surgery, vol. 12, no. 1, pp. 25.

64 Susil, R.C., Krieger, A., Derbyshire, J.A., Tanacs, A., Whitcomb, L.L., Fichtinger, G. & Atalar, E. 2003, "System for MR Image–guided Prostate Interventions: Canine Study1", Radiology, vol. 228, no. 3, pp. 886-894.

65 Taira, A.V., Merrick, G.S., Butler, W.M., Galbreath, R.W., Lief, J., Adamovich, E. & Wallner, K.E. 2011, "Long-term outcome for clinically localized prostate cancer treated with permanent interstitial brachytherapy", International Journal of Radiation Oncology Biology Physics, vol. 79, no. 5, pp. 1336-1342.

66 Todor, D.A., Zaider, M., Cohen, G.N., Worman, M.F. & Zelefsky, M.J. 2003, "Intraoperative dynamic dosimetry for prostate implants", Physics in Medicine and Biology, vol. 48, no. 9, pp. 1153-1171.

67 Tokuda, J., Fischer, G.S., Papademetris, X., Yaniv, Z., Ibanez, L., Cheng, P., Liu, H., Blevins, J., Arata, J., Golby, A.J., Kapur, T., Pieper, S., Burdette, E.C., Fichtinger, G., Tempany, C.M. & Hata, N.

2009, "OpenIGTLink: An open network protocol for image-guided therapy environment", International Journal of Medical Robotics and Computer Assisted Surgery, vol. 5, no. 4, pp. 423-434.

68 Treeby, B.E. & Cox, B.T. 2010, "k-Wave: MATLAB toolbox for the simulation and reconstruction of photoacoustic wave fields", Journal of Biomedical Optics, vol. 15, no. 2, pp. 021314.

69 Tubic, D., Zaccarin, A., Pouliot, J. & Beaulieu, L. 2001, "Automated seed detection and three-dimensional reconstruction. I. Seed localization from fluoroscopic images or radiographs ", Medical Physics, vol. 28, no. 11, pp. 2265.

70 Tutar, I.B., Managuli, R., Shamdasani, V., Cho, P.S., Pathak, S.D. & Kim, Y. 2003, "Tomosynthesis-based localization of radioactive seeds in prostate brachytherapy ", Medical Physics, vol. 30, no. 12, pp. 3135.

71 Vikal, S., Jain, A.K., Deguet, A., Song, D. & Fichtinger, G. 2006, "TU-EE-A3-03: Automated Segmentation of Radiographic Fiducials for C-Arm Tracking", Abstract in Medical Physics, vol. 33, no. 6, pp. 2208.

72 Vikal, S., Jain, A.K., Deguet, A., Song, D. & Fichtinger, G. 2006, "WE-C-330A-03: Seed Segmentation in C-Arm Fluoroscopy for Brachytherapy Implant Reconstruction", Abstract in Medical Physics, vol. 33, no. 6, pp. 2229.

73 Wei, Z., Gardi, L., Downey, D.B. & Fenster, A. 2006, "Automated localization of implanted seeds in 3D TRUS images used for prostate brachytherapy", Medical Physics, vol. 33, no. 7, pp. 2404-2417.

74 Wen, X., Salcudean, S.E. & Lawrence, P.D. 2010, "Detection of brachytherapy seeds using 3-D transrectal ultrasound", IEEE Transactions on Biomedical Engineering, vol. 57, no. 10 PART 1, pp. 2467-2477.

75 Westendorp, H., Hoekstra, C.J., van't Riet, A., Minken, A.W. & Immerzeel, J.J. 2007, "Intraoperative adaptive brachytherapy of iodine-125 prostate implants guided by C-arm cone-beam computed tomography-based dosimetry", Brachytherapy, vol. 6, no. 4, pp. 231-237.

76 Xu, M. & Wang, L.V. 2006, "Photoacoustic imaging in biomedicine", Review of Scientific Instruments, vol. 77, no. 4, pp. 041101.

77 Xu, Y., Feng, D. & Wang, L.V. 2002, "Exact frequency-domain reconstruction for thermoacoustic tomography - I: Planar geometry", IEEE Transactions on Medical Imaging, vol. 21, no. 7, pp. 823-828.

78 Xie, Y. & Ohya, J. 2009, "Efficient detection of ellipses from an image by a guided modified ransac", Proceedings of SPIE - The International Society for Optical Engineering.

79 Xue, J., Waterman, F., Handler, J. & Gressen, E. 2005, "Localization of linked 125I seeds in postimplant TRUS images for prostate brachytherapy dosimetry", International Journal of Radiation Oncology Biology Physics, vol. 62, no. 3, pp. 912-919.

Curriculum Vita

Nathanael Pei-En Kuo was born on January 13, 1985 in New Brunswick, New Jersey, USA. Having completed grades K-12 in the Edison Township Public Schools in New Jersey, he eventually went to the University of Illinois at Urbana-Champaign, where he graduated highest honors in May 2007 with a B.S. degree in Electrical Engineering and minors in Computer Science and Mathematics. He then entered the Biomedical Engineering Ph.D. program in August 2007. His research interests include medical image analysis applied to image-guided interventions. His work has led him to span all stages of imaging, from acquisition to processing to analysis, and to delve into a variety of imaging modalities, such as X-ray, ultrasound, photoacoustic, and magnetic resonance imaging.